UNIVERSITY OF OSLO
Department of Chemistry

Ionic and electronic conductivity in the $LaNbO_4$ – $LaTaO_4$ system

Thesis for the Master of Science degree in Materials, Energy and Nanotechnology

Odd-Arne Ertzeid

October 2009

Preface

This thesis completes the final requirements for the Master of Science degree in Nanotechnology, which falls under the program Materials, Energy and Nanotechnology at the Department of Chemistry, University of Oslo. Work for this thesis took place at the Centre for Materials Science and Nanotechnology (SMN) in the time span of August 2007 - October 2009.

I would like to thank my two supervisors, Truls Norby and Reidar Haugsrud for guidance and advice in sorting out interesting and important measurements in the multitudes of measurement choices I had. Credit also goes to Zuoan Li for helping out with early XRD, Christian Kjølseth for teaching me the complex gas mixer (the hard way), Harald Fjeld for always being helpful, Nebojsa Cebasek for important battery recharging fishing trips and all the other nice people at the group for Solid State Electrochemistry at SMN.

Finally, a great deal of gratitude goes to Iris Dahle Andersson for being a great source of inspiration as I wrote this thesis, and of course a little smile goes to my little baby boy, Vebjørn Dahle Ertzeid for just being who he is.

University of Oslo, October 2009

Odd-Arne Ertzeid

Abstract

Defect chemical investigations on the $LaNbO_4$-$LaTaO_4$ system are, except for investigations on the parent phases, $LaNbO_4$ and $LaTaO_4$, non-existent. Research on this system is required to understand the impact of tantalum-doping on the conductivity of $LaNbO_4$. If Ta-doping is found to increase the conductivity of $LaNbO_4$, it could, in turn, open interesting, new avenues relating to doping and solid solubility in solid oxide fuel cell materials research.

In the work presented in this thesis, defect situations and conductivities for Ta-doped $LaNbO_4$ were investigated as a function of Ta-content. Electrical characterization of several samples, containing concentrations of between 38 and 48 atomic-percent Tantalum, were carried through. Measurements were done in reducing and oxidizing atmospheres in a temperature range from 500°C to 1200°C.

The phase transition between low-temperature monoclinic and high-temperature tetragonal $LaNbO_4$ was seen to increase, with increasing tantalum content, to a limit of ~850°C with 48 atomic-percent Ta. This was also shown to be the highest Ta-doping attainable under present experimental conditions.

Results showed that the defect model of pure $LaNbO_4$ fit that of Ta-doped $LaNbO_4$ rather well, with only a few alterations: Under wet, reducing conditions, proton conductivity dominated at any temperature. Under oxidizing conditions the low-temperature phase displayed decent proton conductivity. This changed over to oxygen ionic conductivity and later p-type electronic conductivity as temperature increased and the high-temperature phase was reached. It is possible that an observed increase in conductivity under reducing conditions, compared to oxidizing conditions, was due to a reduction of the samples.

It was seen that none of the Ta-containing $LaNbO_4$-samples had conductivities exceeding that of its parent pure Ca-doped $LaNbO_4$-phase. The highest proton conductivity measured was $4.5 \cdot 10^{-4}$ $S \cdot cm^{-1}$ for 48 atomic-percent Ta-doped $LaNbO_4$ at 1100°C.

XRD measurements on the sample containing 48 atomic-percent Ta showed three new phases in addition to $LaNbO_4$; $La_{0.33}TaO_3$ (tetragonal), $La(Ta_3O_9)$ (orthorhombic) and $LaTaO_4$. The new phases did not appear to impact conductivity much, if anything.

Table of contents

List of figures

List of tables

1 Introduction

"We are playing Russian roulette with features

of the planet's atmosphere that will profoundly impact generations to come.

How long are we willing to gamble?" – David Suzuki

The first part of this chapter gives a background on climate changes. Part two gives an introduction to fuel cell technology, while the final section gives a thorough justification for this study.

1.1 Climate change

It appears to be an undeniable fact that the climate on earth is changing. This, in itself, is nothing new. The climate on earth has always changed and will most definitely change in the foreseeable future. A new addition to the many variables controlling our planet's climate appeared with the dawning of the industrial age: Anthropic greenhouse gas emissions. The rapid increase of CO_2 and other greenhouse gases in the atmosphere, due to human emissions, only became an important topic in science and politics fairly recently. Today most environmental scientists believe that greenhouse gases emitted by human civilization play a significant role in the global warming being observed. Even a small change in global climate would seriously impact the lives of millions.

In order to reduce the human impact on earth's climate, a reduction in greenhouse gas emissions is desirable. One way to achieve this is by burning less CO_2-emitting fossil fuel. Fossil fuels, like coal, oil and

natural gas, are the main energy sources in use today. Of the three, natural gas is the cleanest and most future proof energy source due to its low carbon to energy ratio and plentiful abundance. The conventional process of extracting chemical energy stored in fossil fuels by burning is a cheap, although highly inefficient process, in which large amounts of waste heat is produced.

It is possible to imagine a scenario in the near future where nobody uses coal and oil, while a relatively cheap and more energy-efficient way to extract energy from natural gas has been found. This scenario would lead to a significant reduction to global emissions of CO_2.

On a longer time scale it is possible to imagine a second scenario where the global energy economy is based solely on renewable energy sources with hydrogen as energy carrier.

Fuel cells may contribute to both of these scenarios by efficiently converting fuel (both natural gas and hydrogen) and oxygen into exhaust gases while at the same time producing electricity.

1.2 The fuel cell

Fuel cells and batteries share many properties. Both of them consist of a set of one or more electrochemical galvanic cells, in which the energy from a chemical reaction is being converted into electricity. The main distinction between fuel cells and batteries is that fuel cells, in contrast to batteries, are open systems continuously being fed with new fuel. Batteries are closed systems containing only a given amount of fuel.

1.2.1 Historical background

The history of the fuel cell traces back to January 1839 when Christian Friedrich Schönbein first published the basic principles of a fuel cell in the Philosophical Magazine [1]. In February of the same year, Sir William Grove, later known as the Father of the fuel cell, created the world's first operating fuel cell [2]. He later improved the design and presented the details of his device, which he called a "Gaseous Voltaic Battery" three years later [3]. The electrodes were made of platinum strips and the electrolyte consisted of sulfuric acid. It is clear, from reading his notes, that he saw a great potential for using his new invention to commercially extract energy from hydrogen. In 1889 Ludwig Mond and Charles Langer started to address devices like

Groves gaseous voltaic batteries as “fuel cells” (Some say William White Jacques used the name before them).

Basic fuel cell technology slowly matured over the decades. The discovery of ever new materials made the electrolytes better and better and expensive platinum electrodes eventually got replaced by cheaper metals like nickel. Efficient catalysts, like platinum nano-particles, appeared, making the energy produced from a fuel cell gradually less expensive.

The first major boost towards making fuel cell technology a viable alternative to ordinary combustion engines came from the research NASA put into the Apollo missions in the 60’s. NASA needed a safer way than nuclear energy to produce electricity in space. Fuel cells fit their needs perfectly even though they still were rather expensive. The effort put into fuel cell technology research has increased steadily since then. Recently, the global warming debate has given fuel cell research another boost. “Everybody” wants to be part of a possible future economy based on renewable energy. Fuel cells may prove to play a significant part of this future economy.

1.2.2 The inner workings of a fuel cell

A fuel cell may simply be viewed as a device in which oxygen and fuel is converted into exhaust and energy. The energy being released is a combination of electricity and heat. The following applies to a fuel cell where the fuel is hydrogen and the exhaust is water:

$$2H_2(g) + O_2(g) \rightarrow 2H_2O(g) + \text{Energy} \qquad (1.1)$$

A single fuel cell consists of at least four distinctive parts: electrolyte, anode, cathode and catalyst (Figure 1.1). The anode and cathode are placed on opposite sides of an electrolyte. The electrolyte is made of a material that conducts ions very well, but acts poorly as an electric conductor. The anode, traditionally made of nickel metal, oxidizes the hydrogen gas into protons. Protons diffuse through the electrolyte while released electrons pass through an external circuit. At the cathode side of the fuel cell protons combine with oxygen gas and electrons to produce water. A catalyst makes the reactions go faster by lowering their kinetic barrier. These are the basic principles of Proton Conducting Fuel Cells, PCFC. The ceramic oxide materials being discussed in this thesis are meant to be possible electrolytes for a high temperature subtype of PCFCs called Proton Conducting Solid Oxide Fuel Cells (SOFC).

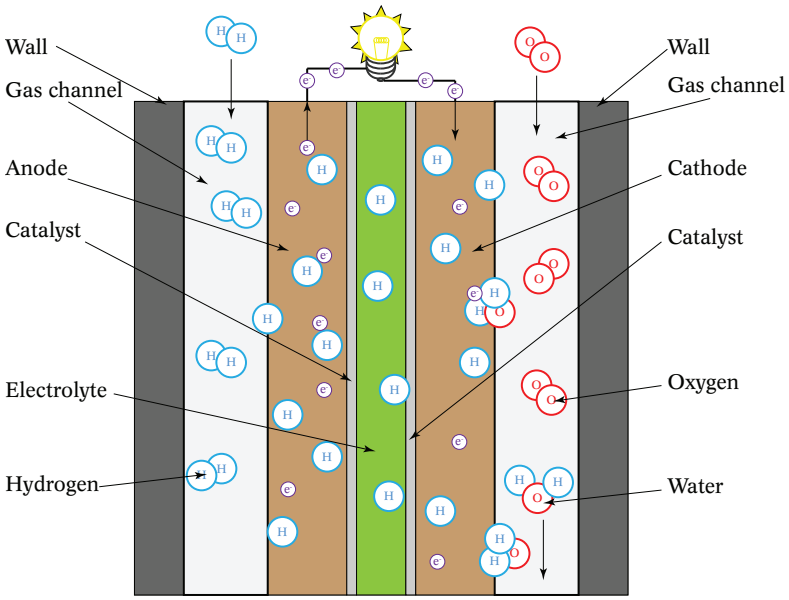

Figure 1.1 *– A sketch of a simple fuel cell converting hydrogen and oxygen into electrical energy and water.*

1.2.3 The electrolyte

There are certain requirements which have to be met in order for a material to be a good electrolyte candidate for a Proton Conducting SOFC: The material should have high ionic proton conductivity and a very low electronic conductivity. If an electrolyte has a high electronic conductivity, a substantial energy loss is experienced as electrons/holes pass through the electrolyte instead of the external circuit.

If a fuel cell is supposed to work in any real world industrial application without expensive gas separation, the electrolyte and all the other parts of the cell should have a high stability towards atmospheric gases and exhaust gases like CO_2. It is also desirable to have an electrolyte material that does not have a phase transition anywhere in its working temperature range in order to avoid unnecessary stress and possible cracks in the interface between electrolyte and electrodes.

1.2.4 Properties of $LaNbO_4$

$LaNbO_4$ shows great promise as a material to be used in proton conducting SOFC electrolytes. It has a high proton conductivity compared to most other electrolyte materials, while still showing a good long-term stability in CO_2-containing atmospheres [4]. Its stability in

both reducing and oxidizing atmospheres at elevated temperatures (~1100°C) is also good.

1.2.5 Properties of $LaTaO_4$

Due to the similar atomic radii of Nb and Ta, $LaTaO_4$ possesses properties similar to those of $LaNbO_4$. It has significant proton conductivity and displays good long-term stability in CO_2-containing atmospheres [5]. The stability at elevated temperatures is very good and the melting point is even higher than the melting point of $LaNbO_4$ (1930°C vs. 1620°C) [6][7].

1.3 Justification for this study

1.3.1 Low temperature fuel cells

Current efforts in developing electrolytes for proton exchange fuel cells have currently been centered on perfluorocarbon sulfonic acid polymer electrolyte (Nafion) and Pt–C electrodes [8]. These operate at temperatures around 80°C. Problems that have to be overcome before Nafion based fuel cells can be considered interesting in commercial applications include a way to remove exhaust water at 80°C, reducing CO-poisoning, reduce the price of Pt-electrodes, and solving the problem of fuel crossover [9][10].

1.3.2 High temperature fuel cells

A fuel cell that could work at a higher temperature would help overcome most of the problems associated with the low temperature polymer membranes. One of the approaches to increase the working temperature of fuel cells is to use solid state proton conductors based on metal oxides. State of the art high temperature proton conducting perovskites made of earth alkali cerates and zirconates, like $BaCe_{0.9}Y_{0.1}O_{2.95}$, display the, as of today, highest known proton conductivities (~0.01 S/cm) [11][12][13][14][15]. Their biggest problem when used as electrolytes in solid oxide fuel cells is that they decompose in even low concentrations of CO_2 and have a limited tolerance for very humid conditions [16]. This makes them unnecessarily expensive and difficult to operate on a larger industrial scale.

1.3.3 CO_2-stable fuel cells

Proton conductors that were known to be stable in CO_2-containing atmospheres used to have a proton conductivity less than one order of magnitude lower than the best perovskites. The sole exception to this was acceptor-doped $LaScO_3$ with a maximum conductivity of 0.006 S/cm at 600°C [17].

Recently this changed with the introduction of 1 mol% Ca-doped $LaNbO_4$, which was shown to be an almost pure ionic conductor with a proton conductivity of ~0.001 S/cm at 950°C [4].

1.3.4 Solid solubility in the $LaNbO_4$ – $LaTaO_4$ -system

Investigations on the solid solubility between $LaNbO_4$ and $LaTaO_4$ concluded that there are two extended regions of solid solubility on each side of a double phase region in the phase diagram between these compounds [18]. On the Nb-rich side of the phase diagram, a maximum solubility of between 40% and 50% Ta was found in the $LaNbO_4$-phase. It was also found that the phase transition temperature of the $LaNbO_4$-phase increased while the thermal expansion coefficient decreased with increasing Ta-content [19].

There are several reasons why it is of interest to see how the conductivities of $LaNbO_4$ evolve as increasing amounts of Ta replaces Nb: If the phase transition temperature could be raised higher than the probable working temperature of the fuel cell without degrading its proton conductivity to any significant degree, a major cause of stress between electrolyte and electrodes could have been removed [20]. This would require that the low-temperature monoclinic phase of $LaNbO_4$ has roughly the same proton conductivity as the high-temperature tetragonal phase of $LaNbO_4$.

Ta and Nb are somewhat expensive to separate due to their very similar chemistry. If one could use a mix of Nb_2O_5- and Ta_2O_5 -powders to produce electrolytes for fuel cells on a larger industrial scale, without any conductivity degradation in the final product, the total cost of production could be lowered by quite a bit. If the solid solution of $LaNbO_4$ and $LaTaO_4$ displays mixed protonic-electronic conductivity, it could be used as a membrane material for hydrogen separation.

Another interesting topic of investigation would be whether it is possible to deliberately introduce a nanoscopic secondary $LaTaO_4$-phase into the main $LaNbO_4$-phase. This so-called hetero phase doping could possibly lead to interesting new effects and defects not yet researched.

2 Theory

This chapter contains the theoretical foundation needed to discuss contemporary literature, and later to explain experimental data. The first section considers defect chemistry theory, while the second section reviews theory on electrical conductivity.

2.1 Defect chemistry

A crystalline material is a material which has a long range atomic order. Because it is not thermodynamically favorable for a crystal to maintain a perfect structure, any real crystalline materials have so-called defects at any temperature. Defects are areas or points in the crystal which deviate from the perfect structure. The concentration of defects in a structure can be determined if the thermodynamics of their formation is known. The equilibrium equations are similar to those used for any chemical reaction.

2.1.1 Types of defects

One way to classify defects is to consider their dimensionality. A point defect is classified as a 0-dimentional defect; a line defect is a 1-dimentional defect and so on. In addition to these structural defects there are electronic defects consisting of free electrons and electron holes. This thesis will mainly deal with point defects and electronic defects using the Kröger-Vink notation. (Section 2.1.3)

0-dimensional defects

0-dimensional defects, or point defects, are defects spanning just a single lattice position or a single atom. (Figure 2.1) The defects can be charged or be neutral. Examples of point defects are single vacancies, interstitials and foreign atoms. Intrinsic defects, which are present in even the purest crystal at any temperature, are differentiated from extrinsic defects, produced by impurities in the crystal. Examples of intrinsic

defects are Frenkel defects and Schottky defects, while doping is an example of an extrinsic defect. High concentrations of point defects in a material often lead to individual defects combining into bigger defect clusters, or 1-, 2- or 3-dimensional defects.

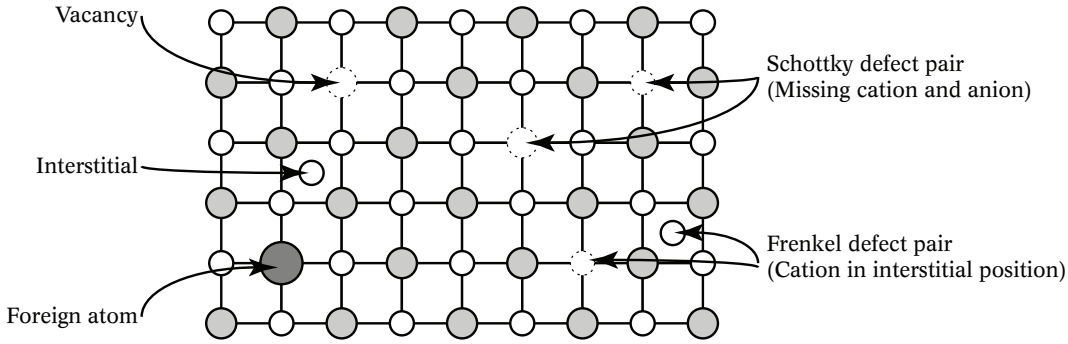

Figure 2.1 *– Examples of both intrinsic and extrinsic point defects.*

1-dimensional defects
1-dimensional defects, or dislocations, constitute of two main types of defects: Edge dislocations and screw dislocations. Edge dislocations appear where an extra half-plane of atoms is introduced inside the crystal. A screw dislocation can be thought of as a crystal, cut along a plane before slipping one half of the plane across the other by a single lattice vector. Dislocations are sometimes called line defects.

2- and 3-dimensional defects
2-dimensional defects, or plane defects, include inner and outer surfaces, grain boundaries and stacking faults. Inclusions and secondary phases are examples of 3-dimensional defects.

Electronic defects
Electronic defects include negatively charged electrons and positively charged electron holes. Electronic conductivity is defined by the transport of electrons and holes. Transport of electrons gives rise to n-type conductivity, while transport of electron holes gives rise to p-type conductivity.

2.1.2 Lattice diffusion of point defects

When point defects move through a crystalline sample it is called lattice diffusion of point defects. This diffusion may require several different

diffusion mechanisms. Most real samples contain different types of point defects. The point defects often prefer various types of diffusion mechanisms due to their difference in charge, mass and electronic structure. In addition to lattice diffusion, defects may diffuse along grain boundaries, surfaces and dislocations. Rate of diffusion is controlled by several variables like temperature, grain size, pressure and structure.

Vacancy mechanism

In the vacancy mechanism, an atom sitting on an ordinary lattice position jumps into- and occupies a nearby vacancy. This atom may have any charge and may be cationic, anionic or neutral. The atom should be roughly the same size as the vacancy it displaces in order for a successful jump to be made.

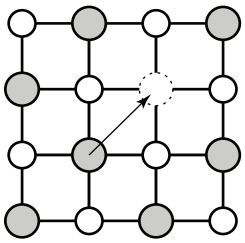

Figure 2.2 *– The Vacancy mechanism*

Interstitial mechanism

If the diffusing atom is small compared to the atoms in normal lattice positions, the interstitial mechanism is often dominating. In this diffusion mechanism, an interstitial atom simply moves from interstitial position to interstitial position.

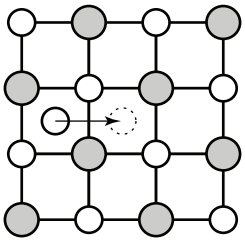

***Figure 2.3** – The Interstitial mechanism*

Interstitialcy mechanism
In the interstitialcy- or indirect interstitial mechanism, a self-interstitial atom pushes an ordinary lattice atom into an interstitial position. At the same time the originally interstitial atom occupies the empty space from the atom it pushed away. The net result is that a self-interstitial has moved from one interstitial site to another.

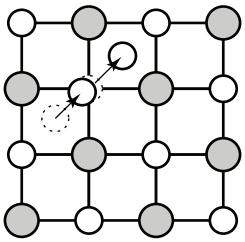

***Figure 2.4** – The Interstitialcy mechanism*

Proton diffusion
When a hydrogen atom is absorbed into a structure it usually loses its electron and turns into a proton. Protons have too large charge densities to exist as separate entities in the structure and tend to associate with electronegative atoms, like oxygen ions, in the parent structure. Protons therefore do not use any of the above diffusion mechanisms, but instead have two diffusion mechanisms of their own. They are called the free proton mechanism and the vehicle mechanism.

In the free proton mechanism (Grotthuss mechanism), protons jump from oxygen atom to oxygen atom after having rotated to correct position between two oxygen atoms. In the vehicle mechanism protons attach to oxygen ions. The now formed hydroxide ions diffuse through the structure, much like ordinary oxygen ions. Hydroxide ions possibly

have lower activation energy of diffusion than oxygen ions due to their smaller size. Hydroxide ions can diffuse through the structure using, the already discussed, vacancy diffusion or interstitial diffusion.

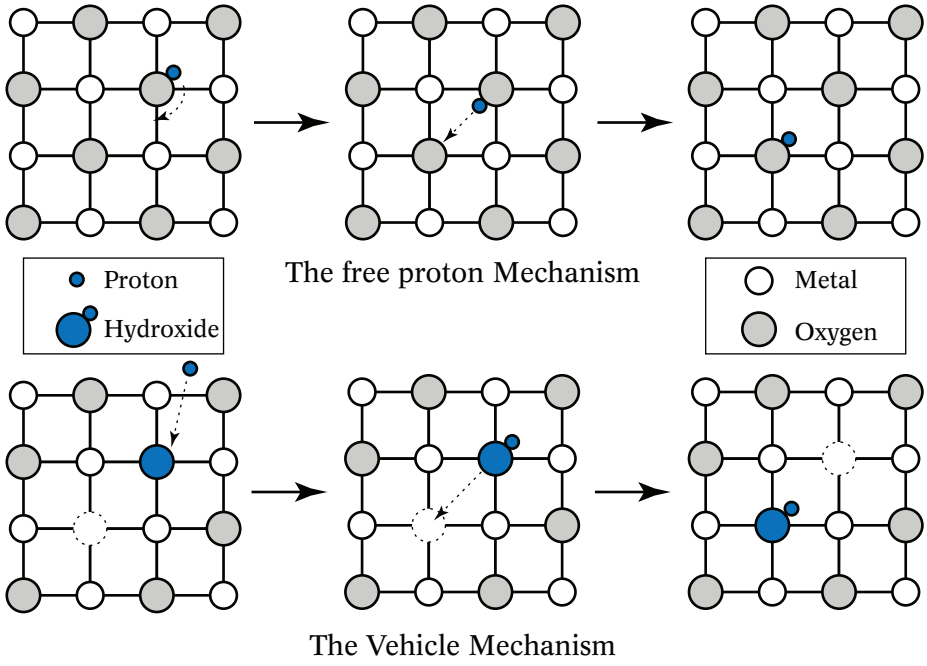

Figure 2.5 *– Proton diffusion mechanisms*

2.1.3 Kröger-Vink notation

The most commonly used defect notation system today is the Kröger-Vink notation, developed by Kröger and Vink [21][22]. Kröger-Vink notation is an assembly of rules used to describe both electrical charge and lattice positions of point defects in crystals. Kröger-Vink notation has three constituents:

$$A_B^C \qquad (2.1)$$

The main symbol (A) describes the chemical content of the point defect. This can be a single element, a molecule, a vacancy (v) or an electrical species (electron (e) or hole (h)). The subscript ($_B$) defines the site in the lattice that is occupied by the point defect; it can be an interstitial site (i) or a site normally occupied by a chemical element or molecule. Finally,

the superscript (^{C}) gives the charge relative to the perfect lattice. The symbol '×' is used to describe null charge. One $^{\bullet}$ indicates a single positive charge, $^{\bullet\bullet}$ indicates double positive charge. One $^{/}$ indicates a single negative charge, while $^{//}$ indicates double negative charge.

Table 2.1 *– Examples of Kröger-Vink notations*

Examples	Explanations
$La_{La}^{\times}$	A lanthanum ion on a lanthanum ion site, having a neutral charge. This is a part of the parent lattice.
$Ta_{Nb}^{\times}$	A tantalum ion on a niobium ion site, having a neutral charge.
$v_O^{\bullet\bullet}$	An oxygen vacancy having a double positive charge.
$Ca_i^{\bullet\bullet}$	A calcium interstitial having a double positive charge.
$e^{/}$	A free electron

In writing defect equations it is important to remember the following three rules:

The law of mass action:
The total number and types of atoms should be evenly matched on each side of the equation. Vacancies and electrons do not usually count to the balance of mass, in order to simplify equations.

Electroneutrality
The total effective charge on each side of the equation should be the same. This can be stated mathematically as:

$$\sum_{i} z(i^2) \qquad (2.2)$$

Where i is any charged species and z is its charge.

Conservation of site ratio
The ratios between cation lattice sites and anion lattice sites in the host structure must be kept constant. Annihilation or formation of lattice sites is only allowed if these ratios are maintained.

2.1.4 Defects in acceptor doped $LaNbO_4$ and $LaTaO_4$

$LaNbO_4$ and $LaTaO_4$ show the same types of possible defects. In the following, only the defects in $LaNbO_4$ will be considered. The defects in $LaTaO_4$ can be described by exchanging Ta for Nb in the equations.

Anionic and cationic vacancies and interstitials are examples of defects in ionic, crystalline materials. Of these four, only oxygen vacancies are of importance when describing the effect of defects on proton conductivity in $LaNbO_4$.

Oxygen vacancies can form stoichiometrically by means of frenkel defects. Frenkel defects are not important for the total defect situation in $LaNbO_4$:

$$O_O^\times = O_i'' + v_O^{\bullet\bullet} \qquad (2.3)$$

$$K_1 = K_F = \left[O_i''\right] \cdot [v_O^{\bullet\bullet}] \cdot [O_O^\times]^{-1} \qquad (2.4)$$

Or they can be formed by exchanging oxygen gas with the surrounding atmosphere:

$$O_O^\times = v_O^{\bullet\bullet} + 2e' + \tfrac{1}{2}O_2(g) \qquad (2.5)$$

$$K_2 = K_{v_O^{\bullet\bullet}} = [v_O^{\bullet\bullet}] \cdot n^2 \cdot p_{O_2}^{1/2} \cdot [O_O^\times]^{-1} \qquad (2.6)$$

This illustrates that the oxygen partial pressure, pO_2, of the surrounding atmosphere directly influences the concentration of oxygen vacancies and electronic defects in the material. It is possible to increase the concentration of oxygen defects in the crystal even further by substituting the native La-cations with a foreign cation of lower valence. This is called acceptor doping. In this study, calcium was used as acceptor dopant:

$$2CaO + Nb_2O_5 = 2Ca_{La}' + 2Nb_{Nb}^\times + v_O^{\bullet\bullet} + 7O_O^\times \qquad (2.7)$$

$$K_3 = K_{Ca_{La}'} = \left[Ca_{La}'\right]^2 \cdot [Nb_{Nb}^\times]^2 \cdot [v_O^{\bullet\bullet}] \cdot [O_O^\times]^7 \qquad (2.8)$$

If the amount of dopant being added to the parent phase is below the solubility limit, the dopant concentration will be constant and independent from temperature and the surrounding atmospheric conditions. If the concentration of dopant is above the solubility limit, the amount of dopant will depend on several variables, like oxygen partial pressure, water partial pressure and equilibrium with a secondary phase. In this work, the concentration of dopant was held below the solubility limit, and thus independent from surrounding conditions.

As protons dissolve into the structure of $LaNbO_4$, oxygen vacancies are being replaced by protons. For $LaNbO_4$ this effect is insignificant under dry conditions but increasingly important as conditions get wetter. Protons are not considered to be structural elements of oxides at higher temperatures and are therefore assumed to be associated with oxide ions, $OH_O^{\bullet}$:

$$H_2(g) + 2O_O^{\times} = 2OH_O^{\bullet} + 2e^{/} \quad (2.9)$$

$$K_4 = K_{H_2} = [OH_O^{\bullet}]^2 \cdot n^2 \cdot p_{H_2}^{-1} \cdot [O_O^{\times}]^2 \quad (2.10)$$

$LaNbO_4$ may also dissolve protons by interacting with water vapor. The equilibrium between protons and oxygen vacancies in this case can be represented by the following point-defect reaction:

$$H_2O(g) + v_O^{\bullet\bullet} + O_O^{\times} = 2OH_O^{\bullet} \quad (2.11)$$

$$K_5 = K_{hydr} = [OH_O^{\bullet}]^2 \cdot p_{H_2O}^{-1} \cdot [v_O^{\bullet\bullet}]^{-1} \cdot [O_O^{\times}]^{-1} \quad (2.12)$$

It is thus important to observe that both the partial pressure of oxygen, pO_2, (2.5) and the partial pressure of water, pH_2O, (or partial pressure of hydrogen) in the surrounding atmosphere influences the total concentration of protons and other defects in the structure.

For electronic defects, the following intrinsic ionization is always true:

$$0 = e^{/} + h^{\bullet} \quad (2.13)$$

$$K_6 = K_i = n \cdot p \quad (2.14)$$

The final defect to consider is the replacement of Nb with increasing amounts of Ta in the $LaNbO_4$-phase. As the solubility limit is passed, a secondary $LaTaO_4$-phase may show up. This “doping” of Ta in $LaNbO_4$ does not give any other defects because the effective charges are neutral:

$$LaTaO_4 = La_{La}^{\times} + Ta_{Nb}^{\times} + 4O_O^{\times} \quad (2.15)$$

$$K_7 = K_{Ta_{Nb}^{\times}} = [La_{La}^{\times}] \cdot [Ta_{Nb}^{\times}] \cdot [O_O^{\times}]^4 \quad (2.16)$$

By combining all the available charged defect species in the $LaNbO_4$-system, at the experimental conditions, the total electroneutrality for defects in this system may be written as follows:

$$2[v_O^{\bullet\bullet}] + [OH_O^{\bullet}] + p = [Ca_{La}^{/}] + n \quad (2.17)$$

2.1.5 Concentration of defects as a function of pO_2

In dry atmospheres, where $[OH_O^{\bullet}]$ may be considered minority defects and the partial pressure of water is low, there are three distinct defect situations dictated by the partial pressure of oxygen; low pO_2, medium pO_2 and high pO_2.

In the low pO_2-situation, eq. (2.5) is shifted to the right and oxygen vacancies together with electrons become majority defects. This is an intrinsic defect situation where it may be assumed that

$$n \gg [Ca_{La}^{/}] \quad \text{and} \quad 2[v_O^{\bullet\bullet}] \gg p, [OH_O^{\bullet}]$$

Eq. (2.17) thus simplifies into:

$$2[v_O^{\bullet\bullet}] = n \qquad (2.18)$$

The concentrations of majority defects in the low pO_2-situation can be found by inserting this into the equilibrium equation for formation of oxygen vacancies, eq. (2.6):

$$2[v_O^{\bullet\bullet}] = n = \left(2K_{v_O^{\bullet\bullet}}\right)^{1/3} p_{O_2}^{-1/6} \qquad (2.19)$$

While the concentration of the negative minority defect, $[Ca_{La}^{/}]$, is constant, the concentrations of the two positive minority defects ($p, [OH_O^{\bullet}]$) are found by merging eq. (2.19) with eq. (2.12) and (2.14):

$$[OH_O^{\bullet}] = \left(\frac{1}{4}K_{v_O^{\bullet\bullet}}\right)^{1/6} K_{hydr}^{1/2}\, p_{H_2O}^{1/2}\, p_{O_2}^{-1/12} \qquad (2.20)$$

$$p = K_i\left(2K_{v_O^{\bullet\bullet}}\right)^{-1/3} p_{O_2}^{1/6} \qquad (2.21)$$

In the medium pO_2-situation, the material encounters an extrinsic situation where concentrations of defects are mainly determined by the concentration of acceptor dopant. In this situation the following simplifications can be made:

$$[Ca_{La}^{/}] \gg n \quad \text{and} \quad 2[v_O^{\bullet\bullet}] \gg p, [OH_O^{\bullet}]$$

Eq. (2.17) thus simplifies into:

$$[Ca_{La}^{/}] = 2[v_O^{\bullet\bullet}] \qquad (2.22)$$

The concentrations of the majority defects, $[Ca_{La}^{/}]$ and $[v_O^{\bullet\bullet}]$, in the medium pO_2-situation are therefore seen to be independent of pO_2 and

pH_2O, but strictly dependent on the concentration of dopant. Concentrations of minority defects, $[OH_O^{\bullet}]$, n and p may be found by merging eq. (2.22) with equations (2.12), (2.6) and (2.14):

$$[OH_O^{\cdot}] = \left(\frac{1}{2}K_{hydr}\right)^{1/2}\left[Ca_{La}^{/}\right]^{1/2} p_{H_2O}^{1/2} \qquad (2.23)$$

$$n = 2^{1/2}\left[Ca_{La}^{/}\right]^{-1/2} K_{v_O^{\bullet\bullet}}^{1/2} p_{O_2}^{-1/4} \qquad (2.24)$$

$$p = 2^{-1/2}\left[Ca_{La}^{/}\right]^{1/2} K_i\, K_{v_O^{\bullet\bullet}}^{-1/2} p_{O_2}^{1/4} \qquad (2.25)$$

In the high pO_2-situation, the defect situation in the material is again intrinsic. Eq. (2.5) is shifted to the left meaning that oxygen vacancies and electrons become minority defects while $\left[Ca_{La}^{/}\right]$ and p become majority defects. In this case the electronic majority and minority defects are solely determined by the concentration of dopant, $\left[Ca_{La}^{/}\right]$:

$$p = \left[Ca_{La}^{/}\right] \qquad (2.26)$$

$$n = \left[Ca_{La}^{/}\right]^{-1} K_i \qquad (2.27)$$

The ionic minority defects, $[v_O^{\bullet\bullet}]$ and $[OH_O^{\bullet}]$, can be found by merging eq. (2.26) with equations (2.6), (2.12) and (2.14):

$$[v_O^{\bullet\bullet}] = \left[Ca_{La}^{/}\right]^2 K_{v_O^{\bullet\bullet}} K_i^{-2} p_{O_2}^{-1/2} \qquad (2.28)$$

$$[OH_O^{\cdot}] = \left[Ca_{La}^{/}\right]\left(K_{v_O^{\bullet\bullet}} K_{hydr}\right)^{1/2} K_i^{-1}\, p_{H_2O}^{1/2}\, p_{O_2}^{-1/4} \qquad (2.29)$$

2.1.6 Concentration of defects as a function of pH_2O

As already observed, in eq. (2.12), the defect concentrations in $LaNbO_4$ and $LaTaO_4$ are not only functions of pO_2, but also functions of the water partial pressure, pH_2O, of its surrounding atmosphere. Increasing its pH_2O leads to an increasing concentration oxygen-bound protons, $OH_O^{\bullet}$, in the structures (eq. (2.11)). This is a positively charged defect which, according to the electroneutrality principle, has to be balanced by one or more negative defects. According to eq. (2.17) there are only two important negative defects in these systems: n and $Ca_{La}^{/}$.

At constant oxygen partial pressure, two distinct defect situations, dictated by the partial pressure of water in the surrounding atmosphere, can be differentiated.

In dry conditions (low pH_2O and therefore low $[OH_O^{\bullet}]$), keeping the pO_2 low enough to warrant the following assumption (eq. (2.5)):

$$2[v_O^{\bullet\bullet}] \gg p$$

One may conclude that the two majority defects are $[Ca_{La}^{/}]$ and $[v_O^{\bullet\bullet}]$. Eq. (2.17) thus simplifies into:

$$2[v_O^{\bullet\bullet}] = [Ca_{La}^{/}] \qquad (2.30)$$

Merging this with eq. (2.12) the following dependency of the minority defect $[OH_O^{\bullet}]$ on pH_2O is observed:

$$[OH_O^{\bullet}] = \left(\frac{1}{2}K_{hydr}\right)^{1/2} [Ca_{La}^{/}]^{1/2} p_{H_2O}^{1/2} \qquad (2.31)$$

Concentrations of electronic minority defects can be found by merging eq. (2.30) with (2.6) and (2.14). These defects are seen to be independent of pH_2O:

$$n = 2^{1/2}[Ca_{La}^{/}]^{-1/2} K_{v_O^{\bullet\bullet}}^{1/2} p_{O_2}^{-1/4} \qquad (2.32)$$

$$p = 2^{-1/2}[Ca_{La}^{/}]^{1/2} K_i\, K_{v_O^{\bullet\bullet}}^{-1/2} p_{O_2}^{1/4} \qquad (2.33)$$

As conditions get wetter, the concentration of $OH_O^{\bullet}$-defects increase with increasing pH_2O. In very wet conditions it is assumed that every $OH_O^{\bullet}$-ion is compensated by one $Ca_{La}^{/}$, and that both of these defects are majority defects, so that:

$$[OH_O^{\bullet}] = [Ca_{La}^{/}] \qquad (2.34)$$

The minority defects in the wet situation are dependent on pH_2O and can be found by inserting (2.34) into eq. (2.12), (2.6) and (2.14):

$$[v_O^{\bullet\bullet}] = K_{hydr}^{-1}\left[Ca_{La}^{/}\right]^2 p_{H_2O}^{-1} \quad (2.35)$$

$$n = K_{hydr}^{1/2} K_{v_O^{\bullet\bullet}}^{1/2} \left[Ca_{La}^{/}\right]^{-1} p_{O_2}^{-1/4} p_{H_2O}^{1/2} \quad (2.36)$$

$$p = K_i K_{hydr}^{-1/2} K_{v_O^{\bullet\bullet}}^{-1/2} \left[Ca_{La}^{/}\right] p_{O_2}^{1/4} p_{H_2O}^{-1/2} \quad (2.37)$$

2.1.7 Concentration of defects as a function of temperature

As already discussed above, the equilibrium constants for the defects in a sample are dependent on the partial pressures of the surrounding atmosphere. The constants are also dependent on the temperature of the sample. This can be expressed:

$$\ln K_x = \frac{\Delta S_x}{R} - \frac{\Delta H_x}{RT} \quad (2.38)$$

Where K_x is the equilibrium constant, ΔS_x is the entropy and ΔH_x is the enthalpy for the formation of a defect of type x.

2.1.8 Brouwer diagrams

The use of Brouwer diagrams makes it possible to display the complete defect situation for both pH_2O- and pO_2-dependency on a single page. These diagrams show the separate defect concentrations as functions of partial gas pressures. The diagrams are, like the equations in the preceding chapter, simplified to have two distinct zones when the gas is H_2O (dry and wet) and three distinct zones when the gas is O_2 (low-, medium- and high pO_2). The scales are arbitrary and should only be viewed as such.

By comparing conductivity data from measurements to the theoretical Brouwer diagrams one can get a better understanding of the actual defect situation in a sample.

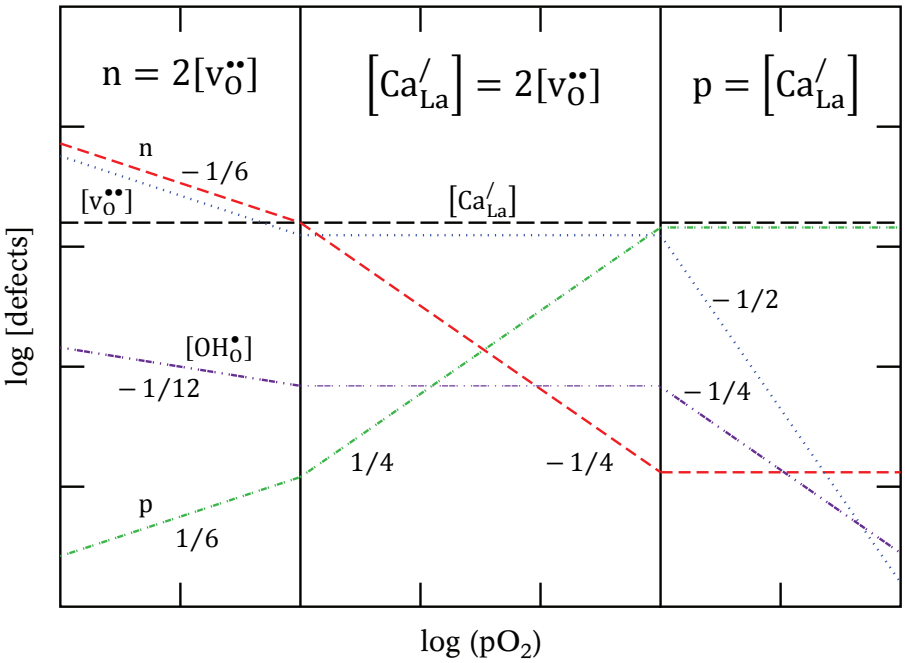

Figure 2.6 *- Concentration of defects as a function of pO_2 for Ca-doped $LaNbO_4$ and $LaTaO_4$. The units are arbitrary.*

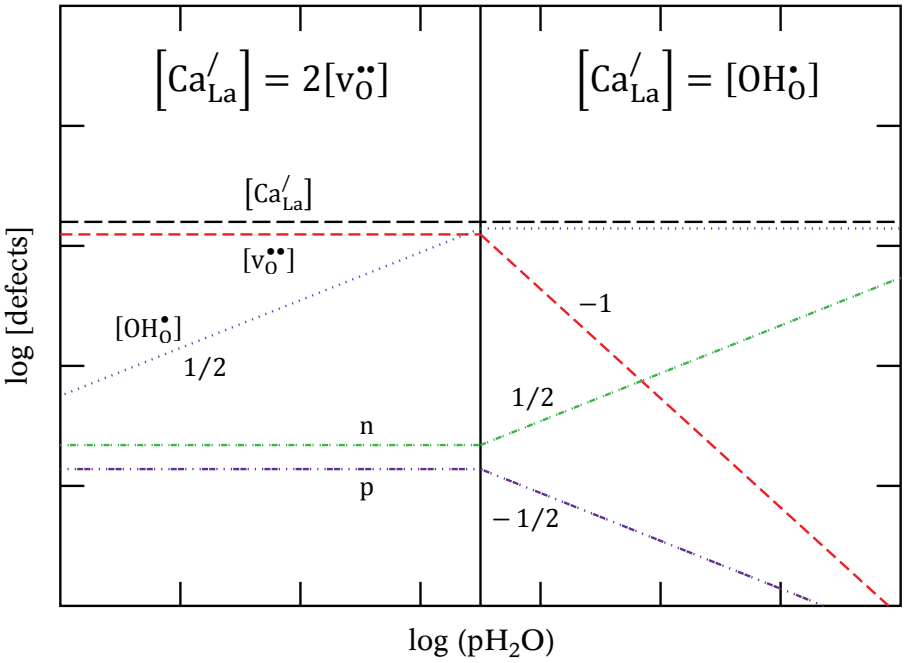

Figure 2.7 *- Concentration of defects as a function of pH_2O for Ca-doped $LaNbO_4$ and $LaTaO_4$. The units are arbitrary.*

2.2 Electrical conductivity

The ability of a material to conduct electrically charged species is called its electrical conductivity or specific conductance. Conductivity is the inverse of resistivity. The conductivity of any specie, for instance charged oxygen vacancies, $\sigma_{v_O^{\bullet\bullet}}$, is defined as the ratio of the current density, $J_{v_O^{\bullet\bullet}}$, to the electric field strength, E. In general for any specie, i:

$$J_i = \sigma_i E \qquad (2.39)$$

Furthermore, conductivity, σ_i, is proportional to the charge of the specie, $z_i e$, concentration of the specie, c_i, and mobility of the specie, u_i. This leads to the complete equation:

$$J_i = \sigma_i E = z_i e c_i u_i E \qquad (2.40)$$

The SI-unit for conductivity is Siemens per meter, S/m (Ohm^{-1}/m). Due to the fact that most samples in the laboratory are in the cm-range, the unit of Siemens per cm, S/cm, is often encountered as well. In samples containing different charge carriers, the total conductivity is calculated by combining the individual conductivities from each charge carrier. In the samples used in this thesis the total conductivity is:

$$\sigma_{tot} = \sum_i \sigma_i = \sigma_{v_O^{\bullet\bullet}} + \sigma_{OH_O^{\bullet}} + \sigma_{Ca_{La}^{/}} + \sigma_{e/} + \sigma_{h^{\bullet}} \qquad (2.41)$$

The transport number of charge carrier is a measure of its contribution to total conductivity and is defined to be the ratio of the individual charge carrier's conductivity to total conductivity:

$$t_i = \frac{\sigma_i}{\sigma_{tot}} \qquad (2.42)$$

The sum of transport numbers equals unity.

The mobility of any charge carrier, moving through a polar material according to the activated hopping mechanism, can be deduced from diffusion theory. By using the Nernst-Einstein relation one can relate self diffusion coefficient of species i, D_i, to its conductivity, σ_i, and charge carrier mobility, u_i:

$$\frac{D_i}{kT} = \frac{u_i}{z_i e} = \frac{\sigma_i}{c_i (z_i e)^2} \quad (2.43)$$

Where k is Boltzmann's constant, T is temperature, z is charge, e is the elementary charge and c is concentration of species i. Since the temperature dependency of the self diffusion coefficient is partially given by its hopping frequency, and the hopping frequency is proportional to the Boltzmann distribution factor, it is seen that the charge carrier mobility, and therefore also conductivity has Arrhenius types of temperature dependencies:

$$u_i = \frac{u_0}{T} e^{\frac{-\Delta H_{mob}}{RT}} \quad (2.44)$$

$$\sigma_i = \frac{\sigma_0}{T} e^{\frac{-\Delta H_a}{kT}} \quad (2.45)$$

In this, ΔH_{mob} is the charge carrier's enthalpy of mobility and ΔH_a is the activation energy for conduction. σ_0 is a pre-exponential containing several factors related to the diffusing species and the structure it is diffusing through.

2.2.1 Alternating current (AC)

In contrast to the simple unidirectional flow of charge in direct current (DC) systems, the flow of current in AC-systems is alternating in the forward and backward directions as a function of time. This can lead to effects not observed in DC-systems. The general expression for voltage in sinusoidal AC-systems is as follows:

$$U = U_0 \cdot \sin(\omega t) \quad (2.46)$$

U_0 is the amplitude or peak voltage. The sinusoidal element contains angular frequency, ω (radians per second), and time, t (in seconds). This expression is seen to describe DC-voltage if its angular frequency is 0. The current in AC-systems is only in phase with the voltage if no capacitive or inductive elements are present in the circuit. (These elements are explained in 2.2.2) The general expression for current in sinusoidal AC-systems is as follows:

$$I = I_0 \cdot \sin(\omega t + \theta) \quad (2.47)$$

I_0 is the peak current (unit: Ampere) and θ is the phase change caused by capacitive or inductive elements. ω and t are the same as in (2.46).

While DC-systems only contain real conductivity and resistivity, AC-systems have additional contributions from imaginary, 90° out of phase susceptance and reactance. Susceptance is the imaginary version of conductivity, while reactance is the imaginary version of resistance.

The combination of conductance and susceptance is called admittance, while the combination of resistance and reactance is called impedance. Both are complex numbers and can be described as vectors in the complex plane. Impedance is a more generic expression than resistance and may be used for both DC-systems and AC-systems, in phase or out of phase.

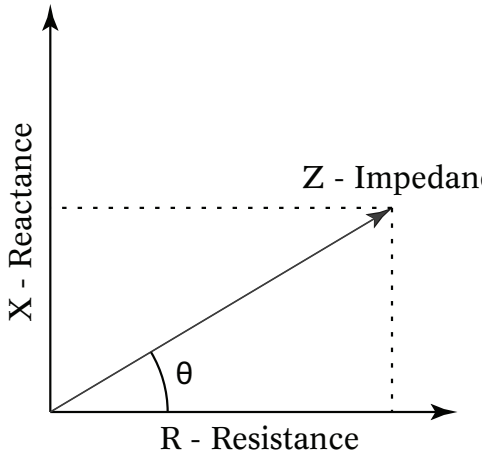

Figure 2.8 *– AC Impedance*

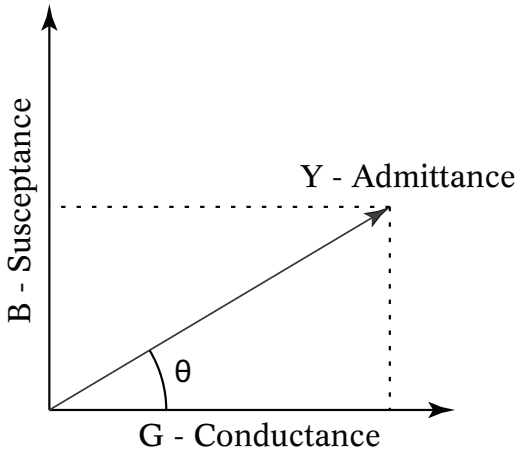

Figure 2.9 *– AC Admittance*

Due to the unique properties of AC impedance and its imaginary parts, the amount of information that can be extracted from a sample's electronic structure using AC is much improved over using DC.

2.2.2 Passive circuit elements

It is possible, in any electrical network or circuit, to isolate multiple interconnected electrical elements. Each element may affect either the current through the network or the voltage in the network in some way. In contrast to real electrical components, circuit elements do not physically exist, and are assumed to have ideal properties.

There are two main types of electrical elements; active elements and passive elements. The difference between the two is that passive elements cannot generate power nor act as power sources while active

elements can. Active elements used to model the likes of field effect transistors are not discussed in this thesis.

Four different passive elements are defined, three of which are of importance for this thesis. The three are Resistance, Capacitance and Inductance. The fourth element, Memristance, is rarely encountered. Due to the non-ideal nature of electrochemical processes a fifth "quasi"-circuit element, the Constant Phase Element, may be introduced in order to simplify matters.

Resistance

Resistance R is measured in ohms, Ω. Resistance produces a voltage across each element proportional to the current flowing through it. The electrical component corresponding to resistance is the resistor. Current and voltage through a resistor will be in phase and the resistor will only contribute to the real part of impedance:

$$R = \frac{U}{I} = \frac{U_0 \sin\ \omega t}{I_0 \omega t} = \frac{U_0}{I_0} \qquad (2.48)$$

The combined resistance of two resistors in series equals the sum of the two, while for two resistors in parallel the combined inverse resistance is the sum of the inverse resistances. An ideal resistor is a conductor in which the current flowing through instantly sets up a voltage across it.

Capacitance

Capacitance C is measured in farads, F. Capacitance produces a current through each element proportional to the rate of change of voltage across it. The electrical component corresponding to capacitance is the capacitor. A simple capacitor consists of a slab of a dielectric sandwiched between two parallel conductive plates. If A is the area and L is the distance between the plates, the capacitance of a capacitor will be given by:

$$C = \varepsilon \frac{A}{L} \qquad (2.49)$$

A capacitor stores electrical energy proportional to the voltage applied across it and subsequently discharges the energy back into the circuit if the voltage is removed. This property leads to the ability of an alternating current (AC) flowing through a capacitor to set up a voltage lagging 90° behind the current. Due to the phase difference between current and voltage, a capacitor may contribute to the imaginary part of the impedance. The frequency dependent reactance, X, is given by:

$$X = -\frac{1}{\omega C} \qquad (2.50)$$

Inductance

Inductance L is measured in henries, H. Inductance produces a voltage across each element proportional to the rate of change of current through it. The electrical component corresponding to inductance is the inductor. A simple inductor consists of a conducting wire shaped as coil. This shape acts to produce a strong magnetic field in the centre of the coil which induces a voltage across the conductor. The induced voltage leads the current by 90° and thus gives an imaginary contribution to the impedance, called reactance. The frequency dependent reactance, X, is given by:

$$X = \omega L \qquad (2.51)$$

Memristance

The recently developed fourth element, Memristor (short for memory resistor), will not be used in this thesis. Memristance M produces a current such that the rate of change of current through the element is proportional to the rate of change of voltage across it. This means that at any given instant, a memristor is a resistor, but if a charge passes through it, it will change its resistance accordingly. Its resistance is proportional to the charge that has passed through it. It can forever "remember" what resistance it had at the moment no more charge was passed through it. The memristor was first mentioned in a paper by Chua in 1971 [23], but was first realized as a physical object in 2008 by HP Labs [24].

Constant phase element (CPE)

As already stated, the non-ideal nature of real samples may necessitate the introduction of one or more constant phase elements in addition to the four original passive circuit elements. CPEs were discovered in the 1940's by studying the electrical response of real samples of dielectrics. Observing that the responses did not match any other circuit elements, one saw the need to invent a new type of circuit element. Several explanations for CPE behavior have been put forward. They all explain CPE behavior by pointing to some property of the system being inhomogeneous. Examples of the latter are surface roughness, different grain sizes, -shapes and –boundaries and dual layer capacitance. The impedance of a CPE is defined to be

$$Z = \frac{1}{Y} = \frac{1}{Y_0(j\omega)^n} \qquad (2.52)$$

Y_0 has the numerical value of $1/|Z|$ at $\omega=1$ rad/s, ω is frequency and n can take any value from -1 to 1. A constant phase elements is a very general electrical element: A pure capacitor can be described as a CPE where n=1, a pure resistor can be described as a CPE where n=0 and a pure inductor can be described as a CPE where n=-1.

2.2.3 Electrochemical impedance spectroscopy

The use of Electrochemical Impedance Spectroscopy makes it possible to characterize physico-chemical systems like electrochemical fuel cell materials. Amongst other things, the method makes it possible to distinguish conductivity of grains from conductivity of grain boundaries in polycrystalline materials. Additionally it makes it possible to observe any contribution to the impedance from electrodes used in the experimental setup.

Electrochemical Impedance Spectroscopy works by examining the impedance of a sample over a range of AC frequencies (Typically from 1 MHz to 0.01 Hz). The frequency response of the sample is thus mapped. As the conductivities of bulk, grain boundaries and electrodes tend to have different time dependencies, different conductivities will dominate at different frequencies. The complete impedance sweep over a number of frequencies is often displayed in the form of a Nyquist plot.

In this kind of plot the y-axis corresponds to the imaginary part of impedance (reactance) with increasingly negative numbers above the x-axis while the x-axis corresponds to the real part of impedance (resistance). The highest frequencies are close to- or at the origin. As the frequencies change, the phasor quantities change. At each measured frequency, the angle corresponds to the phase change, θ, of the current, while the distance from origin corresponds to the magnitude of impedance.

Nyquist plots of real polycrystalline samples often have three arches or semicircles, sometimes with a “tail” close to origin. (Figure 2.10) Starting at origin the “tail” is an inductive element, L, caused by inductance in the wiring setup. The first semicircle describes bulk impedance. The second semicircle describes grain boundary impedance and the third and last describes electrode impedance. The semicircles are often somewhat overlapping and may be difficult to separate. Each semicircle can be modeled by a parallel combination of a resistor and a

capacitor, an (RC)-combination. If a semicircle has its centre below the x-axis in a Nyquist plot, the fit can be improved by replacing the capacitor with a constant phase element, an (RQ)-combination. A typical n-value for polycrystalline materials with many grain boundaries is $n = 0.80$.

A semicircle's highest imaginary point is called its characteristic frequency and is given by [25]:

$$\omega_{cf} = \frac{1}{RC} = \frac{1}{\frac{L}{\sigma A}\frac{\varepsilon_0 \varepsilon_r A}{L}} = \frac{\sigma}{\varepsilon_0 \varepsilon_r} \qquad (2.53)$$

The equation for the characteristic frequency of an (RQ)-combination is different from that of an (RC)-combination (2.53):

$$\omega_{cf} = \frac{1}{(R\,Y_0)^{1/n}} \qquad (2.54)$$

It is seen that this equation is identical to (2.53) if $n = 1$. The true capacitance for an (RQ)-combination is found by merging (2.53) into (2.54) :

$$C = \frac{1}{R\omega_{cf}} = R^{(1/n\,-1)}\,{Y_0}^{1/n} \qquad (2.55)$$

This reduces back to [26]:

$$C = Y_0(\omega_{cf})^{n-1} \qquad (2.56)$$

Finally, if one considers each semicircle to be a parallel combination of passive elements and each semicircle to be connected to the next by a serial connection, one can, by using the brick layer model, calculate the amount of energy being stored and dissipated in the grain bulk, grain boundaries and electrode connections.

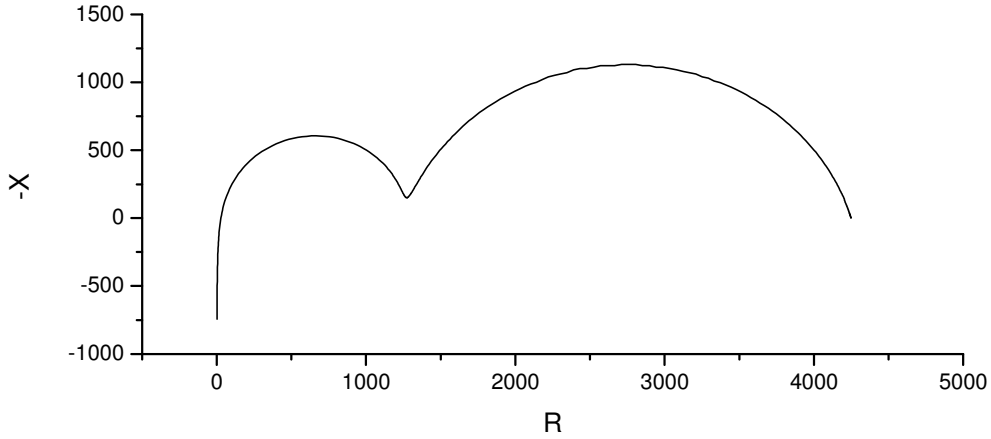

Figure 2.10 *– A typical impedance sweep showing two semicircles corresponding to bulk impedance (left) and grain boundary impedance (right). The tail to the far left corresponds to an inductive element. In this example there are no semicircles corresponding to electrode impedance.*

2.2.4 Brick layer model

In the so-called brick layer model, polycrystalline samples are assumed to consist of cubic grains sandwiched in-between sidewise homogenous grain boundaries.

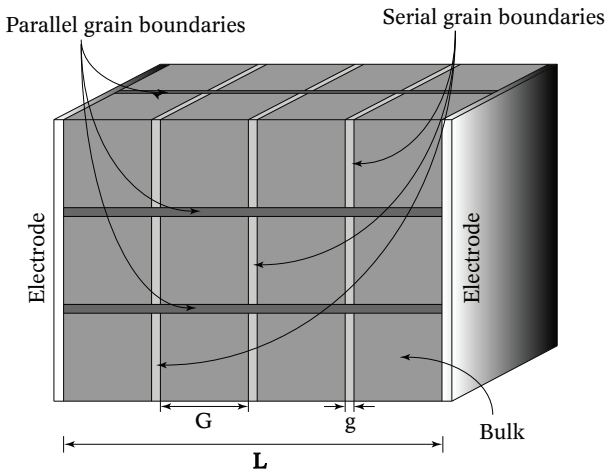

Figure 2.11 *– The brick layer model for polycrystalline materials. Modified from* [27].

Charge carriers can in theory pass through either bulk or the lengthwise grain boundaries. In any case they have to pass through crossing grain boundaries. All grain boundaries are assumed to have identical properties. When adding up the complete sets of bulk and grain boundary contributions to conductivity, two distinct systems emerge; one has bulk conductivity, the other one has lengthwise grain boundary conductivity. The following equivalent circuit together with its simplified version sums up the situation:

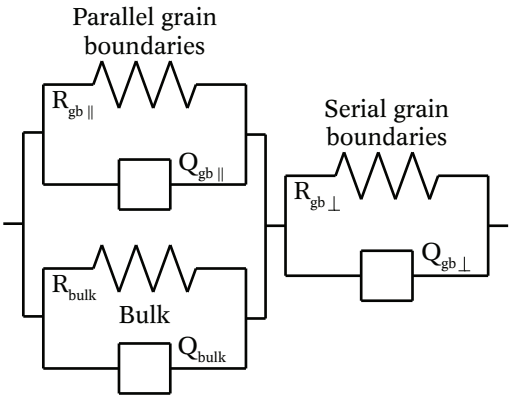

Figure 2.12 *– The equivalent Circuit for the brick layer model.*

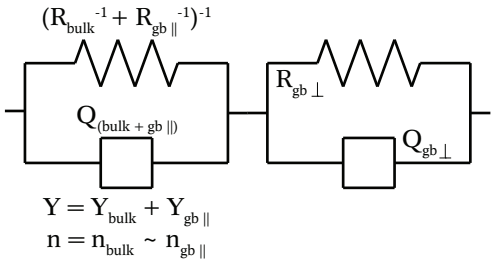

Figure 2.13 *– The simplified equivalent Circuit for the brick layer model.*

The bulk- and the lengthwise grain boundary conductivity-situations can be described by the following two equations:

$$\sigma_1 = \frac{1}{R_1} = \frac{2g}{G}\sigma_{gb} + \sigma_{bulk} \qquad (2.57)$$

$$\sigma_2 = \frac{1}{R_2} = \frac{G}{g}\sigma_{gb} \qquad (2.58)$$

The relationship between σ_1 and σ_2 in a sample thus is dependent on both the electrical properties (σ_{gb}, σ_{bulk}) and microstructure (g, G) of the samples' material.

Two requirements have to be fulfilled in order for a Nyquist plot to display the two separate semicircles corresponding to bulk- and grain boundary conductivity: First of all the semicircles need to be of roughly the same size. This happens when the sizes of R_1 and R_2 are roughly the same, or within about two orders of magnitude. Secondly the two

semicircles must have significantly different characteristic frequencies. It can be shown that, for materials with standard microstructure, this can only be the case if $\sigma_{bulk} > \sigma_{gb}$. In this case 2.53 stays the same while 2.52 reduces to:

$$\sigma_1 = \frac{1}{R_1} = \sigma_{bulk} \qquad (2.59)$$

2.2.5 Constant frequency measurements

Due to the significant time consumption of doing a complete impedance sweep at every temperature throughout a series of measurements, a constant frequency measurement is often used instead. During such a measurement, the frequency is locked at a predetermined value, often 10 kHz, while other variables, like temperature and gas compositions, are changed.

If the temperature in a constant frequency measurement is ramped over a large span of several hundred degrees, certain things must be taken into consideration before interpreting the results. In a system such as described in 2.2.4, with two semicircles corresponding to bulk and grain boundary impedance, the characteristic frequencies of both semicircles will change as temperature changes. This means that as temperature changes, the impedance being measured will slowly traverse across the two semicircles. At elevated temperatures, mainly the impedance of the grain boundaries will be measured and at lower temperatures the impedance of the bulk will be measured. This can lead to significant changes in measured impedance at certain temperatures. It is important to know about this effect in order to avoid doing bad interpretations of measurement data. Wrongly ascribing swift impedance changes to changes in the transport of charge carrier types can, for instance, lead to unrealistically high numbers for proton conductivities.

3 Literature

Several types and systems of proton conductors are known. (See chapter 1.3) Of these, $LaNbO_4$ and $LaTaO_4$ stand out because they both, in addition to being good high temperature proton conducting materials, also are able to withstand high levels of humidity and CO_2-containing atmospheres. Because the combination of these properties is interesting and rather unique, their structures, conductivities and defects have recently been under thorough investigation with the ultimate goal of producing a fully working, commercial fuel cell. Recently it was discovered that $LaNbO_4$ and $LaTaO_4$ display solid solubility over large ranges of concentrations.

In this chapter, the available literature on $LaNbO_4$, $LaTaO_4$ and their solid solution will be discussed. This chapter is divided into two main sections; one section containing literature on the structures and one section containing literature on conductivity properties.

3.1 Structures

$LaNbO_4$ and $LaTaO_4$ both have at least two polymorphs. The low temperature polymorph is a monoclinic phase in both cases. At higher temperatures $LaNbO_4$ assumes a tetragonal phase, while $LaTaO_4$ adopts an orthorhombic phase. This section examines available literature on the structures of $LaNbO_4$, $LaTaO_4$ and a combination of the two.

3.1.1 Structure of $LaNbO_4$

$LaNbO_4$ has two different structures depending on temperature [28]. The low temperature phase is monoclinic with a Fergusonite structure while the high temperature phase is tetragonal and has a Scheelite structure. The phase transition between the high- and low temperature structures of $LaNbO_4$ has earlier been identified to be of second order in

nature [29] and reportedly happening in the temperature range of 490°C-530°C [19][29][30][31][32].

The cell parameters for monoclinic $LaNbO_4$ were measured by Vullum et al. [19] and found to be in very good agreement with the values calculated by Tsunekawa et al. [33](Table 3.1):

Table 3.1 *– The cell parameters for monoclinic $LaNbO_4$* [19].

Space group: I2/a (= C2/c = I2/c)			
a (Å)	b (Å)	c (Å)	β (deg)
5.5626(02)	11.519(61)	5.2013(06)	94.06(89)

Atom	**x**	**y**	**z**
La	0	0.6304(33)	0.25
Nb	0	0.1047(83)	0.25
O(1)	0.2265(31)	0.0378(13)	0.0497(30)
O(2)	0.1424(34)	0.2089(13)	0.4827(22)

The y-number for O(1) was published to be 0.378(13) in the study by Vullum et al. [19] This is probably a typographical error and the correct y-number for this atom should read 0.**0**378(13). This number can be compared to the y-number of 0.0337(1) for O(1), calculated by Tsunekawa et al. [33].

Figure 3.1 and Figure 3.2 display the unit cell of monoclinic $LaNbO_4$. The figures make it possible to directly observe the slight displacement of ~4° from a perfectly tetragonal system.

It is possible to create a theoretical powder X-ray diffraction pattern based on the unit cell parameters of any crystalline material. Below, in Figure 3.3, the theoretical powder X-ray diffraction pattern of monoclinic $LaNbO_4$ is displayed. It is based on the numbers from Table 3.1 and created by *Diamond 3.2c* [34].

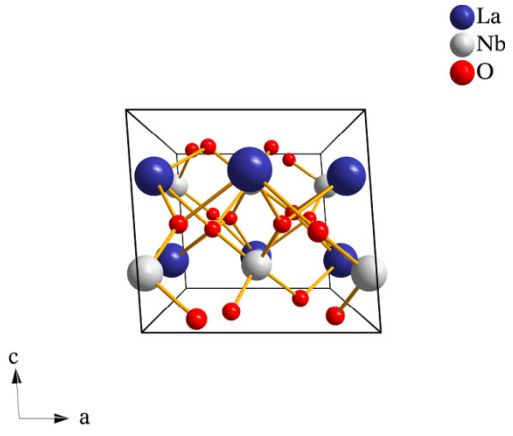

Figure 3.1 *– The unit cell of monoclinic $LaNbO_4$ viewed along its y-axis.*

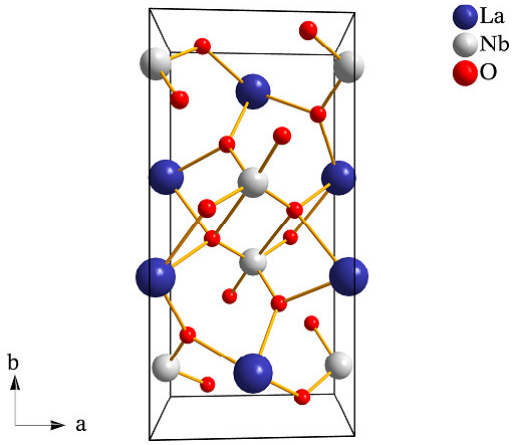

Figure 3.2 *– The unit cell of monoclinic $LaNbO_4$ viewed along its z-axis.*

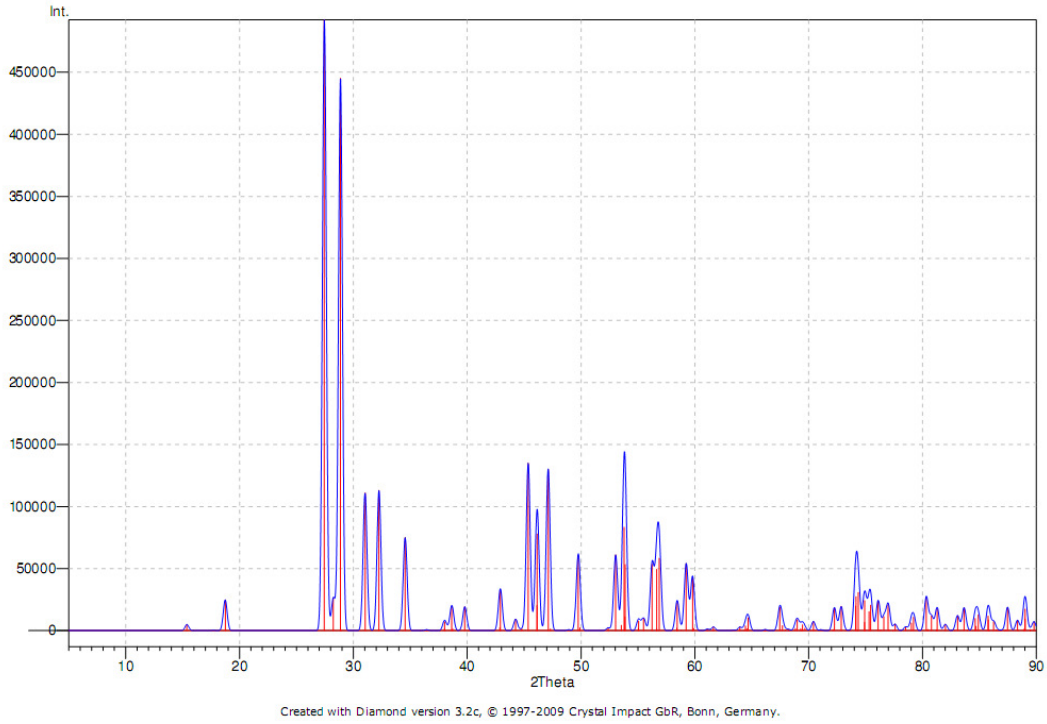

Figure 3.3 *– A theoretical X-ray diffraction pattern for monoclinic $LaNbO_4$ in the 2θ-range of 5° to 90°* [34].

Some of the cell parameters for tetragonal $LaNbO_4$ were measured by Vullum et al. [19] and found to be in very good agreement with the values calculated by David [35] and Prytz and Taftø [36]. The following numbers are from the earlier study by David: (Table 3.2)

Table 3.2 *– The cell parameters for tetragonal$LaNbO_4$ at 500°C* [35].

Space group: $I4_1/a$			
a (Å)		c (Å)	
5.4001(2)		11.6661(2)	
Atom	**x**	**y**	**z**
La	0	0	0.5
Nb	0	0	0
O	0.2441(5)	0.1599(3)	0.0850(3)

Cell parameters calculated by Jian and Wayman [29] are not presented as they show considerable deviations from later studies. At temperatures between 500°C and 600°C the studies by Prytz and Taftø [36] display somewhat different cell parameters when compared to the more recent study by Vullum et al. [19], but are very similar at all other temperatures.

Figure 3.4 and Figure 3.5 display the unit cell of the high-temperature polymorph of $LaNbO_4$, projected along its y- and z-axes.

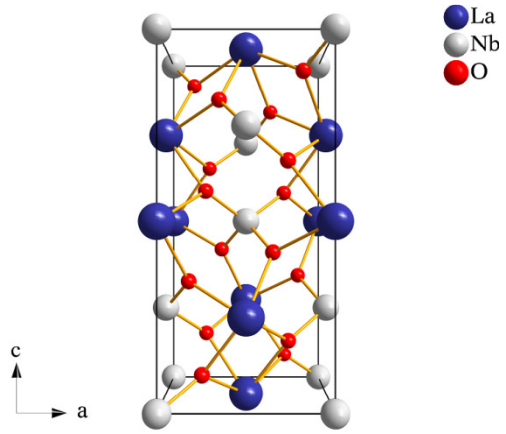

Figure 3.4 *– The unit cell of tetragonal $LaNbO_4$ viewed along its y-axis.*

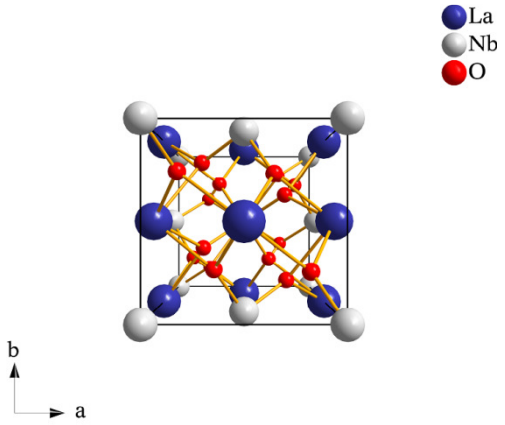

Figure 3.5 *– The unit cell of tetragonal $LaNbO_4$ viewed along its z-axis.*

3.1.2 Structure of $LaTaO_4$

$LaTaO_4$ exists as at least two different polymorphs; if prepared with the solid state method two phases, one monoclinic and one orthorhombic, coexist at room temperature. The powder can be transformed into a monoclinic single phase if a pressure of 150-170MPa is applied to the powder before sintering. A phase transition to a pure orthorhombic polymorph has been found to take place at ~250°C [19][37][38][39]. No higher temperature polymorphs have been reported below 1450°C for $LaTaO_4$ [30].

The cell parameters for monoclinic $LaTaO_4$ were measured by Vullum et al. [19] and found to be in agreement with values calculated by Hartenbach et al.[38] and Kurova et al.[39] (Table 3.3):

Table 3.3 *– The cell parameters for monoclinic* $LaTaO_4$ [19].

Space group: $P2_1/c$			
a (Å)	b (Å)	c (Å)	β (deg)
7.6281(81)	5.5781(02)	7.8203(71)	101.533(80)

Atom	**x**	**y**	**z**
La	0.3412(71)	0.7743(94)	0.0964(42)
Ta	0.1686(61)	0.2644(74)	0.3007(22)
O(1)	0.1706(19)	0.1713(27)	0.0618(24)
O(2)	0.0507(23)	0.5779(29)	0.2104(22)
O(3)	0.3783(20)	0.4843(29)	0.3245(21)
O(4)	0.3352(19)	0.9947(30)	0.3592(20)

Based on the numbers from Table 3.3 one can draw the unit cell for monoclinic $LaTaO_4$ (Figure 3.6 and Figure 3.7) and create its theoretical powder X-ray diffraction pattern. (Figure 3.8)

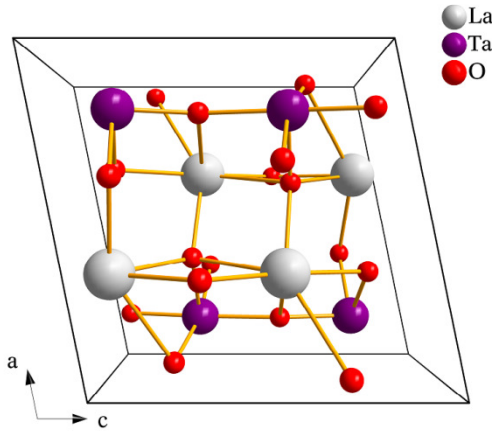

Figure 3.6 *– The unit cell of monoclinic $LaTaO_4$ viewed along its y-axis.*

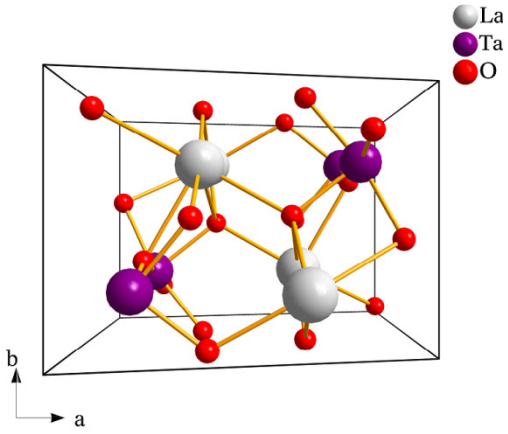

Figure 3.7 *– The unit cell of monoclinic $LaTaO_4$ viewed along its z-axis.*

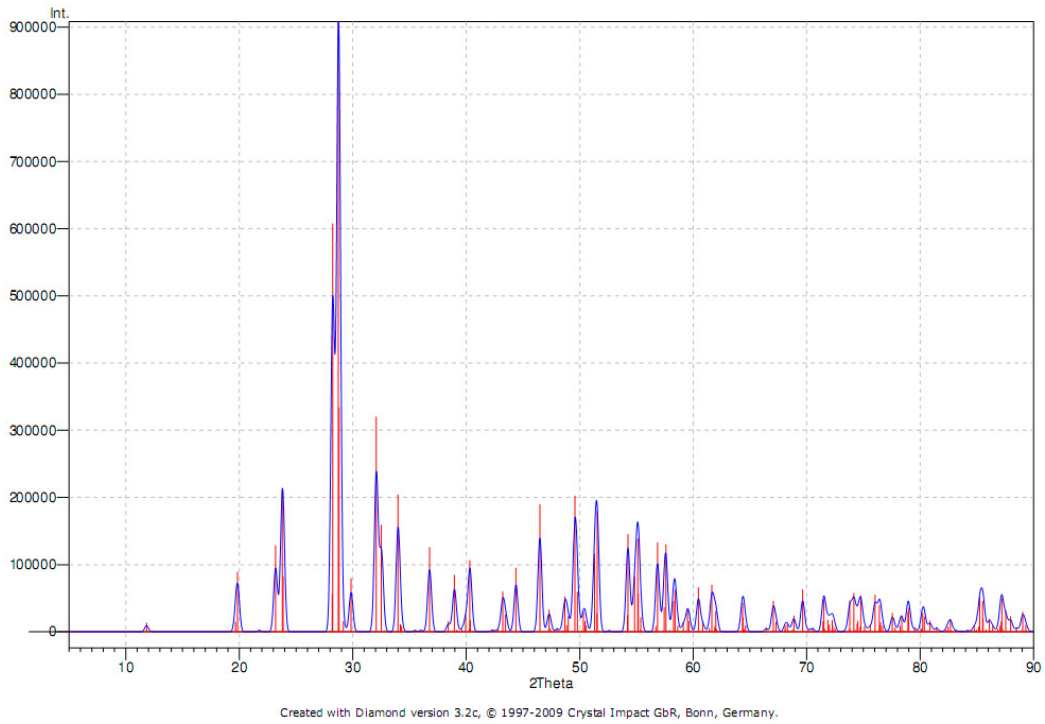

Figure 3.8 *– A theoretical X-ray diffraction pattern for monoclinic $LaTaO_4$ in the 2θ-range of 5° to 90°* [34].

The cell parameters for orthorhombic $LaTaO_4$ were also measured by Vullum et al. [19], and found to be in agreement with values calculated by Cava and Roth (Table 3.4) [37]:

Table 3.4 *– The cell parameters for orthorhombic $LaTaO_4$* [19].

Space group: $A2_1am$			
a (Å)	b (Å)	c (Å)	
5.6415(82)	14.719(51)	3.9404(41)	
Atom	**x**	**y**	**z**
La	0.171(28)	0.1682(24)	0
Ta	0.212(30)	0.4144(24)	0
O(1)	0.422(32)	0.3077(54)	0
O(2)	0.949(42)	0.3381(55)	0
O(3)	0.563(18)	0.4724(75)	0
O(4)	0.2496	0.9055(51)	0

The theoretical powder X-ray diffraction pattern for orthorhombic $LaTaO_4$ (Figure 3.11) displays some recognizable features not present in the pattern for monoclinic $LaTaO_4$ (Figure 3.8), (for instance a small peak at 30°, and a single, large peak at 38°), and vice versa. (Twin peaks at 32° and a single peak at 37°) This is a rather simple and easy way to tell them apart. Both patterns are significantly different from the one for monoclinic $LaNbO_4$ (Figure 3.3). This should, by the use of XRD, make it easy to recognize any secondary phases in the samples.

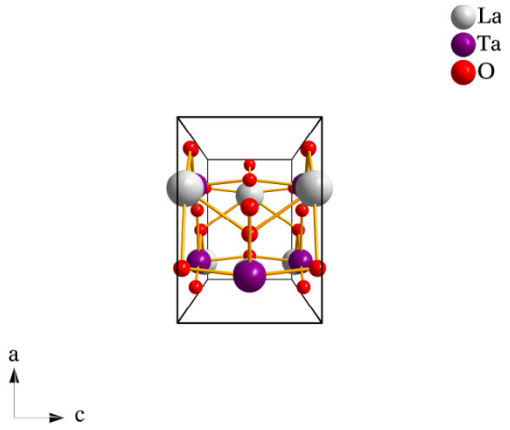

Figure 3.9 *– The unit cell of orthorhombic $LaTaO_4$ viewed along its y-axis.*

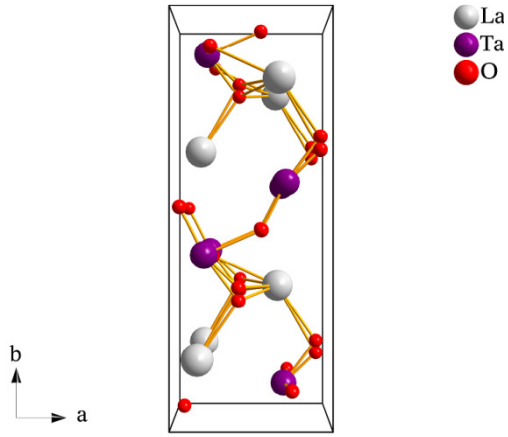

Figure 3.10 *– The unit cell of orthorhombic $LaTaO_4$ viewed along its z-axis.*

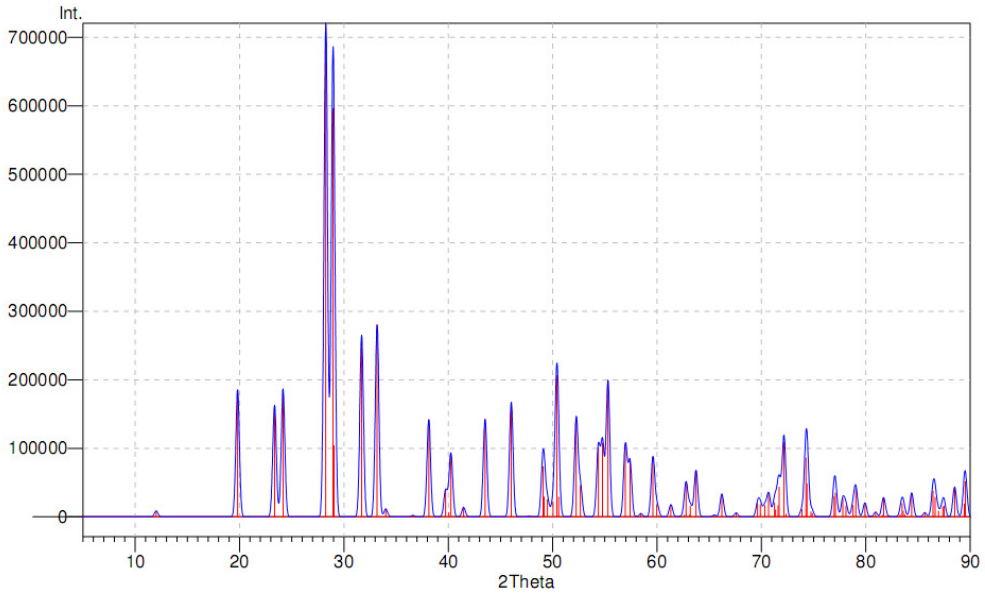

Figure 3.11 *– A theoretical X-ray diffraction pattern for orthorhombic $LaTaO_4$ in the 2θ-range of 5° to 90°* [34].

3.1.3 Structure of the $LaNbO_4$ – $LaTaO_4$ system

Recent investigations have shown that $LaNbO_4$ and $LaTaO_4$ display complete solid solubility over large ranges of concentrations. A Study by

Vullum et al. [19] shows that, if the concentration of $LaTaO_4$ is kept equal to, or below 40%, $LaTaO_4$ dissolves completely into a $LaNbO_4$-phase. Additionally, if the concentration of $LaNbO_4$ is kept equal to, or below 20%, $LaNbO_4$ dissolves completely into a $LaTaO_4$-phase. A qualitative analysis showed that a solid solubility limit exists somewhere between $LaNb_{0.6}Ta_{0.4}O_4$ and $LaNb_{0.5}Ta_{0.5}O_4$ on the Nb-rich side and between $LaNb_{0.3}Ta_{0.7}O_4$ and $LaNb_{0.2}Ta_{0.8}O_4$ on the Ta-rich side. In between these concentrations a two-phase region exists. Table 3.5 sums it up:

Table 3.5 *– Phase distribution in the $LaNbO_4$-$LaTaO_4$ –system* [19].

$LaNb_{1-x}Ta_xO_4$	**Result**
$0 \leq x \leq 0.4$	Single $LaNbO_4$-phase
$0.5 \leq x \leq 0.7$	Two-phase area; both $LaNbO_4$-phase and $LaTaO_4$-phase
$0.8 \leq x \leq 1$	Single $LaTaO_4$-phase

It was seen that as the concentration of $LaTaO_4$ in the $LaNbO_4$-phase increased, the phase transition temperature also increased. While $LaNbO_4$ has a phase transition temperature of roughly 500°C, $LaNb_{0.6}Ta_{0.4}O_4$ has a phase transition temperature of roughly 800°C. This increase in phase transition temperature could be favorable for fuel cells as it would increase the possible working temperature of the cell without dealing with any change in thermal expansion coefficient (TEC) as phase boundaries are crossed. The cell parameters were also seen to change significantly as more and more $LaTaO_4$ was added to the $LaNbO_4$-phase.

A big change in TEC is experienced as $LaNbO_4$ changes from one phase to another. A less severe change in TEC was experienced as higher concentrations of $LaTaO_4$ were added to the $LaNbO_4$-phase. A less severe change in TEC across the monoclinic-tetragonal phase boundary would make it easier to match the rest of the materials, needed to make a working fuel cell, to the TEC of the $LaNbO_4$-electrolyte. Still, the thermal expansion of the $LaNbO_4$ monoclinic phase was shown to be significantly higher than for the tetragonal phase. Any cathode and anode materials being connected to a $LaNbO_4$-phase should be synthesized according to this. Table 3.6 gives a full review on the changes in both monoclinic and tetragonal TEC as the concentration of $LaTaO_4$ in the $LaNbO_4$-phase is varied. The TEC for monoclinic

$LaNbO_4$ decreases as more $LaTaO_4$ is added, while the TEC for tetragonal $LaNbO_4$ increases as $LaTaO_4$ is added.

Table 3.6 *– Change in TECs as the concentration of $LaTaO_4$ is varied* [19].

	TEC monoclinic (10^{-6} °C^{-1})	TEC tetragonal (10^{-6} °C^{-1})	T_c (°C)
$LaNbO_4$	17.3±0.5	7.1±0.7	510±10
$LaNb_{0.8}Ta_{0.2}O_4$	15.7±0.3	9.1±0.1	670±10
$LaNb_{0.6}Ta_{0.4}O_4$	14.0±0.2	11.5±1	800±10

On the Ta-rich side it was seen that as the concentration of Nb decreased, the phase transition temperature between the monoclinic and the orthorhombic phases increased. Figure 3.12 displays a simplified phase diagram for the $LaNbO_4$ – $LaTaO_4$ –system.

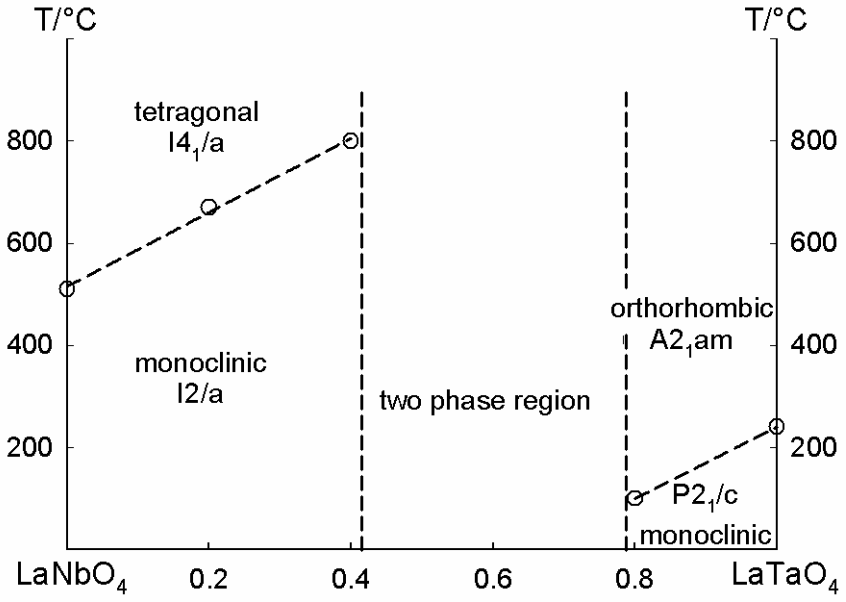

Figure 3.12 *– A simplified phase diagram for the $LaNbO_4$ – $LaTaO_4$ phase system. Experimentally measured points are marked with circles* [19].

It is of importance to note that the complete $LaNbO_4$ – $LaTaO_4$ –system phase diagram probably does not look like the simplified phase diagram

in Figure 3.12. Rarely, if ever, does a phase diagram contain such straight lines between regions of one and two phases. This has to do with the temperature dependency of the entropy of mixing.

3.2 Defects and conductivity

The high proton conductivities in $LaNbO_4$ and $LaTaO_4$ were only very recently discovered [20]. The complete sets of possible defects and their equations were dealt with earlier in chapter 2.1. This section will give a thorough literature review on known defects and conductivities in both $LaNbO_4$ and $LaTaO_4$.

3.2.1 Defects and conductivity in $LaNbO_4$

In measurements made by Teterin et al. on different undoped rare-earth niobates, it was seen that the conductivity of undoped $LaNbO_4$, depending on temperature and partial pressure of oxygen, had contributions from both ionic and electronic partial conductivities.[40] A later, more thorough study by Haugsrud and Norby modeled the conductivities of Ca^{2+} doped $LaNbO_4$ and presented its good proton conductivity [4].

The total conductivity of $LaNbO_4$ as a function of pO_2 using wetted gases ($pH_2O = 0.025$ atm) is displayed in Figure 3.13 a). When total conductivity does not change with changing oxygen partial pressure, it implies areas of mainly ionic conductivity, while the areas where the conductivity increases with pO_2 imply electronic contributions to total conductivity. By comparison with Figure 2.6 it is clear that the electronic contributions to total conductivity are of p-type.

Figure 3.13 b) displays the total conductivity of $LaNbO_4$ as a function of water vapor pressure, pH_2O. At higher temperatures $LaNbO_4$ shows much less dependency on the water vapor pressure than at lower temperatures. This could imply that protons from water vapor contribute significantly less to the total conductivity at higher temperatures than lower (< 1000°C) temperatures. If this is combined with the results from Figure 3.13 a) and the defect situations listed in chapter 2.1, one can assume that at temperatures above 1200°C, the main contribution to total conductivity increasingly stems from oxide ions. Figure 3.14 b) seems to agree with this.

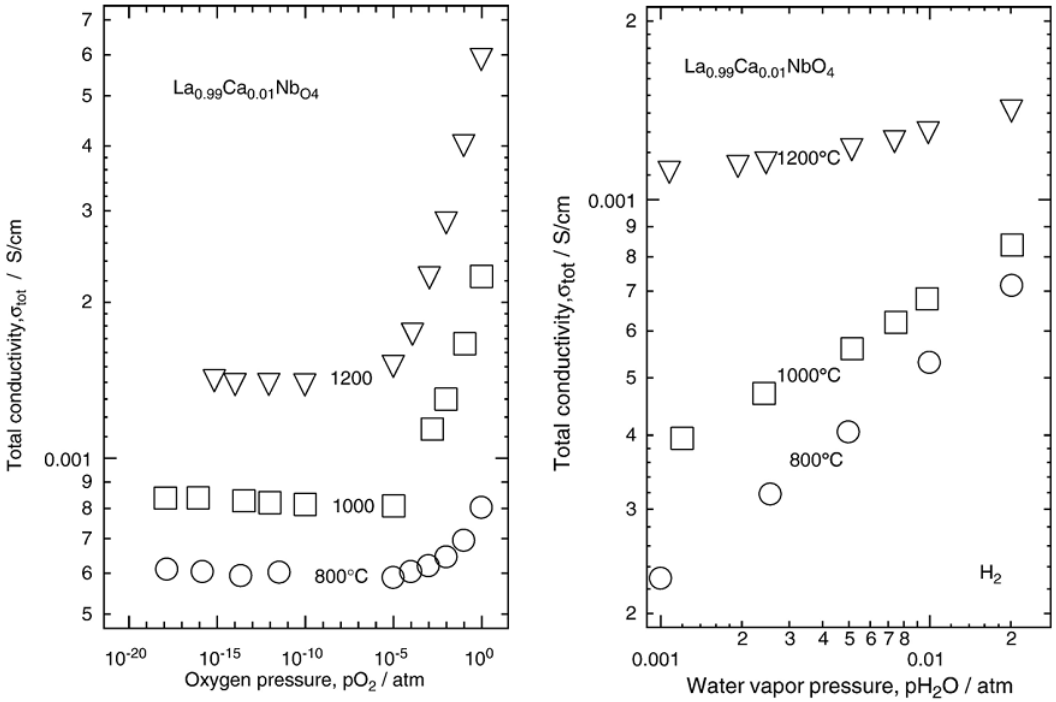

Figure 3.13 *– Total conductivity as a function of the oxygen partial pressure (a) and water partial pressure (b) at 800, 1000 and 1200 °C for* $La_{0.99}Ca_{0.01}NbO_4$ [4].

In Figure 3.14 a), temperature ramps in wet/dry O_2 and wet H_2 are displayed for $La_{0.99}Ca_{0.01}NbO_4$. Here, total conductivities are displayed as functions of the inverse absolute temperature. Conductivities for both wet O_2 and wet H_2 have the same magnitude up to a certain temperature. At this temperature oxygen ion and electronic conductivity takes over.

Figure 3.14 b) displays total and partial conductivities of $La_{0.99}Ca_{0.01}NbO_4$ as a function of the inverse absolute temperature under reducing conditions. It is clear that up to roughly 950°C Ca-doped $LaNbO_4$ is mainly a proton conductor, with a maximum proton conductivity of about 10^{-3} S cm^{-1} at 950°C. At temperatures close to 1200°C oxide ions start to take over as the main contribution to total conductivity.

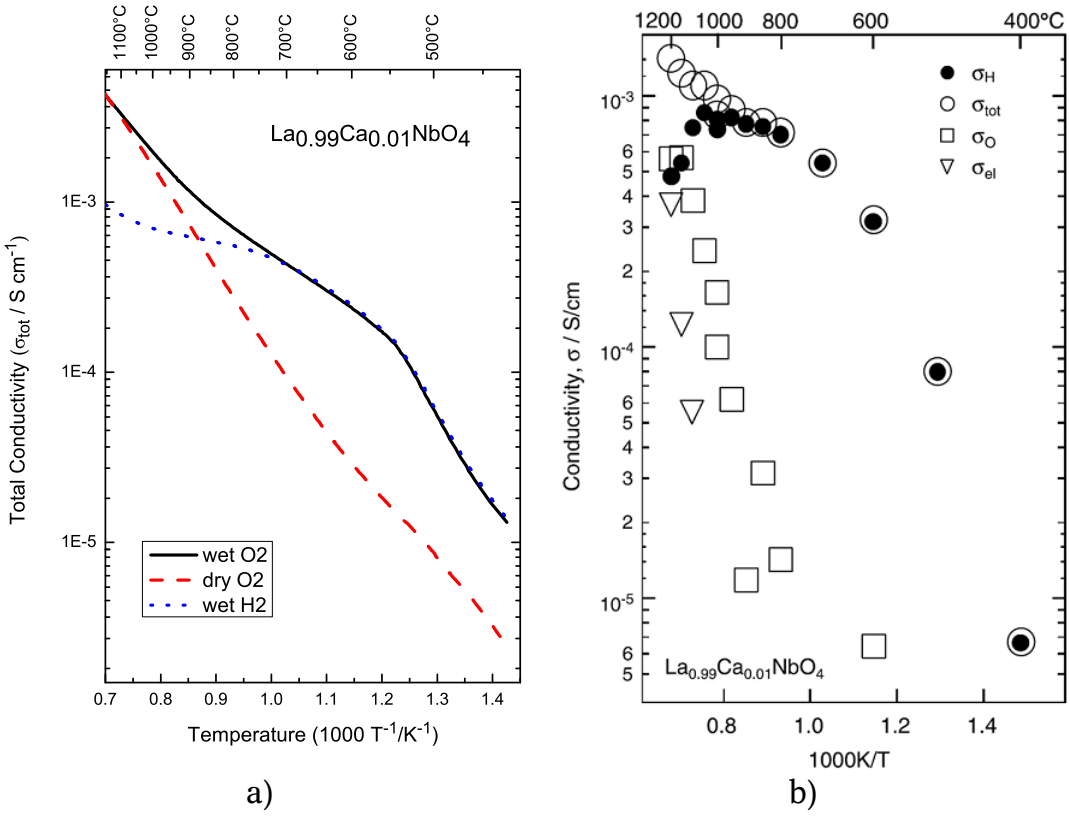

Figure 3.14 *– a) : Ramps in wet/dry O_2 and H_2 for $La_{0.99}Ca_{0.01}NbO_4$, showing total conductivity as a function of inverse temperature* [41]. *b) : Total and partial conductivities as a function of the inverse absolute temperature in the temperature range 400 to 1200 °C under reducing conditions (wet H_2, $La_{0.99}Ca_{0.01}NbO_4$)* [4].

Table 3.7 lists thermodynamic and transport parameters for $LaNbO_4$, extracted from modeling of partial and total conductivity data. The data is valid for reducing conditions.

Table 3.7 *– Thermodynamic and transport parameters extracted from modeling of partial and total conductivity data (wet H_2, $La_{0.99}Ca_{0.01}NbO_4$)* [4].

ΔS_{hydr} [J/mol K]	ΔH_{hydr} [kJ/mol]	$\mu_0(H^+)$ [cm² K/V s]	$\Delta H_{mob}(H^+)$ [kJ/mol]	$\mu_0(O^{2-})$ [cm² K/V s]	$\Delta H_{mob}(O^{2-})$ [kJ/mol]
-130 ± 10	-115 ± 10	35 ± 10	55 ± 5	15 ± 5	60 ± 5

3.2.2 Defects and conductivity in $LaTaO_4$

Until very recently, nothing was known about the conductivities of $LaTaO_4$. In 2006/2007 Haugsrud and Norby, for the first time, measured its conductivities [5][20]. Their findings (Figure 3.16 b)) showed that $LaTaO_4$ displays pure protonic conductivity up to a temperature of around 800°C. Above this temperature oxide ions and electronic conductivities start to dominate total conductivity. $LaTaO_4$'s maximum proton conductivity, of about $2 \cdot 10^{-4}$, is reached at a temperature of ~1000°C.

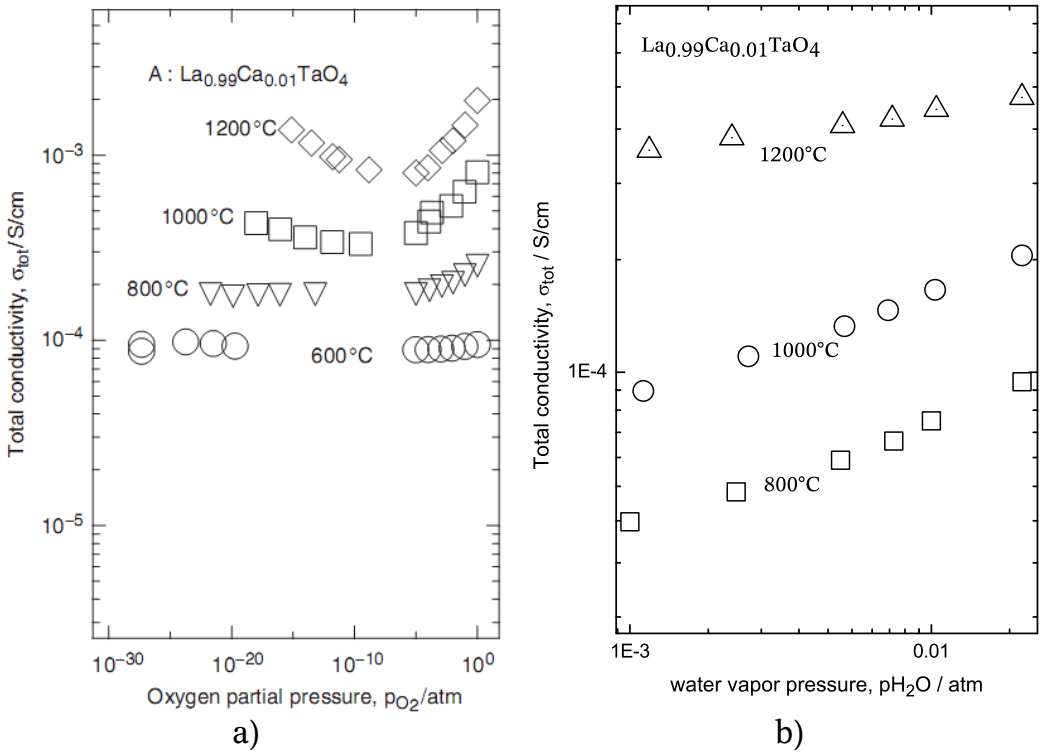

Figure 3.15 *– Total conductivity as a function of the oxygen partial pressure (a)* [5] *and water partial pressure (b)*[41] *at 800, 1000 and 1200 °C for* $La_{0.99}Ca_{0.01}TaO_4$.

Figure 3.15 a) displays the total conductivity of Ca-doped $LaTaO_4$ as a function of the oxygen partial pressure in wet atmospheres (pH_2O = 0.025 atm). At lower temperatures (600°C - 800°C) the total conductivity is mainly ionic with a small p-type electronic contribution to total conductivity at high oxygen partial pressures (Ref Figure 2.6). At higher temperatures and high oxygen partial pressures the p-type

electronic conductivity plays an increasingly significant role. The same trend is apparent at higher temperatures and low partial pressures of oxygen. The only difference from the case of higher oxygen partial pressure is that the electronic contribution to the total conductivity at lower oxygen partial pressures is n-type electronic conductivity.

In Figure 3.15 b) the total conductivity is plotted as a function of water vapor partial pressure. The water partial pressure dependency at any temperature is significantly weaker than corresponding measurements for Ca-doped $LaNbO_4$.

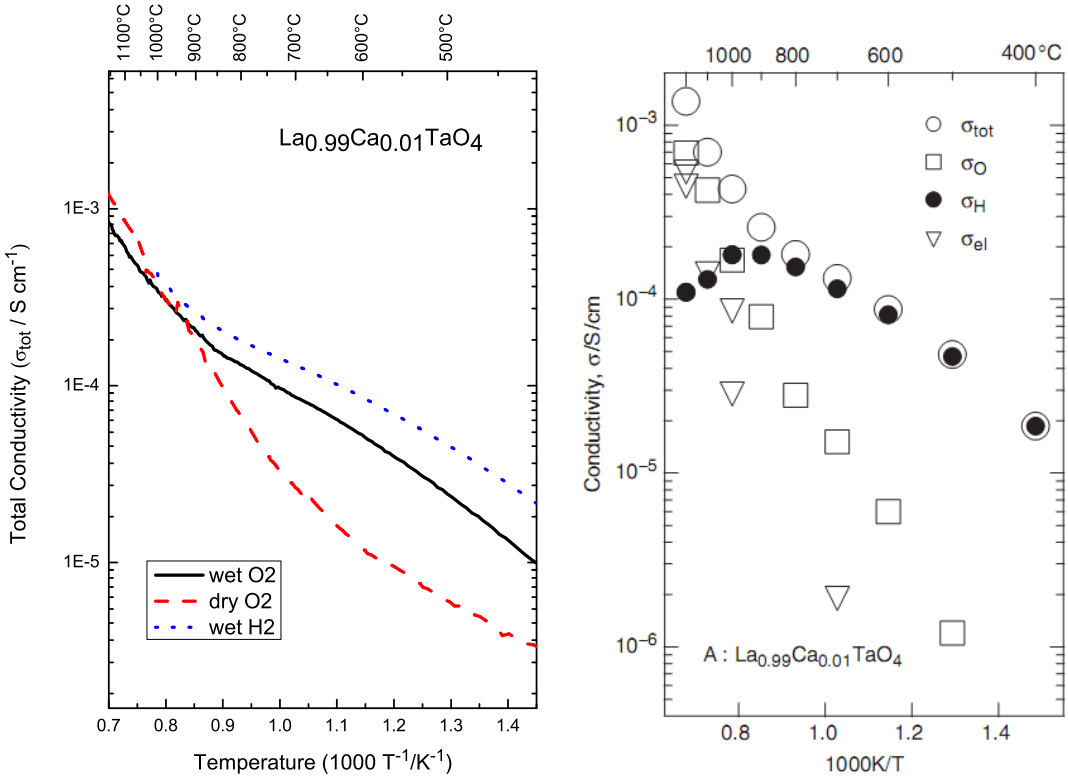

Figure 3.16 *– a) : Ramps in wet/dry O_2 and H_2 for $La_{0.99}Ca_{0.01}TaO_4$, showing total conductivity as a function of inverse temperature* [41] *b) : Total and partial conductivities as a function of the inverse absolute temperature in the temperature range 400 to 1200 °C under reducing conditions (wet H_2, $La_{0.99}Ca_{0.01}TaO_4$)* [5].

Temperature ramps in wet/dry oxygen- and wet hydrogen atmospheres for Ca-doped $LaTaO_4$ are shown in Figure 3.16 a). $LaTaO_4$ have tell-tale signs of proton conductivities at temperatures below ~800°C. Here the wet O_2 and wet H_2 ramps have significantly higher total conductivity than dry O_2. At higher temperatures, oxygen ion and electronic conductivities seem to take over. This is later confirmed in Figure 3.16 b).

Important thermodynamic and transport parameters for $LaTaO_4$ are displayed in Table 3.8. The numbers are extracted from modeling of partial and total conductivity data and are valid for reducing conditions.

Table 3.8 *– Thermodynamic and transport parameters extracted from modeling of partial and total conductivity data (wet H_2, $La_{0.99}Ca_{0.01}TaO_4$)* [5].

ΔS_{hydr} [J/mol K]	ΔH_{hydr} [kJ/mol]	$\mu_0(\mathrm{H}^+)$ [cm^2 K/V	$\Delta H_{mob}(\mathrm{H}^+)$ [kJ/mol]	$\mu_0(\mathrm{O}^{2-})$ [cm^2 K/V s]	$\Delta H_{mob}(\mathrm{O}^{2-})$ [kJ/mol]
-120 ± 10	-100 ± 10	10 ± 5	50 ± 5	15 ± 5	70 ± 5

4 Experimental

For this thesis several samples of differing compositions were synthesized, characterized and measured. The starting materials and compositions of the samples were as follows:

Table 4.1 *– Starting materials for the samples used in this thesis.*

Compound	Producer and purity
La_2O_3	Alfa Aesar, 99,99%
Nb_2O_5	Sigma Aldrich, 99,9%
Ta_2O_5	Sigma Aldrich, 99,99%
$CaCO_3$	Sigma Aldrich, ≥ 99,0%

Table 4.2 *– Sample compositions*

Sample number	Sample composition
Sample 38	$La_{0.99}Ca_{0.01}Nb_{0.62}Ta_{0.38}O_4$
Sample 40	$La_{0.99}Ca_{0.01}Nb_{0.60}Ta_{0.40}O_4$
Sample 42	$La_{0.99}Ca_{0.01}Nb_{0.58}Ta_{0.42}O_4$
Sample 44	$La_{0.99}Ca_{0.01}Nb_{0.56}Ta_{0.44}O_4$
Sample 46	$La_{0.99}Ca_{0.01}Nb_{0.54}Ta_{0.46}O_4$
Sample 48	$La_{0.99}Ca_{0.01}Nb_{0.52}Ta_{0.48}O_4$
Sample 50	$La_{0.99}Ca_{0.01}Nb_{0.50}Ta_{0.50}O_4$

The solid state preparation method was used to synthesize all samples. XRD and SEM were used to characterize samples before electrical measurements, using a gas mixer and probostat™-setup, were carried through.

Due to the hygroscopic nature of La_2O_3, great care was taken to avoid introducing La_2O_3 powder to water in the atmosphere. Before being weighted, powders were dried over night at 600°C.

This chapter will discuss the solid state sample preparation, physical characterizations and electrical characterizations used on the samples. Finally, in the last section of this chapter, a thorough review of conceivable sources of error will be given.

4.1 Solid state sample preparation

Solid state sample preparation, or "shake and bake" as it's sometimes called, is a preparation method based on repeatedly crushing, mixing and heating two or more different starting powders. After each cycle of crushing, mixing and heating, the solid powders react with each other. As the number of calcinations increase, the powders will increasingly deviate from original powder compositions and, if done right, eventually reach desired final chemical composition. This method is widely used in the fields of inorganic chemistry, due to its ease of use and good results.

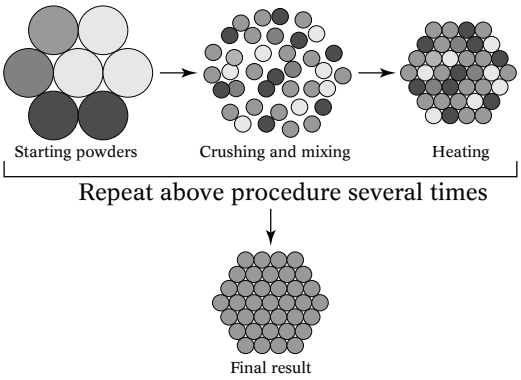

Figure 4.1 *– The solid state sample preparation procedure of repeatedly crushing, mixing and heating powders to get the desired final product composition.*

The importance of each step in the "shake and bake" process will be discussed below.

Starting materials were weighed to correct stoichiometry before being mixed to form each sample. Each sample was calcined three times at 1100°C for 15 hours with intermediate grindings before being sintered at 1500°C for 10 hours. Heating and cooling rates were 300°C/h for both calcination and sintering. (Figure 4.2)

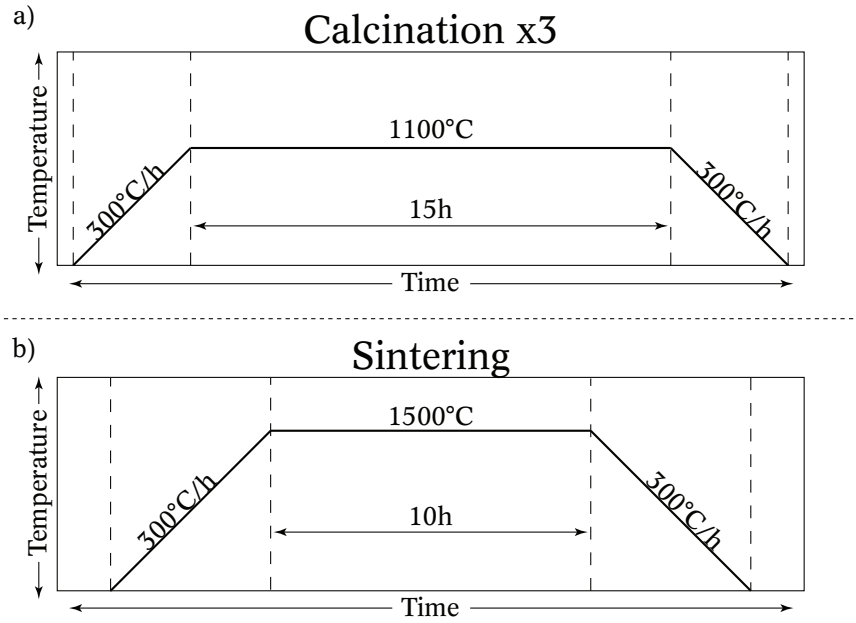

Figure 4.2 *– Calcination- (a) and sintering- (b) programs used for all samples.*

4.1.1 Ball milling

Ball milling is a technique for crushing and grinding materials into very fine powder. In some cases the final powder grain size may be in the lower sub-micron range. The very small grain size in ball milled powders facilitates fast solid state reaction rates. This is mainly due to the increased surface energy and -area of smaller grains, but also due to the fresh reaction surfaces being exposed in newly milled powders.

In this study, agate balls were used as grinding medium within a capped agate cylinder. To avoid excessive silicon contamination in the samples, a milling time of just 15 minutes at 150rpm was chosen. Isopropyl alcohol was used as solvent during the entire synthesis and was later evaporated at 150°C in a heating cabinet, after each process of mixing and grinding.

4.1.2 Calcination and thermal treatment

The goal with a calcination process is to treat a solid material with heat in order to remove a volatile fraction, thermally decompose it or to bring about a phase transition. In most cases the process takes place at a temperature below the materials melting point. In this thesis, thermal treatment was used to decompose $CaCO_3$ into $CaO + CO_2$, but also to help the starting oxides diffuse into each other after each round of ball milling. Before the samples were calcined they were pressed into pellets with a diameter of 13 mm under a uniaxial pressure of 6 metric tons.

4.1.3 Sintering

During sintering, grains in a powder fuse at temperatures below the melting point of the material. A sintering process proceeds through several stages. During stage one, powder grains reduce in surface roughness. The second stage includes so-called neck growth where particles start to fuse together. In the later stages the solid becomes denser and less porous by elimination of pores and other voids. (Figure 4.3)

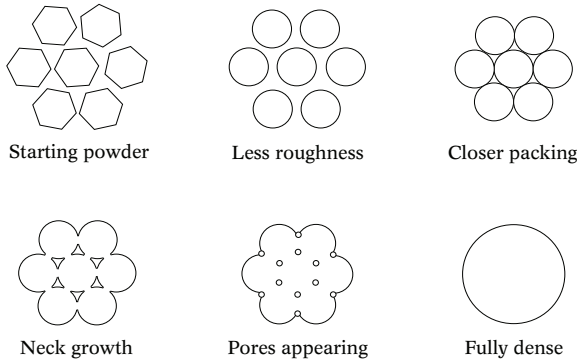

Figure 4.3 *– Stages of the sintering process.*

To successfully make a useful, sintered sample, one should first carefully prepare the powders to get desired composition and particle size. The powders should thereafter be pressed into desired green body shape before being heated to sinter the particles into a solid body. Optimally, this body should be pore free and have the same shape as the originally pressed powders. Each sample being measured in this thesis was thin and cylindrical in shape with diameters of 13 mm. Relative densities varied from ~94% to ~97%.

4.2 Physical characterization

A physical characterization process reveals some of the structural, chemical and topological features of a sample. This section will discuss XRD and SEM, which both were used to extract information from the samples.

4.2.1 Introduction to XRD

XRD, short for X-ray diffraction, is a non-destructive method that can reveal information about chemical composition and crystallographic structures of materials. The technique is based on measuring the elastically scattered intensity of an X-ray beam hitting a sample containing long range order. The intensity being measured is a function of incident angle, scattered angle, polarization and wavelength of the X-ray beam.

Most, if not all, crushed solid materials have a different powder XRD signature. By connecting to an online database containing powder XRD diffraction spectra, the measured powder XRD spectrum can be evaluated and assigned to a material. This database is being maintained by the International Centre for Diffraction Data. Powder XRD is a common way to quickly and easily determine whether the sample you just made contains the material you planned to make. It can also be used to characterize crystallite size, crystallographic structure and preferred orientation in powders and also to determine relative abundance of crystalline compounds in heterogeneous solid mixtures.

4.2.2 Introduction to SEM

A Scanning Electron Microscope produces images of a sample surface by scanning it in a raster pattern using a high-energy electron beam. The electrons interact with the surface to produce, amongst other things, back scattered electrons (BSE), secondary electrons (SE) and X-rays. BSE are electrons being elastically scattered back from the sample. The number of BSEs depends intimately on the atomic number of the atoms being scanned. Heavier and bigger cores scatter more electrons than lighter and smaller cores. Due to this property, BSE imaging can be used to determine distributions of elements in a sample.

When primary electrons from a scanning electron beam interact with the surface of a sample, secondary electrons are kicked out and may hit the detector. The amount of secondary electrons being detected depends on the angle of the scanned surface relative to the primary beam. This

property makes it possible to get a picture of surface topology and gives the characteristic depth of field of a SEM picture.

X-rays are emitted as primary electrons interact with a sample. Since all elements have their own unique electronic structure, each element will have its own characteristic X-ray signature. Characteristic X-rays make the basis for the analytical technique of energy dispersive X-ray spectroscopy, or EDS. This technique is used for elemental analysis of a sample. By detecting relative amounts of characteristic X-rays, the relative concentration of elements in the sample may be determined. In this thesis EDS is only used for qualitative detection of elements, due to the low accuracy using the instrument at hand.

4.3 Electrical characterization

The samples were measured using a Probostat™ sample holder inside an electronically controlled furnace. A gas mixer was used to control partial pressures of different gases, while an impedance spectrometer was used to measure conductivities. Before any conductivity measurements were carried through, all samples were polished and painted with three layers of Pt-ink. A Pt-mesh with a diameter of 10mm was fixed to each sample by Pt-ink to collect current from the sample. Each layer of Pt-ink was dried at 150°C for between 1 and 2 hours. The organics in the layers of ink were finally burned off at 1000°C overnight.

This section starts off with discussing the Probostat™ sample holder. Part two explains the gas mixer, while general conductivity properties are discussed at the end of the section.

4.3.1 Probostat™ sample holder

The Probostat™ sample holder, manufactured by NorECs, is made to fit inside a vertical tube furnace. The outer gas tube is made from quartz, mounted on top of a metal piece containing all the cell's electrical contacts, switches, gas inlets and -outlets. Inside the quartz tube the sample is supported on an alumina tube, which itself is attached to the cells lower metal parts. A spring load attached to an alumina plate is used to sandwich the sample against two measuring electrodes; one on each side of the sample. (Figure 4.4)

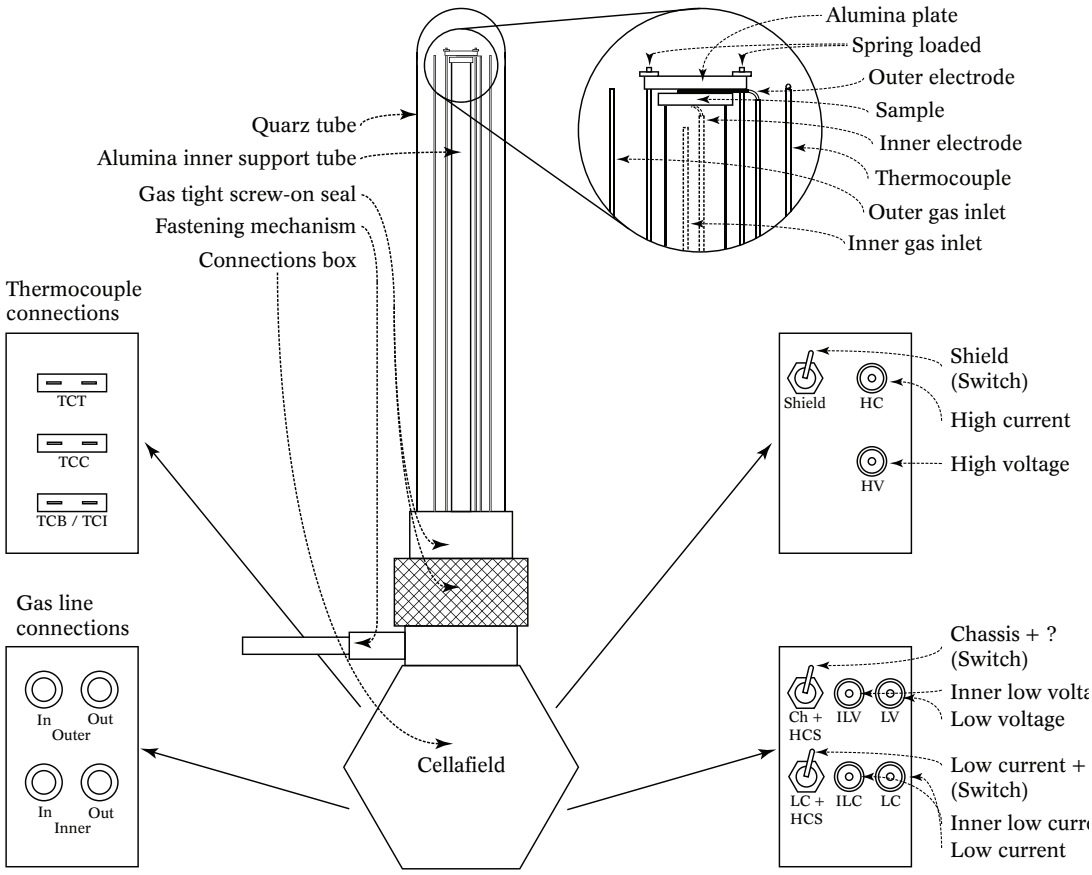

Figure 4.4 *– The inner workings of a NorECs Probostat™ sample holder. (The image is not to scale)*

4.3.2 Gas mixer

A gas mixer of the type sketched below, in Figure 4.5, was used to control the partial pressures of gases passed over the samples. The design of the gas mixer is such that three different gases can be used simultaneously, mixed and either dried, used “as-is”, wetted or a combination of these.

The drying stages contain P_2O_5 and gives gases passing through a pH_2O of roughly $3 \cdot 10^{-5}$ atm. In the wetting stages gases pass over a water surface before being bubbled through a saturated solution of KBr. This gives the gases a pH_2O of 0,025 atm at 25°C. This is roughly 80% of the pH_2O right after passing over the water surface. By lowering the pH_2O to less than 100% relative humidity, one avoids possible condensation

problems in colder parts of the mixer and measurement systems. The main flowmeters, 12 in numbers, are used in pairs to produce gas mixtures. Each pair of flowmeters is connected to their own bubbler column containing dibuthylftalat (DBF). These columns come in different sizes and are used to make sure the pressure through the system decreases towards the measuring cells. The final 4 flowmeters control how much gas is being fed to measurement cells.

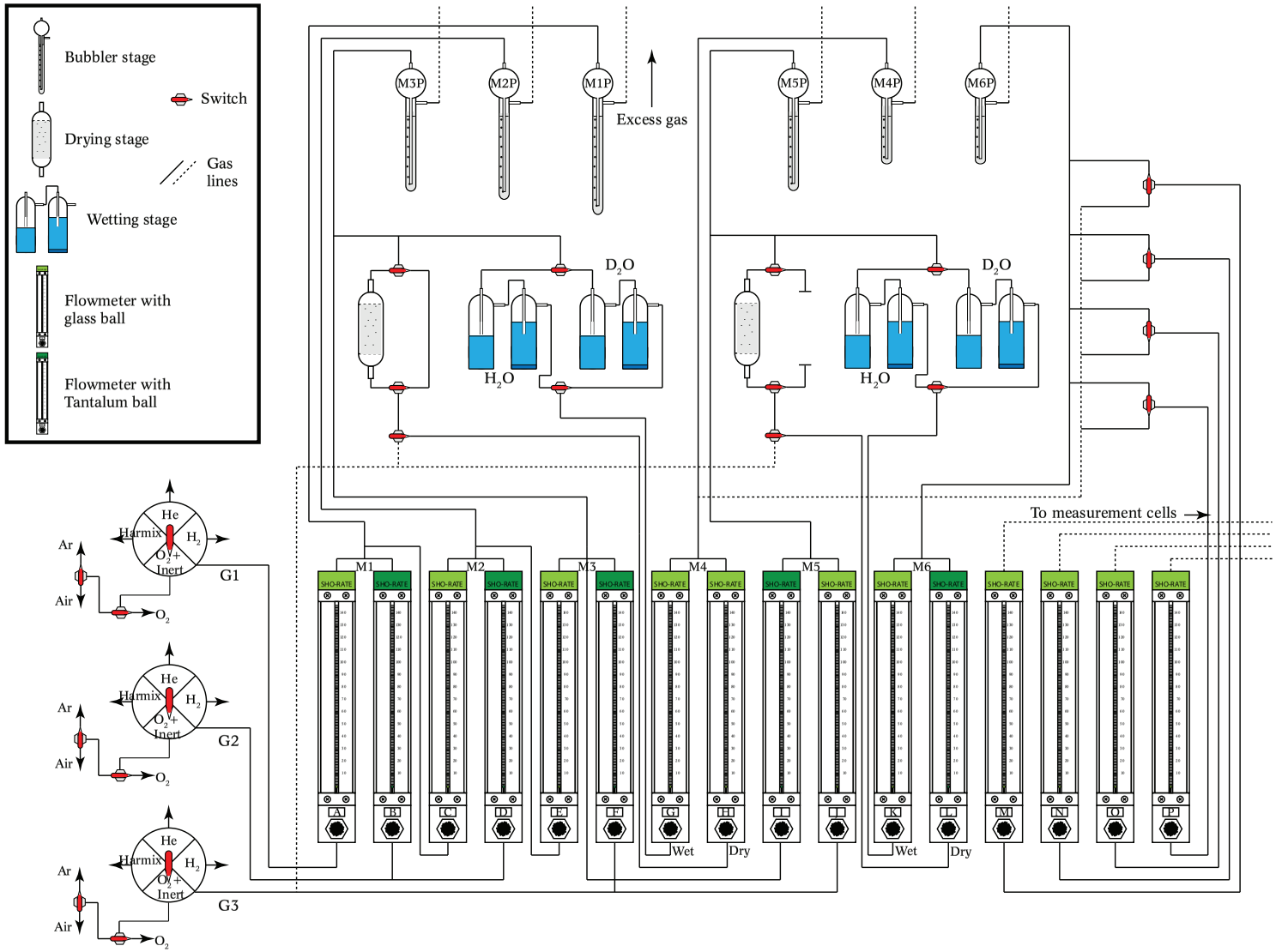

Figure 4.5 *– A sketch of the complex gas mixer used in this thesis. Flowmeters A-H and M-N were used. (The image is not to scale)*

4.3.3 Conductivity measurements

The conductivity measurements were carried out using a Solartron SI 1260 Impedance / Gain-Phase Analyzer. This specific instrument can measure in a frequency span from 10 μHz to 32 MHz and has an input impedance of 1MΩ. When frequencies below 10 MHz are used, maximum amplitude of 3 V is possible. Measurements in this thesis were carried out using voltage amplitudes of 0.5 V.

4.4 Sources of error

In a project, such as this one, several sources of error can be tracked down. Errors during synthesis, physical characterization and electrical characterization are conceivable.

4.4.1 Errors during sample preparation

Typical systematic errors during synthesis may be bad calculations before weighing powders, wrong methods for using weighting scales and wrong use of the furnaces and ball mill. Another systematic error coming from the ball mill is Si-impurities. During each second of ball milling, an increased amount of silicon will be introduced to powders being milled. This error is hard to eliminate. Random errors during synthesis may comprise of wrongly reading weights of a powder, mixing up of samples, the use of unclean equipment and taking the wrong notes.

4.4.2 Errors during physical characterization

When preparing powders for powder XRD using a glass plate sample holder, it is important to have a thin, uniform layer of powder on top of the glass plate. It is a common mistake to spread a thick layer of powder on top of the plate instead. This gives a worse XRD image than needed, with broader peaks than necessary. When doing XRD on a pellet, it is important to properly polish and clean the pellet before doing any XRD. This avoids doing XRD of any surface impurities and surface irregularities.

It is important to have a proper understanding of the SEM equipment before doing any SEM scans. The possible errors one can make are numerous.

4.4.3 Errors during electrochemical characterization

During electrochemical characterization, possible errors are mostly linked to wrong usage of equipment and poor mounting of samples inside the measuring equipment. Wrong data on sample thickness and electrode diameter might also be a source of error. Other sources of errors may include old and worn flowmeters, ignoring the effects of slow kinetics in samples at low temperatures, leakages through gas lines and failing to take sample porosity into consideration.

Gas line leakage is supposed to be taken care of in the measurement software. The uncertainties of flow through the flowmeters are up to ~60% when only low flows are used (below 20 mm). When the flow is higher and preferably above 60mm, uncertainty reduces to ~5%. [42]. The hydrogen and argon gases used in this thesis had purities of 99.999 volume %, while the oxygen gas used only had a purity of 99.5 volume %.

5 Results

Table 5.1 lists samples prepared in this thesis, but also what kinds of characterizations and measurements were performed on each sample. A cross under "XRD" or "SEM" means that the given sample was characterized using XRD or SEM, respectively. A cross under "Impedance" means that impedance sweeps were performed on the sample. Crosses under "pH_2O" or "pO_2" means that the sample underwent pH_2O-dependency or pO_2-dependency measurements, respectively. A cross under "O_2 ramps" means that temperature ramps in both wet and dry oxygen atmospheres were created for the sample. Finally, a cross under H_2 ramp means that a temperature ramp in wet hydrogen was created for the selected sample.

Table 5.1 *– Sample compositions and measurements done to them.*

Sample no.	XRD	SEM	Impedance	pH_2O	pO_2	O_2 ramps	H_2 ramp
38	X					X	
40	X		X	X	X	X	X
42	X					X	X
44	X			X	X		
46	X						
48	X			X	X	X	X

This chapter is divided into three sections. The first section deals with results relating to XRD. The second section discusses SEM results, while the third and final section gives a review on conductivity measurements.

5.1 XRD

XRD data was retrieved for all samples, as a quality control, before any other measuring took place. XRD made it possible to easily see whether samples contained phase pure $LaNbO_4$, or whether the elusive single phase-boundary/dual phase boundary in the $LaNbO_4$-$LaTaO_4$-system had been crossed. This will be discussed in section 5.1.2.

Additionally, XRD was used to observe gradual changes in phase composition after one, two and three calcinations of sample 40.

5.1.1 XRD after calcinations of sample 40

Sample 40 was the first sample to be prepared and therefore a prime candidate for XRD measurements in-between calcinations. Three selected phases and their evolution after one, two and three calcinations will be shown. These phases were chosen to give a general idea on how calcination may alter total phase compositions before sintering.

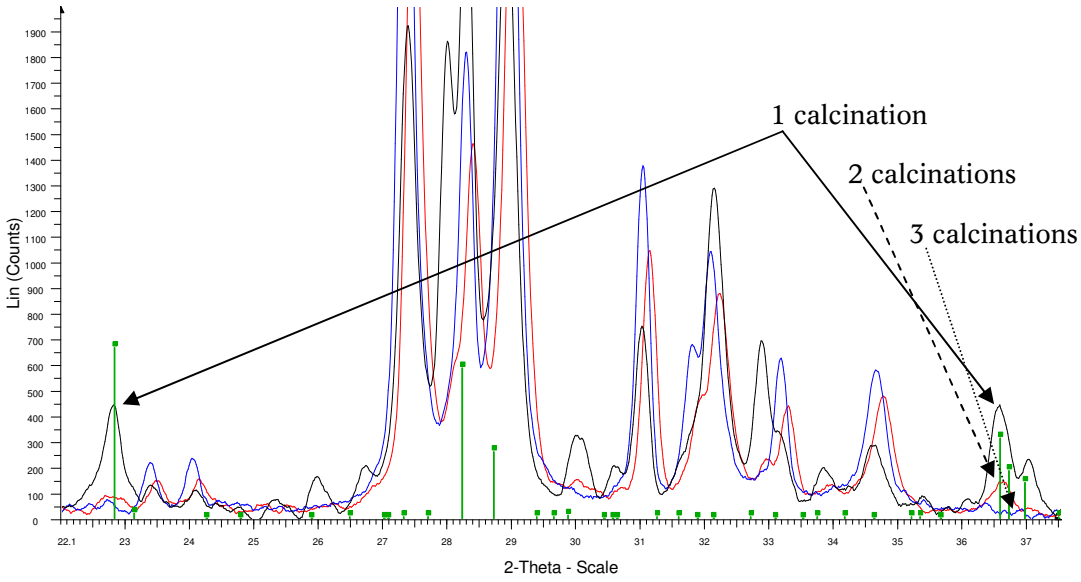

Figure 5.1 *– Changes in Ta_2O_5-content (vertical bars) in sample 40 after 1-(black), 2-(red) and 3-(blue) calcinations.*

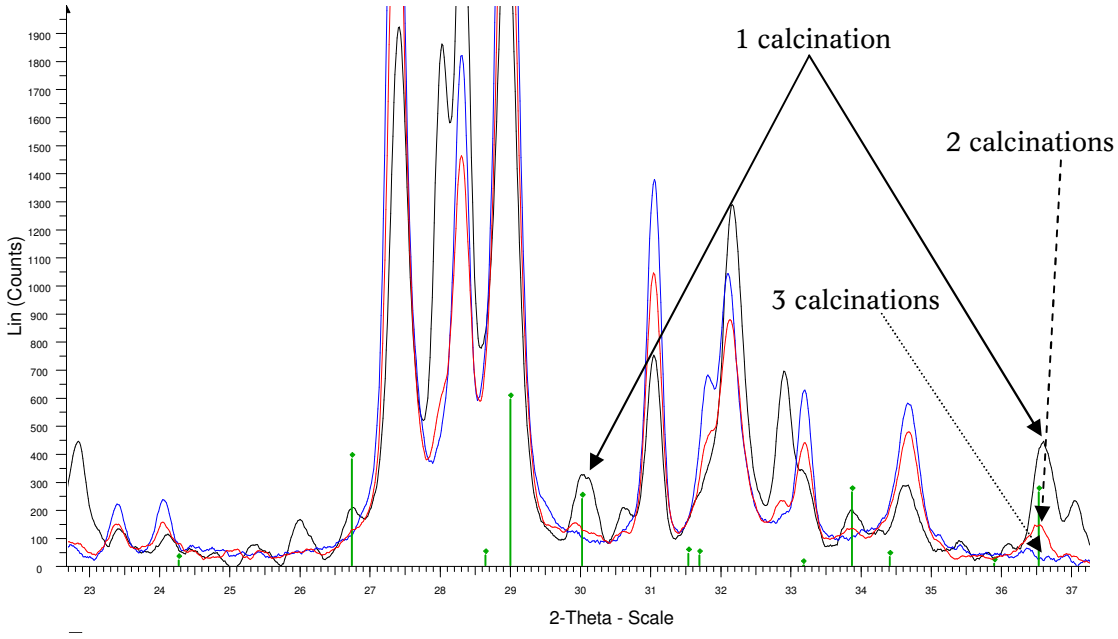

Figure 5.2 *– Changes in $LaTa_7O_{19}$-content (vertical bars) in sample 40 after 1-(black), 2-(red) and 3-(blue) calcinations.*

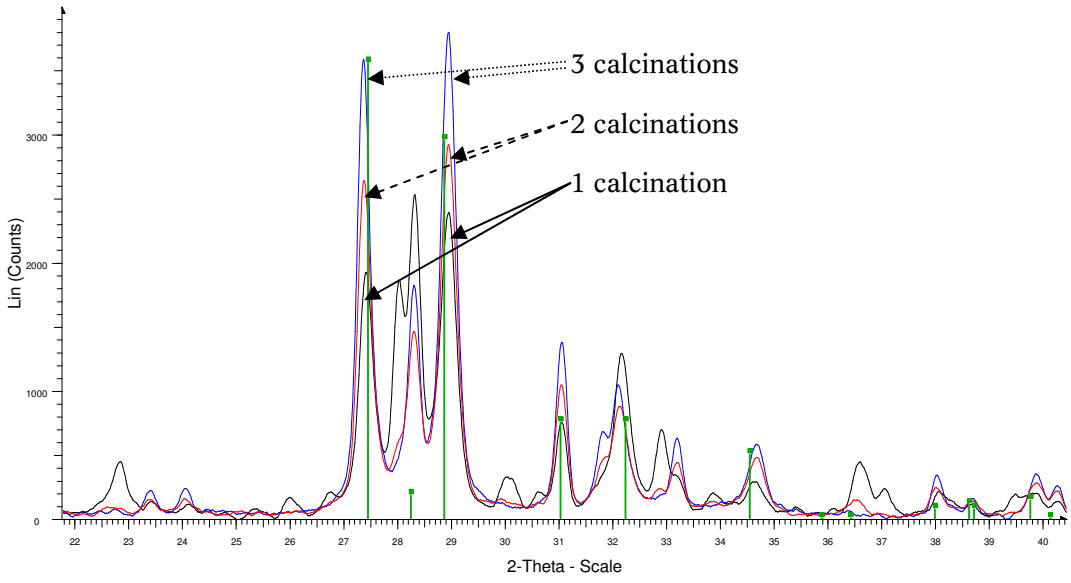

Figure 5.3 *– Changes in $LaNbO_4$-content (vertical bars) in sample 40 after 1-(black), 2-(red) and 3-(blue) calcinations.*

Figure 5.1 through Figure 5.3 show the importance of calcination in solid state synthesis. The phase composition after three calcinations is remarkably different from the phase composition after just a single calcination.

5.1.2 XRD on samples before conductivity measurements

As already stated, XRD was used to quickly observe whether samples contained phase pure material before any other measurements were carried through. Samples 38-46 had almost identical XRD spectra, showing a Ta-rich, phase-pure $LaNbO_4$-phase. Several peaks were shifted somewhat compared to pure $LaNbO_4$, but were still recognizable. The shift in peaks is understandable as the cell parameters of $LaNbO_4$ are shifted quite a bit when large quantities of $LaTaO_4$ are added. (Ref. section 3.1.3 and Figure 3.3)

The XRD spectrum of sample 46 is plotted in Figure 5.4 to show what the identical XRD spectra of samples 38-46 look like. Green columns represent literature XRD spectra of $LaNbO_4$. Several similarities can be seen when comparing this to the theoretical XRD spectrum of monoclinic $LaNbO_4$ (Figure 3.3).

While the XRD spectra of samples 38-46 were rather straightforward to interpret, sample 48 had a few different peaks extra. After careful elimination of possible phases, two main phases remained. These two phases, $La_{0.33}TaO_3$ (tetragonal)[43] and $La(Ta_3O_9)$ (orthorhombic)[44], explains all new significant peaks, but not the weakest peaks.

Some very weak peaks in the XRD of sample 48, hardly distinguishable from background noise, were observed and eventually decided to be reflections from $LaTaO_4$. Finally the elusive single-phase / dual-phase phase boundary seemed to have been discovered at around 48% Ta-doping of $LaNbO_4$.

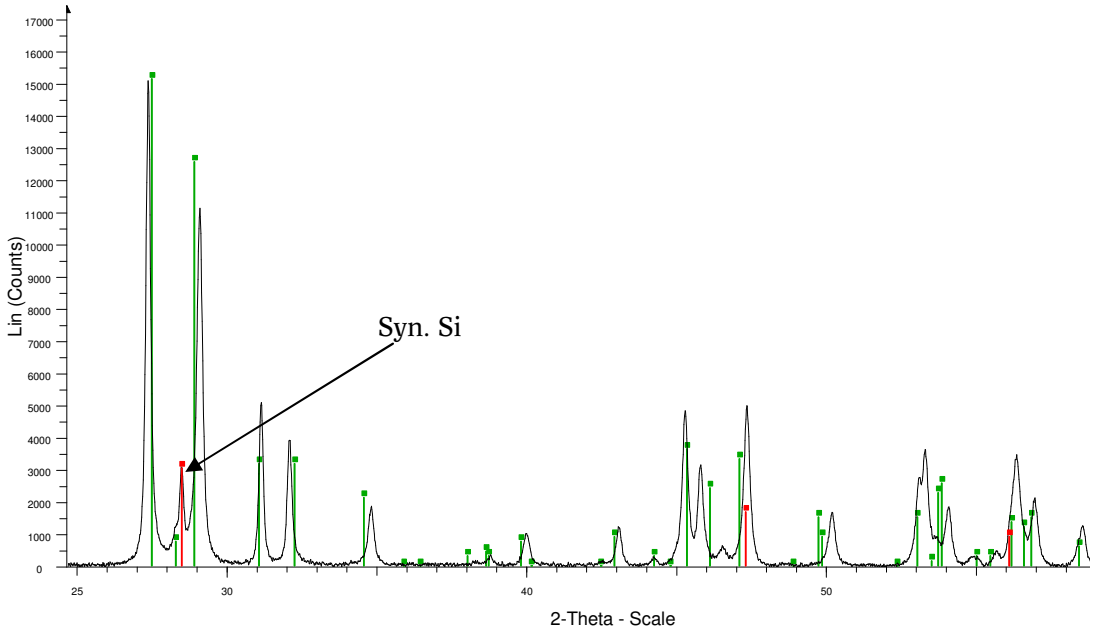

Figure 5.4 *– The XRD of Sample 46 showing phase-pure $LaNbO_4$.*

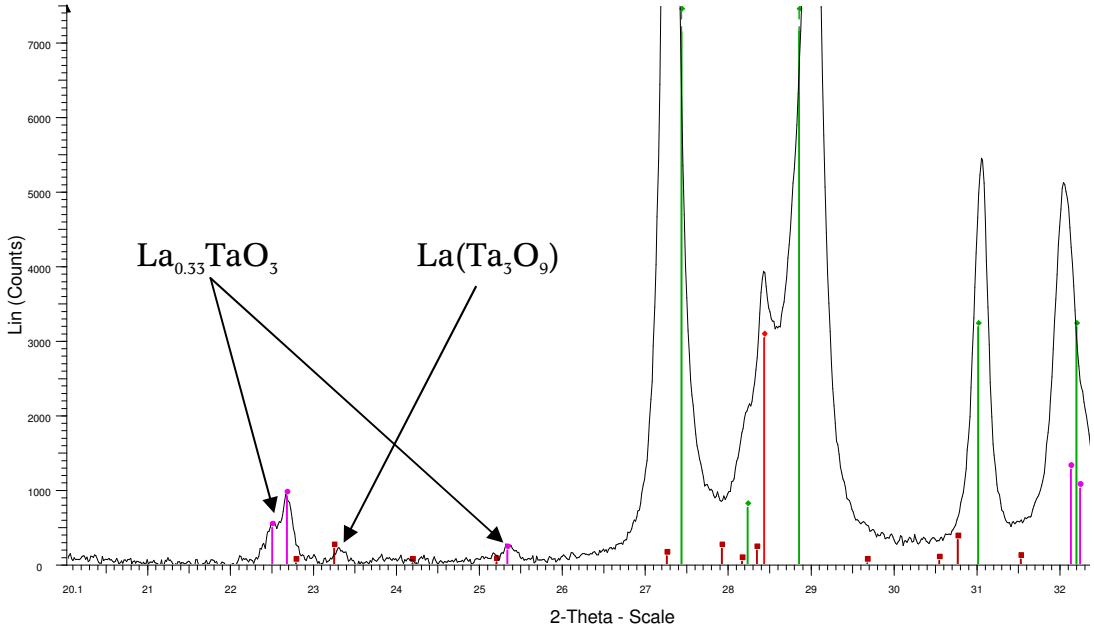

Figure 5.5 *– A part of the XRD of Sample 48 showing peaks not seen in earlier samples.*

5.2 SEM

The SEM-pictures were similar for all samples. Grains were uniform and of the same size. Looking at the SEM-pictures and EDS results, no definite signs of the secondary phases, seen in later parts of section 5.1.2, were to be found. This could be due to very high Ta-doping of the $LaNbO_4$-phase, possibly in combination with high concentrations of Nb in Ta-phases. The net result would be all phases having roughly the same concentrations of Nb and Ta.

A second reason for not observing the secondary phases could be due to their low concentration compared to the large amount of primary $LaNbO_4$-phase. EDS would possibly not be able to detect such small amounts of secondary phases.

Figure 5.6 a)-d) displays SEM pictures, originating from samples 40, 44 and 48. They were made using by a combination of back scattered electrons (BSE) and secondary electrons (SE). As can be seen, very few differences between samples exist.

Grain sizes appear to be between 1µm and 4µm in diameter with an average size close to 2.5µm. This is roughly half the grain size of pure Ca-doped $LaNbO_4$. (See section 3.1.1) It seems that, in general, higher doping leads to smaller grain sizes due the lower mobility of doped systems.

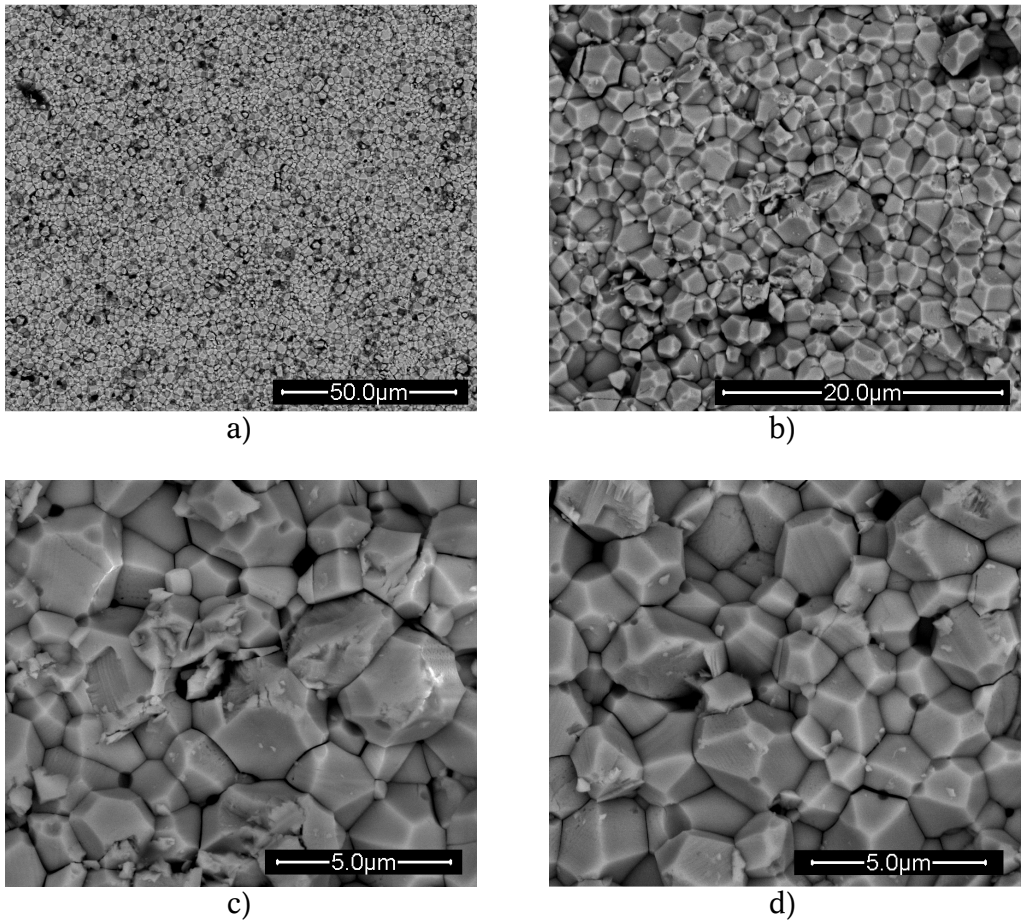

Figure 5.6 *– SEM pictures of sample 40 (a), 44 (b and c) and 48 (d)*

5.3 Conductivity

AC voltages of 10 kHz were used to create measurements displayed in the literature section of this thesis (section 413.2). This was the reason for choosing 10 kHz as the AC voltage frequency to be used when doing pH_2O- and pO_2-dependency conductivity measurements in this thesis.

This chapter will display conductivity measurements from most of the samples synthesized for this thesis and also point out some of the features observed in aforementioned measurements. First, impedance sweeps of sample 40 will be shown. pH_2O dependency and pO_2 dependency measurements of samples 40, 44 and 48 follow shortly thereafter. Towards the end of the chapter, temperature ramps in wet

and dry oxygen are shown for samples 38, 40, 42 and 48. Finally, temperature ramps in wet H_2 for samples 40, 42 and 48 are displayed.

5.3.1 Impedance sweeps

In order to maintain acceptable control over whether grain boundary impedance, bulk impedance or electrode impedance contributes to measured impedance, impedance sweeps were generated. (See section 2.2.5.) As frequencies gradually were reduced from 100 kHz to 0.1Hz, sweeps were generated. The sweeps were created at temperatures between 300°C and 750°C, using 50°C intervals under reducing, wet conditions.

Successful interpretations of results were possible at 300°C-500°C. At higher temperatures, conductivity was too high and the semicircles shifted too far up in frequency. The full set of impedance spectra of sample 40, can be seen in Figure 5.7 a) to j). In these figures the y-axis corresponds to negative reactance, -X, while the x-axis corresponds to resistance, R. The numeric values of the axes will be shown together with modeled impedance sweeps in a later chapter. (section 6.2)

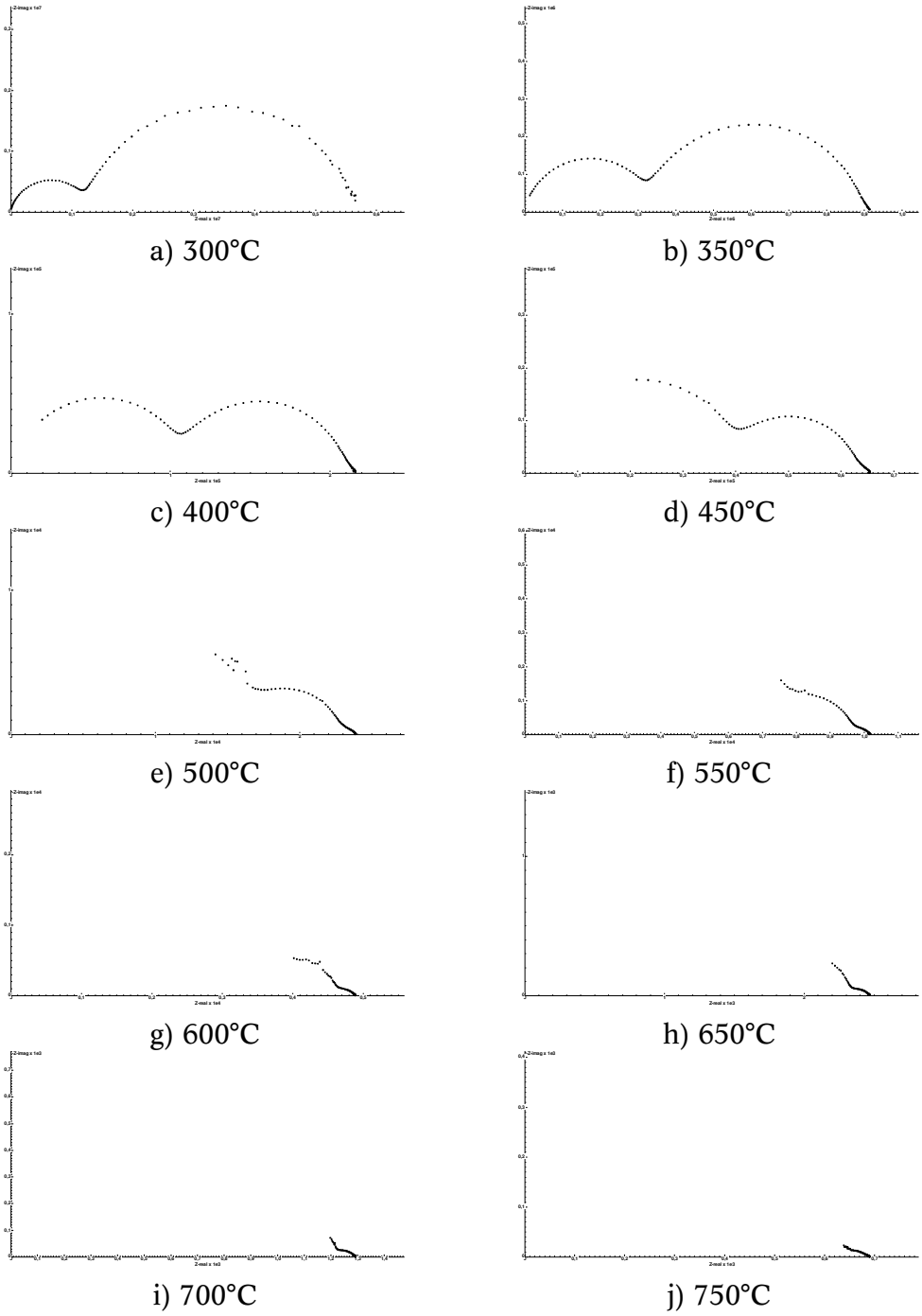

a) 300°C b) 350°C

c) 400°C d) 450°C

e) 500°C f) 550°C

g) 600°C h) 650°C

i) 700°C j) 750°C

Figure 5.7 *– Impedance sweeps of sample 40, $La_{0.99}Ca_{0.01}Nb_{0.60}Ta_{0.40}O_4$, scanned from 100 kHz to 0.1 Hz. The sweeps were generated under reducing, wet conditions.* T*he x-axis corresponds to negative reactance, -X, while the y-axis corresponds to resistance, R.*

5.3.2 pH_2O dependency

Figure 5.8 a)-c) display the total conductivities of samples 40, 44 and 48, respectively, as a function of water vapor partial pressure. The measurements were carried through at temperatures of 800°C, 1000°C and 1200°C under reducing conditions. Oxygen pressure is kept more or less constant at each temperature, due to a constant pH_2O/pH_2 ratio. For this section, measurements were carried out using the following temperature increase: Room temperature, 800°C, 1000°C and finally 1200°C.

Measurements generated for sample 40 (Figure 5.8 a) seem to follow an expected pattern; at low temperatures the curve is steeper than at higher temperatures yet they all seem to have the same general shape. The curves are more or less evenly spaced and slightly curved away from being perfectly straight.

The same cannot be stated for sample 44, $La_{0.99}Ca_{0.01}Nb_{0.56}Ta_{0.44}O_4$ (Figure 5.8 b) and sample 48, $La_{0.99}Ca_{0.01}Nb_{0.52}Ta_{0.48}O_4$ (Figure 5.8 c). The two samples show deviations from the pattern seen for sample 40 at 800°C. While sample 40 displays a steeper curve at 800°C than at 1000°C, Sample 44 and 48 display gentler curves at 800°C than at 1000°C. In all other respects the curves show similar properties.

A final observation to take note of is that generally the total conductivity increases as more $LaTaO_4$ is added. This is true for all samples at 1000°C/1200°C and is opposite of what is being observed for samples 44 and 48 at 800°C. Here, total conductivity decreases as more $LaTaO_4$ is added.

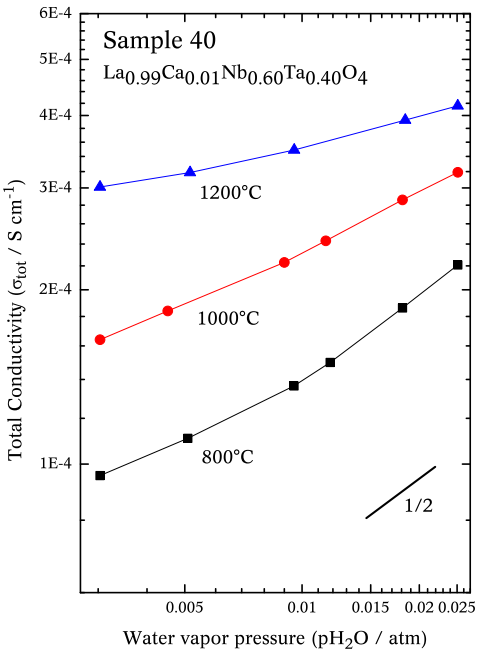

***Figure 5.8** a)*

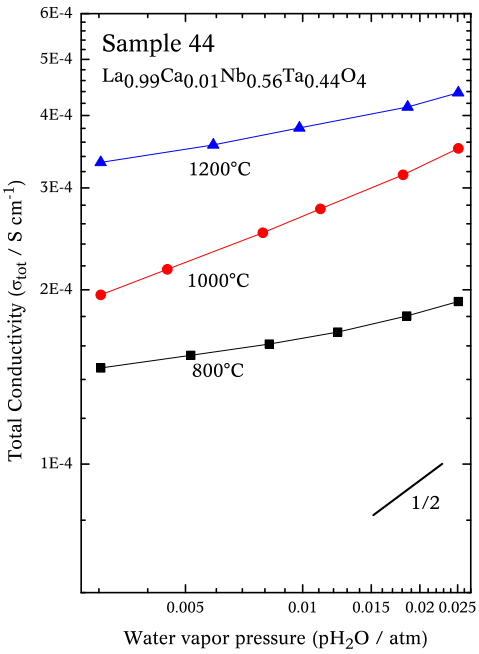

***Figure 5.8** b)*

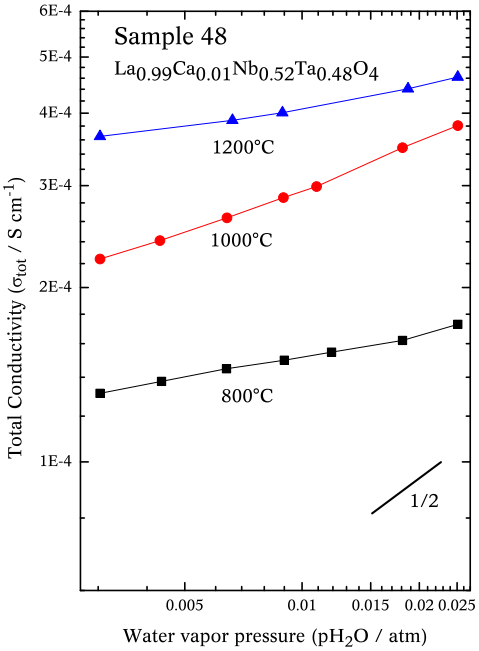

***Figure 5.8** c)*

***Figure 5.8** – The total conductivities of sample 40 (a), 44 (b) and 48 (c) as functions of water vapor partial pressures under reducing conditions.*

5.3.3 pO_2 dependency

Figure 5.9 a)-c) display the total conductivities of samples 40, 44 and 48, respectively, as a function of oxygen partial pressure. The measurements were carried through at temperatures of 800°C, 1000°C and 1200°C using wetted gases (pH_2O of ~0.025 atm). In contrast to the pH_2O-measurements, pO_2 measurements at 800°C were done after decreasing the temperature from 1200°C through 1000°C. This could, in turn, mean that measurements were only done on the high-temperature tetragonal phase in all samples.

No surprising or deviating results were seen in any of the pO_2 measurements. At 800°C all samples show an almost flat line connecting the individual measurements. The line is increasingly curving upwards at the right hand side as temperature increases. At the highest temperatures the curve reaches a slope of $(pO_2)^{1/4}$. On the left hand side, the line stays flatter at all temperatures, but still does have a more pronounced curve at higher temperatures.

It can be seen that the total conductivities of all samples steadily increase with increasing Ta-content at the three temperatures used.

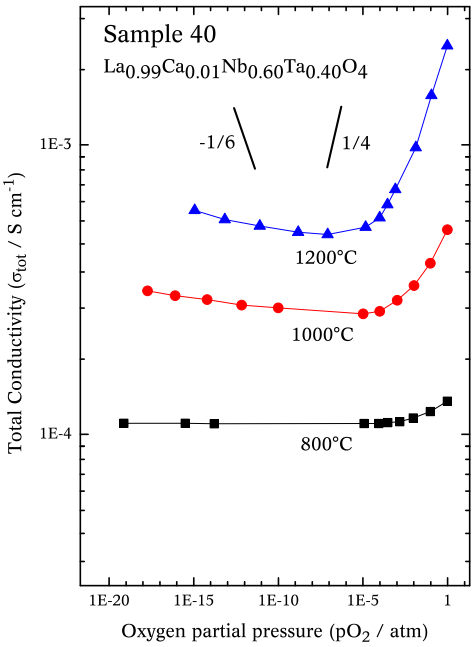

***Figure 5.9** a)*

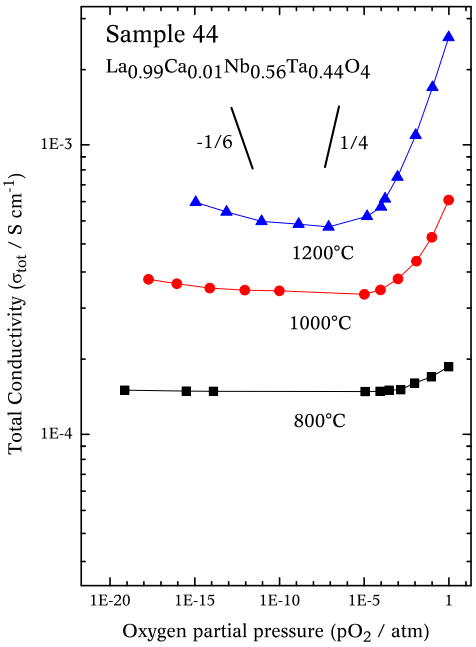

***Figure 5.9** b)*

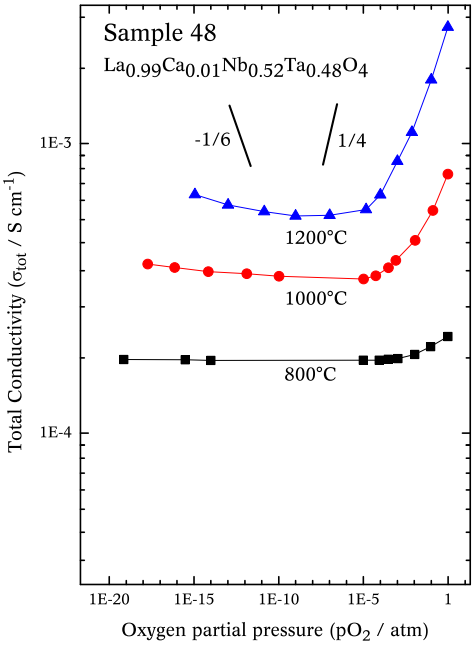

***Figure 5.9** c)*

***Figure 5.9** – The total conductivities of sample 40 (a), 44 (b) and 48 (c) as functions of oxygen partial pressures using wetted gases.*

5.3.4 Temperature ramps

Figure 5.10 a)-d) display total conductivities of samples 38, 40, 42 and 48 respectively as a function of inverse temperature, using different mixes of gases. All four samples were measured in wet and dry O_2, while all, except sample 38 also were measured in wet H_2. A temperature rate of change of -6°C/h was used to make the ramps, decreasing from 1100°C to 400°C.

In all samples there is a significant difference in conductivity between wet and dry oxygen atmospheres. The measurements also show that the total conductivity of wet oxygen has a pronounced change in temperature dependency at temperatures around 800°C-850°C. This change in temperature dependency will henceforth be called "the breaking point" or "T_{break}".

Temperature ramps in wet hydrogen were created for samples 40, 42 and 48. Wet hydrogen seems to have an even higher total conductivity than wet oxygen, but only up to a certain temperature. At this temperature the temperature dependency of wet hydrogen goes through an abrupt change, much like that for wet oxygen. The temperature dependency change for wet hydrogen is significantly more abrupt than for oxygen, but seems to happen at the same temperature.

At higher temperatures, the total conductivity in wet H_2 increases much slower than the total conductivity for both wet and dry O_2. At temperatures higher than T_{break}, wet H_2 eventually ends up with having a lower total conductivity than both wet and dry O_2.

It can be seen that the total conductivity of all samples increases with increasing Ta-content at temperatures above T_{break}. This is true for the three atmospheres used in this experiment. At temperatures below T_{break}, the total conductivity decreases with increasing Ta-content in wet H_2, while seems to stay roughly the same in wet and dry O_2.

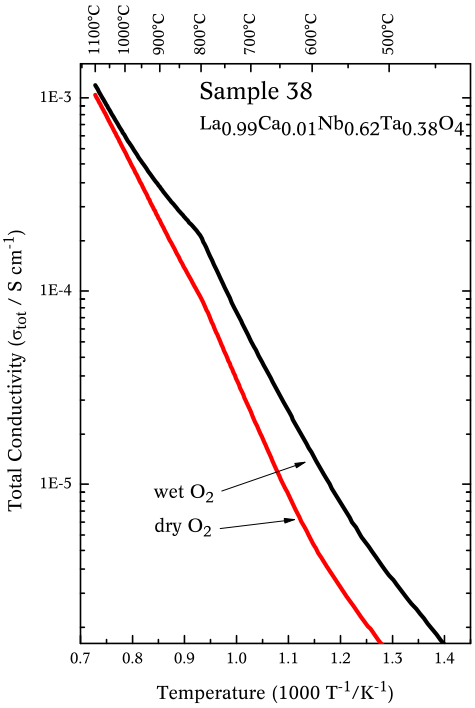

***Figure 5.10** a)*

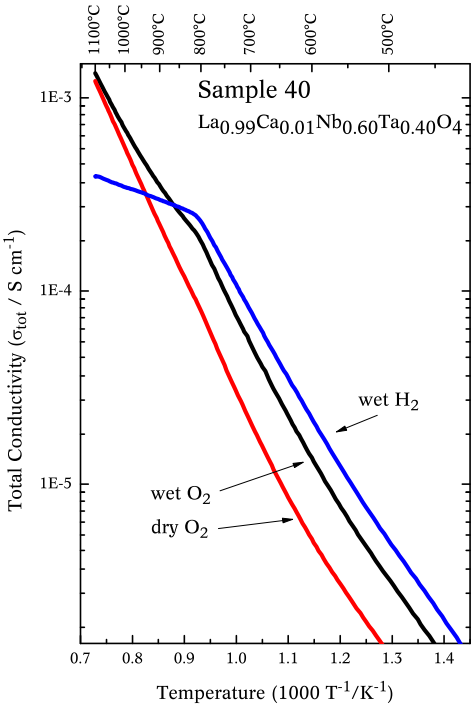

***Figure 5.10** b)*

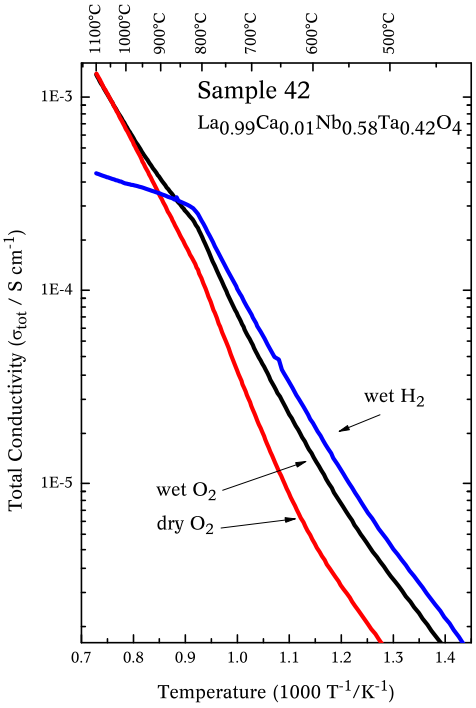

***Figure 5.10** c)*

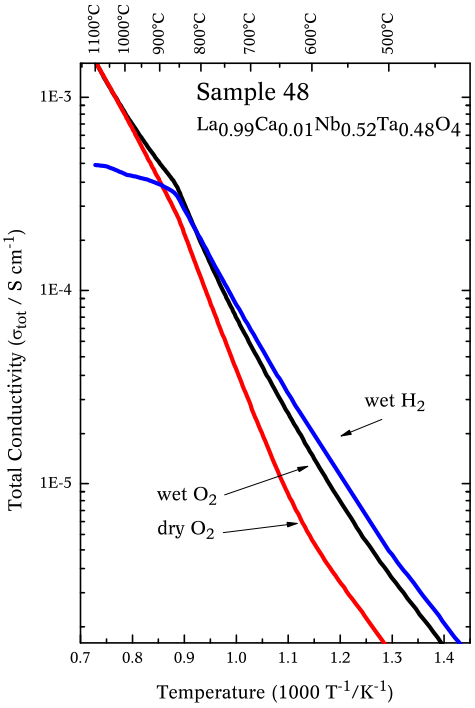

***Figure 5.10** d)*

***Figure 5.10 (previous page)** –The total conductivity for Sample 38 (a), 40*

(b), 42 (c) and 48 (d) as functions of inverse temperature in atmospheres containing wet O_2, dry O_2 and wet H_2.

6 Discussion

In previous chapter it was interesting to observe that "The breaking point" seemed to increase in line with increased tantalum content, as did the total conductivity above T_{break}. Below T_{break}, trends were not as clear. The erratic conductivity behavior of sample 44 and 48 at 800°C in Figure 5.8 b)-c) needs explanation as do other conductivity trends.

$LaNbO_4$ is the main parent phase for the samples in this thesis. All samples contained $LaNbO_4$-phase "doped" with different amounts of Tantalum. By comparing conductivities of Ta-doped $LaNbO_4$-samples to pure $LaNbO_4$-samples from literature, one should be able to see whether high amounts of Ta-doping gives any advantages over pure Ca-doped $LaNbO_4$. Also, it is of interest to see whether the addition of secondary, Ta-rich phase changes anything related to conductivity.

Of all the samples, sample 40 was chosen to be thoroughly compared to its parent phases, because it was the only measured sample with a phase transition temperature at, or below, 800°C. This made it certain that all measurements were carried through on high-temperature phases of $LaNbO_4$ and $LaTaO_4$.

By comparing Brouwer diagrams for pH_2O and pO_2 dependency from section 2.1.8, the total electroneutrality given in equation (2.17) and the partial pressure dependencies, seen in section 5.3, defect situation in all samples will be explained. Additionally, shapes of measured temperature ramps will be discussed.

The first parts of this chapter contain a quick review on the phase transition temperature of $LaNbO_4$ in addition to interpretations of impedance sweeps. Sections discussing pH_2O dependency, pO_2 dependency and temperature ramps follow thereafter. In the end of this chapter there is section dealing with possible future work on the $LaNbO_4$-$LaTaO_4$-system.

6.1 Phase transition temperatures compared

Vullum et al. [19] showed that the phase transition temperature of $LaNbO_4$ increases with increasing content of tantalum up to a maximum of ~800°C with $LaNb_{0.6}Ta_{0.4}O_4$ (Figure 3.12). Comparing this phase transition temperature to T_{break}, seen in previous chapter, one can draw the conclusion that the observed "breaking point" in the temperature ramps actually is a sign of mentioned phase transition.

In the same study by Vullum et al. [19], it was shown that the phase boundary dividing the single phase area, containing only $LaNbO_4$-phase, from the dual phase area, having both $LaNbO_4$ and $LaTaO_4$-phases, exists somewhere between $LaNb_{0.60}Ta_{0.40}O_4$ and $LaNb_{0.50}Ta_{0.50}O_4$ in the phase diagram.

By defining $T_{break} = T_{phase\ tr.}$, one can compare the phase transition temperature for samples in this thesis to their literature values. Table 6.1 lists values from this thesis as well as literature values. It can be seen that values from this thesis are similar to values published in literature.

Table 6.1 *– Comparison of phase transition temperatures to Ta-content in samples of different compositions of $LaTaO_4$ and $LaNbO_4$.*

Sample	Ta-content	Temperature
$LaNbO_4$	0%	510±10°C [19]
$LaNb_{0.80}Ta_{0.20}O_4$	20%	670±10°C [19]
$LaNb_{0.62}Ta_{0.38}O_4$	38%	795±5°C
$LaNb_{0.60}Ta_{0.40}O_4$	40%	800±10°C [19]
$LaNb_{0.60}Ta_{0.40}O_4$	40%	800±5°C
$LaNb_{0.58}Ta_{0.42}O_4$	42%	815±5°C
$LaNb_{0.52}Ta_{0.48}O_4$	48%	850±5°C

One can assume that the phase transition temperature increases steadily as more Ta is added, up to a maximum at the single-phase/dual-phase phase boundary. By this assumption, Table 6.1 shows that the actual phase boundary between single- and dual-phase areas, in $LaNbO_4$, exists much closer to the composition of $LaNb_{0.50}Ta_{0.50}O_4$ than to $LaNb_{0.60}Ta_{0.40}O_4$.

A least square linear fit of Ta-content as a function of temperature values from Table 6.1, gives the following equation:

$$T = 710x + 517 \qquad (6.1)$$

In this case, T is the phase transition temperature and x is the percentage of Ta-content written as a decimal number. The equation seems to fit for most of the observed values. (Figure 6.1)

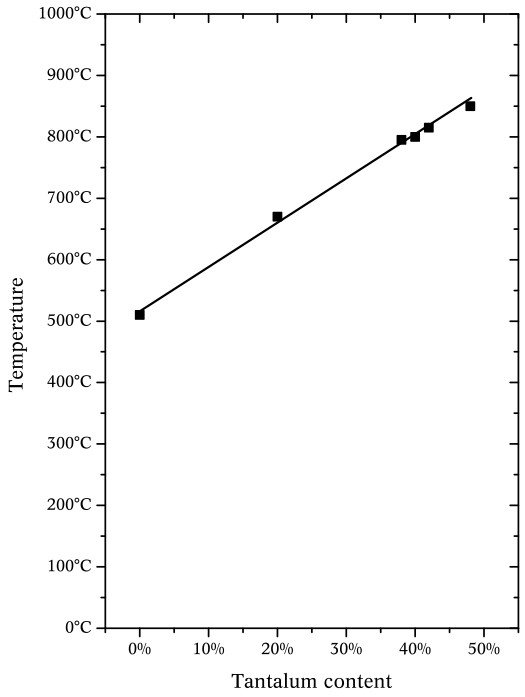

Figure 6.1 *–The temperature of phase transition as a function of tantalum content in the* $LaNb_{1-x}Ta_xO_4$*-system. The line represents equation* (6.1)

6.2 Interpretation of impedance sweeps

Comparing section 2.2.3 and 2.2.4 to the actual impedance sweeps in section 5.3.1, several interesting characteristics may be noted:

A slight impedance contribution from the electrodes can be seen at very low frequencies (right, small "semicircle"). The semicircle corresponding to electrode impedance is seen to increase in size with temperature compared to the semicircle for grain boundaries (right, big semicircle).

As temperature increases, the semicircle corresponding to bulk impedance (left semicircle) increases in size when compared to the semicircle corresponding to grain boundary impedance. This might imply that the impedance of grain boundaries have a greater temperature dependency than bulk impedance.

Using the equivalent circuit in Figure 2.13 together with results obtained from fitting the impedance spectra in Equivalent Circuit [45], the following values for R, Y_0 and n were obtained (Table 6.2):

Table 6.2 *– Values extracted from the fitting of impedance sweeps in Equivalent Circuit.*[45]

	R_{bulk}	Q: Y_{0bulk}	Q: n_{bulk}	R_{gb}	Q: Y_{0gb}	Q: n_{gb}
300°C	1.17E6	1.43E-10	0.886	4.54E6	8.60E-9	0.825
350°C	3.23E5	1.63E-10	0.883	5.78E5	1.01E-8	0.856
400°C	1.07E5	1.50E-10	0.894	1.05E5	1.12E-8	0.876
450°C	3.99E4	1.21E-10	0.912	2.38E4	1.38E-8	0.874
500°C	1.63E4	7.73E-11	0.943	6.77E3	2.01E-8	0.844

After some calculation and comparison with the other temperatures, it can be seen that values, extracted from the fitting of 500°C in Equivalent Circuit, probably are not entirely correct. The numbers at this temperature diverge a bit from the steady evolution of numbers between the other temperatures.

Sweeps were interpreted using Equivalent Circuit for Windows 1.2 [45], remodeled using values from Equivalent Circuit inserted into Excel 2007 [46] and the values plotted using OriginPro [47]. The modeled impedance sweeps are more or less identical to their corresponding measured impedance sweeps, except for a small change: As already stated, a very small semicircle, corresponding to electrode impedance can be observed to the far right of the actual sweeps at very low

frequencies. (Figure 5.7) This semicircle was not added to modeled impedance spectra. (Figure 6.2)

In Figure 6.2, certain frequencies are displayed on the modeled impedance sweeps of sample 40, $La_{0.99}Ca_{0.01}Nb_{0.60}Ta_{0.40}O_4$, in order to show how frequencies move across the semicircles from left to right with increasing temperature.

At 300°C and a frequency of 10 kHz, pure bulk impedance is measured, as seen in Figure 6.2 a). This is seen to move towards grain boundary impedance as temperature increase (Figure 6.2 c). After a closer inspection of available RAW-data, it is seen that, at 10 kHz and temperatures above ~700°C, electrode impedance begin to play an important role (Far right in Figure 5.7 i)). It is importance to remember this electrode contribution when interpreting later constant frequency measurements.

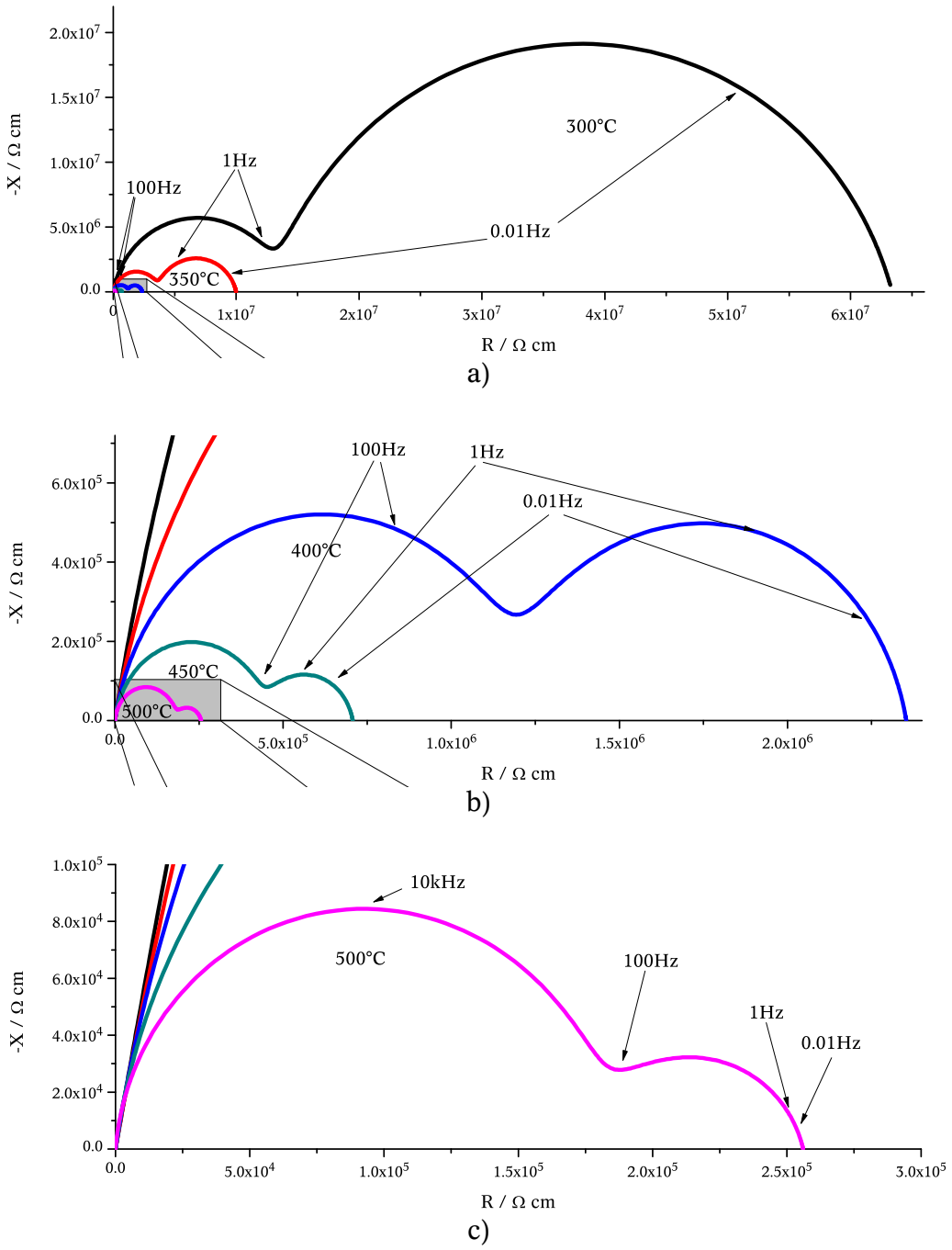

Figure 6.2 *– Modeled impedance sweeps of sample 40,* $La_{0.99}Ca_{0.01}Nb_{0.60}Ta_{0.40}O_4$.

6.3 pH_2O dependency

In section 5.3.2 it was seen that the three measured samples had somewhat different pH_2O dependencies at 800°C. When compared to the pH_2O dependency measurements for pure $LaNbO_4$, Sample 40 had the expected curve, while sample 44 and 48 had flatter curves than expected.

This discrepancy might be explained by the increasing phase transition temperature of $LaNbO_4$. The phase transition temperature increases to a maximum of ~850°C (Table 6.1) with increasing content of Ta. Table 6.1 shows that both sample 44 and sample 48 have their phase transition temperatures above 800°C, while sample 40 has its phase transition temperature at ~800°C. It is plausible that any two phases on each side of a phase transition temperature may have different pH_2O dependencies and that this is the reason for the observed differences.

When Figure 5.8 a) (pH_2O for sample 40) is compared to the Brouwer diagram in Figure 2.7, it can be seen that the slope, at 800°C and high water partial pressure, is getting very close to having a $(pH_2O)^{1/2}$ dependency slope. It is the same slope which ionic $OH_O^{\cdot}$ adapts at high water vapor pressures. This might indicate that at low temperatures and higher water vapor partial pressures the samples display increased proton concentration and thus proton conductivity. Since the conductivities follow $(pH_2O)^{1/2}$ dependencies at the highest water partial pressures and do not get flatter, one can conclude that samples are not fully protonated, even at very high water partial pressures. By this logic, protons remain minority defects in comparison to oxygen ions. Due to increased mobility of protons over oxygen ions, the proton conductivity still is higher than the oxygen ion conductivity.

At higher temperatures and lower water partial pressures, the curves are flatter and are more in line with oxygen vacancy ionic conductivity. This is also true for the low-temperature phase at 800°C.

The high-temperature phase in general increases its conductivity as more tantalum is added, while the low-temperature phase decreases in conductivity as tantalum is added. The reason for the increasing conductivity in the high-temperature phase could possibly be that when a certain amount of tantalum is mixed into tetragonal $LaNbO_4$, more Ca is incorporated into the structure instead of being trapped inside grain boundaries. This increased effective Ca-doping would in turn lead to more protons being incorporated in the structure and therefore higher conductivity.

The reason for having a lower conductivity as Ta is added to the low-temperature phase could possibly be due to a less ordered structure and therefore higher activation energy of proton conductivity.

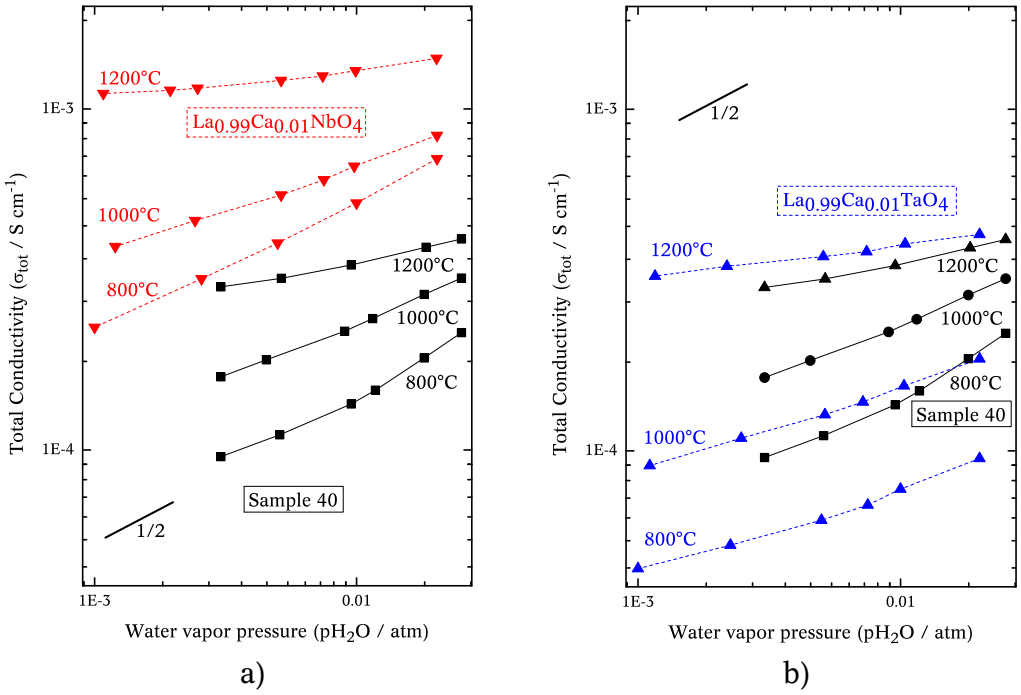

Figure 6.3 *– The total conductivities of sample 40, $La_{0.99}Ca_{0.01}Nb_{0.60}Ta_{0.40}O_4$, and $La_{0.99}Ca_{0.01}NbO_4$ (a) or $La_{0.99}Ca_{0.01}TaO_4$ (b) as a function of water vapor partial pressure under reducing conditions.*

Sample 40 seems to have the same kind of water vapor dependency as Ca-doped $LaNbO_4$, although with quite a bit lower total conductivity. (Figure 6.3) Both sample 40 and $LaNbO_4$ have the tell-tale $(pH_2O)^{1/2}$ dependency of $OH_O^{\cdot}$-conductivity at lower temperatures (Figure 2.7).

pH_2O slopes for Ca-doped $LaTaO_4$ are different. Here, the slopes are shallower than for both sample 40 and Ca-doped $LaNbO_4$. Except for very high temperatures, the total conductivities are somewhat lower than for sample 40. Adding up, it seems that sample 40 has much more in common with $LaNbO_4$ than with $LaTaO_4$.

6.4 pO_2 dependency

By comparing section 2.1.5 and 2.1.8 to section 5.3.3 one can assume that flat parts of the curves seen in the pO_2 dependency measurements, both in literature and this thesis, are signs of ionic conductivity. Thus, the electroneutrality condition for this case reads:

$$2[v_O^{\bullet\bullet}] + [OH_O^{\bullet}] = [Ca_{La}^{/}] \qquad (6.2)$$

At higher temperatures, curves in all samples, including $LaTaO_4$ and $LaNbO_4$, were seen to get steeper on the right hand side. This is often the case if p-type electronic conductivity becomes the major contributor to total conductivity under oxidizing conditions. Observing the curves getting very close to the tell-tale p-type slope of $(pO_2)^{1/4}$ at 1200°C, the evidences for p-type electronic conductivity at high temperature oxidizing conditions mount up.

On left hand side of the same figures it was seen that curves were curving slightly upwards at 800°C and noticeably more profound as temperature increased. The upward curving is often a sign of n-type electronic conductivity, especially if it reaches or gets close to a slope of $(pO_2)^{-1/6}$. In the case of these measurements, the curves remain reasonable flat. What this could mean is that under reducing conditions, and as temperatures increase, n-type electronic conductivity has an increasingly important contribution to total conductivity, but far from ever being the major contributor. Another explanation for the slight upward curving could be that the samples are reduced under reducing atmospheres and that the reduced samples have higher concentrations of protons, which in turn lead to higher proton conductivity. It could also be a case of decreased activation energy in the reduced samples compared to the "normal" samples.

Earlier it was assumed that all pO_2 measurements were done on the high-temperature tetragonal phase of all samples (5.3.3). It thus can be assumed that the trends with increased concentrations of Ta leading to increased conductivity follow the trends seen in previous section.

When sample 40 is compared to Ca-doped $LaNbO_4$ (Figure 6.4 a) it is seen that, while $LaNbO_4$ has very little or no upwards curving on the left hand side (ref. Figure 2.6), at any temperature, sample 40 has noticeable amounts.

When compared to Ca-doped $LaTaO_4$ (Figure 6.4 b), it is seen that the upwards curving on the left hand side in the pO_2 measurements of

sample 40 is significantly lower than those of $LaTaO_4$. Especially at higher temperatures, $LaTaO_4$ shows signs of n-type electronic conductivity

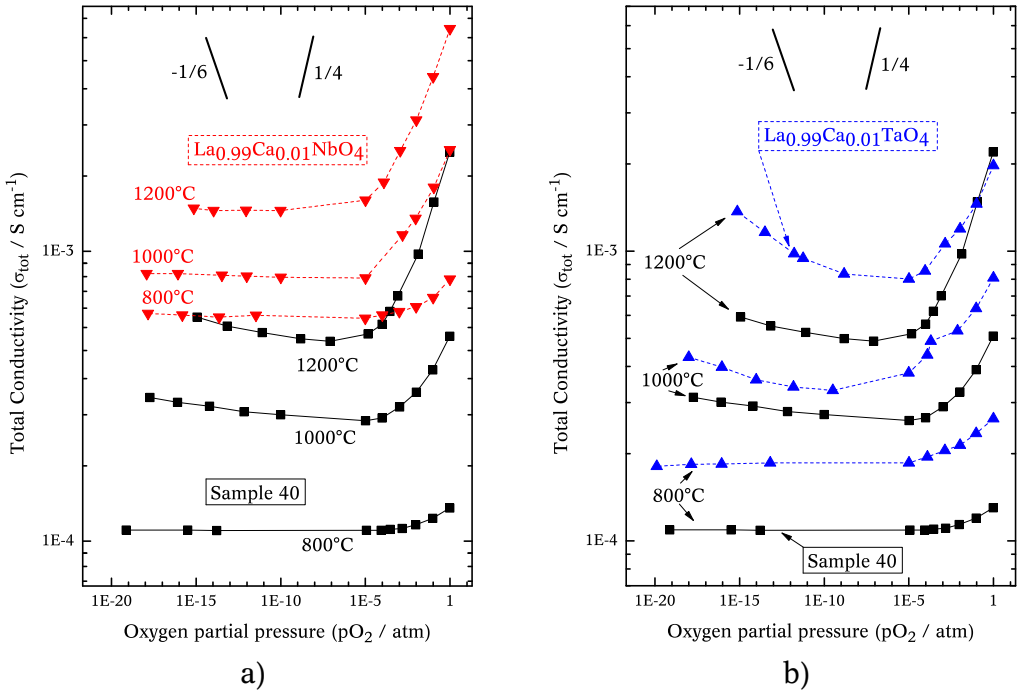

***Figure 6.4** – The total conductivity of sample 40, $La_{0.99}Ca_{0.01}Nb_{0.60}Ta_{0.40}O_4$, and $La_{0.99}Ca_{0.01}NbO_4$ (a) or $La_{0.99}Ca_{0.01}TaO_4$ (b) as a function of oxygen partial pressure.*

.

In the end, sample 40's oxygen partial pressure dependencies match those of $LaNbO_4$ in shape and form, but better match those of $LaTaO_4$ in magnitude of total conductivity. On average, total conductivity of sample 40 is half that of Ca-doped $LaTaO_4$.

6.5 Comparison in temperature ramps

As was seen in Figure 5.10 a)-d), the wet O_2-ramps had higher conductivities than the dry O_2–ramps at temperatures below ~1000°C. This is probably a sign of proton conductivity, since the only difference

between the two cases is increased hydrogen content in the case of wet O_2.

At temperatures above ~1000°C, wet and dry O_2 gradually end up having identical total conductivities. The probable reason for this is a deprotonation of samples at high temperatures. At these temperatures, oxygen ion and electronic conductivities gradually take over and finally end up being the major contributors to total conductivity at ~1100°C.

The swift change between different slopes and gradients across the $LaNbO_4$-phase boundary in wet H_2 (Figure 5.10 b)-d)) can be attributed to different values of proton transport activation energies. A steeper slope often means higher activation energies.

The reason for wet H_2 having a total conductivity below those of wet and dry oxygen at higher temperatures is possibly due to an almost 100% proton conductivity under reducing conditions compared to more p-type conductivity under oxidizing conditions (Values are seen in Table 6.3). This is backed up by the pO_2 dependency measurements.

At lower temperatures it was seen that wet hydrogen in general had a higher conductivity than wet oxygen. This is probably, as stated in section 6.4, a sign of the samples being reduced under reducing atmospheres.

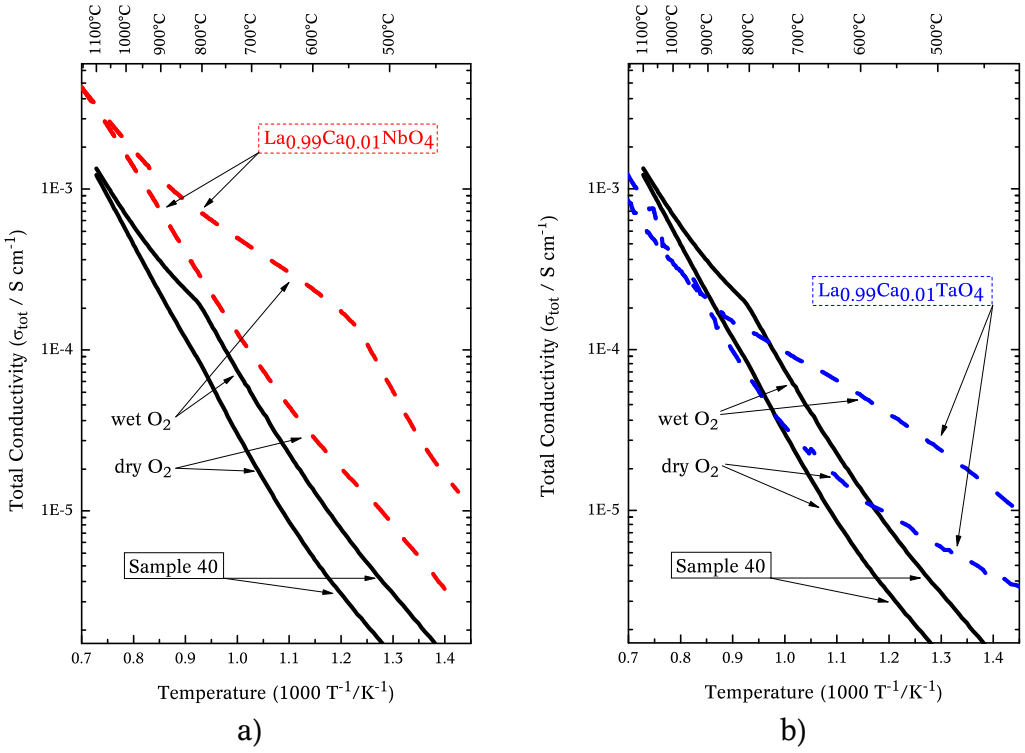

Figure 6.5 *– The total conductivity of sample 40, $La_{0.99}Ca_{0.01}Nb_{0.60}Ta_{0.40}O_4$, and $La_{0.99}Ca_{0.01}NbO_4$ (a) or $La_{0.99}Ca_{0.01}TaO_4$ (b) as a function of inverse temperature in atmospheres containing wet O_2 and dry O_2 respectively.*

Temperature ramps in wet and dry O_2 comparing the conductivity of sample 40 to its parent phases, reveal some interesting points of interest. First of all, the slopes for measurements in dry O_2 and those for measurements on the high temperature phase of both samples in wet O_2 are roughly the same for sample 40 and Ca-doped $LaNbO_4$. (Figure 6.5) The total conductivity for $LaNbO_4$ is much higher than that of sample 40 at any temperature and in any atmosphere.

$LaNbO_4$ has a much greater difference in conductivity between the measurements done in wet and dry O_2 than sample 40 has. This could be a sign of much higher proton concentration and therefore higher proton conductivity under oxidizing conditions in $LaNbO_4$, compared to sample 40. (ref. equation (2.9))

The slope of the wet O2-ramp is steeper for sample 40 than that of pure Ca-doped $LaNbO_4$ at temperatures above breaking point. This is a probable sign of lower activation energy for proton diffusion in the high-temperature phase of $LaNbO_4$ than corresponding energy for sample 40.

Sample 40 has very little in common with Ca-doped $LaTaO_4$ when comparing temperature ramps (Figure 6.5 b). The shapes are different and the evolution of conductivity as a function of inverse temperature is different. The low-temperature phase monoclinic phase of sample 40 has, for the most part, lower conductivity at any given temperature than $LaTaO_4$ in both wet and dry O_2. The high-temperature tetragonal phase of sample 40, on the other hand, has slightly higher conductivity than $LaTaO_4$ in both wet and dry O_2.

$LaTaO_4$ does have a greater difference in conductivity between the measurements done in wet and dry O_2, at low temperature, than corresponding difference in sample 40. This could, as earlier stated for $LaNbO_4$, be a sign of higher proton concentration and therefore higher proton conductivity in $LaTaO_4$, compared to sample 40, at least at lower temperatures and oxidizing atmospheres.

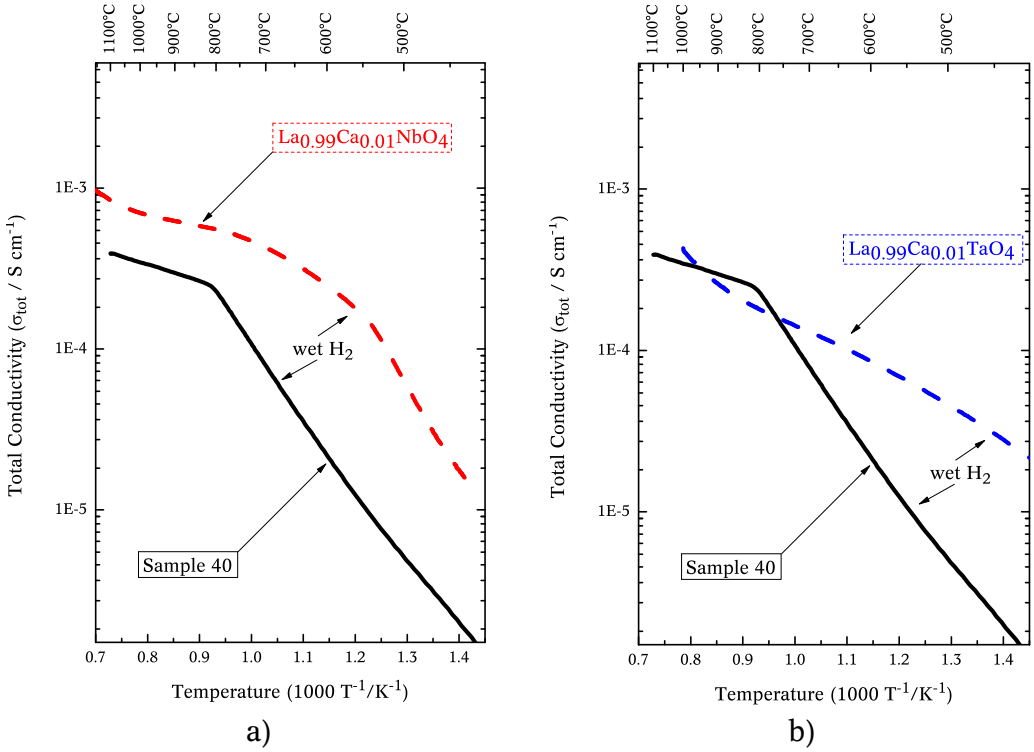

Figure 6.6 *– The total conductivity of sample 40, $La_{0.99}Ca_{0.01}Nb_{0.60}Ta_{0.40}O_4$, and $La_{0.99}Ca_{0.01}NbO_4$ (a) or $La_{0.99}Ca_{0.01}TaO_4$ (b) as a function of inverse temperature in atmospheres containing wet H_2.*

While sample 40 experiences a very abrupt change in conductivity as temperature decreases through its phase transition temperature in wet H_2, pure $LaNbO_4$ does not (Figure 6.6).

$LaNbO_4$ seems to have three distinct conductivity and temperature regimes. From low temperatures up to a maximum temperature of roughly 500-550°C, the low-temperature monoclinic phase displays its conductivity. From this temperature the high-temperature tetragonal phase of $LaNbO_4$ takes over. Between 500-550°C and 1000-1050°C, a second conductivity regime is seen. The slope is somewhat gentler than for the low-temperature phase and is possibly a sign of lower activation energy for proton conductivity. The third temperature regime appears at temperatures above 1000-1050°C; this signifies a gradual transition to oxygen ionic conductivity.

Sample 40, on the other hand, has only two distinct temperature and conductivity regimes; below and above the phase transition temperature. The low temperature phase has the steepest curve and therefore probably has the highest activation energy for proton conductivity.

Total conductivities and trends discussed in this section can be summarized like this for two chosen temperatures. As already stated, conductivities increase with increasing Ta-content in the high-temperature phase, while decrease with Ta-content in the low-temperature phase:

Table 6.3 *– Proton conductivities*

Sample number	1100°C (tetragonal)	700°C (monoclinic)
40	$3.9 \cdot 10^{-4}$ S·cm^{-1}	$7.8 \cdot 10^{-5}$ S·cm^{-1}
42	$4.0 \cdot 10^{-4}$ S·cm^{-1}	$7.5 \cdot 10^{-5}$ S·cm^{-1}
48	$4.5 \cdot 10^{-4}$ S·cm^{-1}	$6.3 \cdot 10^{-5}$ S·cm^{-1}

If one assumes 100% proton conductivity under reducing conditions for the high temperature phase, the maximum proton conductivity of $4.5 \cdot 10^{-4}$ S·cm^{-1} at 1100°C is roughly half that of pure Ca-doped $LaNbO_4$ at 950°C.

6.6 Future work

It soon became apparent that the limited time frame of a master's thesis would not make it possible for this student to do a complete set of measurement on all prepared samples. If a more detailed analysis of all the samples' conductivities were carried through in the future, a clearer picture of the conductivities around the one phase/two phase area of the $LaNbO_4$-$LaTaO_4$-phase diagram might emerge. Maybe increasing Ta–doping even further, beyond 48%, could give higher proton conductivities in the high-temperature phase of $LaNbO_4$ due to increased effective Ca-doping.

Future work should probably concentrate more on the very left part (Nb-rich part) of the $LaNbO_4$-$LaTaO_4$-phase diagram. A small concentration of Ta in $LaNbO_4$ would probably not hamper its proton conductivity too much, while at the same time increase its phase transition temperature and reduce the TEC. More detailed analysis is required to see whether the introduction of Tantalum is worth it or not.

Another area of interest is to see whether it's possible to create a nanoscopic secondary $LaTaO_4$-phase inside the parent $LaNbO_4$-phase. One seemingly viable route to this goal is to make nanoscopic powders of $LaNbO_4$ and $LaTaO_4$, create a sample with just enough $LaTaO_4$ to keep the sample phase pure at a medium temperature (~1000°C), sinter the nanoscopic grains at this temperature before quenching the sample through the one phase/two phase boundary in the phase diagram. This technique could possibly create nanoscopic secondary phase areas inside the parent phase as the phase boundary is crossed. If temperature is decreased quickly to a level where its kinetics are too slow and unable to increase the size of grains, the nanoscopic secondary phase should be locked in.

Looking further ahead, it would be interesting to see how heavily Ta-doped $LaNbO_4$ mates to common electrode materials. It would also be interesting to see whether the increased conductivity of wet H_2 over wet O_2 actually stems from a reduction of the samples.

7 Conclusion

As seen in previous sections, the low-temperature monoclinic phase of Ta-doped $LaNbO_4$ has too low proton concentration and proton conductivity to be useful in a fuel cell. Only the high-temperature, tetragonal phase of Ta-doped $LaNbO_4$-samples displays proton conductivities high enough to be of any interest as fuel cell materials. As was observed in previous sections, the phase transition temperature of the samples increased with increasing Ta-content to a maximum temperature of ~850°C using 48 percent tantalum.

Although the high-temperature phase of the measured samples have a significant percentage of proton conductivity, their total conductivity is still quite a bit lower, at any temperature, than the total conductivity for pure Ca-doped $LaNbO_4$. At ~1000°C pure Ca-doped $LaNbO_4$ displays a proton conductivity at least twice that of any samples tested in this thesis. Vullum et al. showed that Ta-doped $LaNbO_4$ has much smaller differences in thermal expansion coefficient than pure $LaNbO_4$. This could, in combination with the significant proton conductivity measured for Ta-doped $LaNbO_4$, still be an interesting combination for a fuel cell material.

It was seen, in sample 48, that conductivities did not change noticeably with the introduction of secondary phases. The sample still followed the trends set by other samples, especially trends set by sample 40 and 44. Unfortunately, the most significant secondary phases, seen in XRD, did not appear to include $LaTaO_4$. A nanoscopic secondary phase of $LaTaO_4$, or any other phase, within the $LaNbO_4$ main phase was not attainable under current synthesis conditions.

Future work is required to see whether Ta-doped $LaNbO_4$ with lower or higher Ta-content could give any improvements in proton conductivity over pure Ca-doped $LaNbO_4$.

There are possibly other systems more or less similar to the $LaNbO_4$-$LaTaO_4$-system were solid solubility exists over large ranges of

concentrations. Maybe conductivities in these systems could benefit from addition of one phase into the other, and thereby increasing the amount of acceptor doping possible?

8 Bibliography

1 Schönbein, C. F. On the Voltaic Polarization of certain Solid and Fluid Substances. *Philosophical Magazine and Journal of Science*, XIV (January-June 1839), 43-45.

2 Grove, W. R. On Voltaic Series and the Combination of Gases by Platinum. *Philosophical Magazine and Journal of Science*, XIV (January-June 1839), 127-130.

3 Grove, W. R. On a Gaseous Voltaic Battery. *Philosophical Magazine and Journal of Science*, XXI (July-December 1842), 417-420.

4 Haugsrud, R. and Norby, T. High-temperature proton conductivity in acceptor-doped LaNbO4. *Solid State Ionics*, 177, 13-14 (2006), 1129-1135.

5 Haugsrud, R. and Norby, T. High-temperature proton conductivity in acceptor-substituted rare-earth ortho-tantalates, LnTaO4. *Journal of the American Ceramic Society*, 90, 4 (2007), 1116-1121.

6 Afonskii, N. S. and Neiman, M. B. Phase composition of the lanthanum oxide-tantalum oxide system. *Izvestiya Akademii Nauk SSSR, Neorganicheskie Materialy*, 3, 7 (1967), 1280-1283.

7 Savchenko, E. P., Godina, N. A., and Keler, E. K. Reactions in solid phases between niobium pentoxide and lanthanum, cerium, and praseodymium oxides. *Zhurnal Prikladnoi Khimii*, 39, 9 (1966), 1913-1920.

8 Costamagna, P. and Srinivasan, S. Quantum jumps in the PEMFC science and technology from the 1960s to the year 2000: Part I. Fundamental scientific aspects. *Journal of Power Sources*, 102, 1-2 (December 2001), 242-252.

9 Qingfeng, L., He, R., Gao, J.-A., Jensen, J. O., and Bjerrum, N. J. The CO Poisoning Effect in PEMFCs Operational at Temperatures up to 200°C. *Journal of The Electrochemical Society*, 150, 12 (December 2003), 1599-1605.

10 Heinzel, A. and Barragán, V. M. A review of the state-of-the-art of the methanol crossover in direct methanol fuel cells. *Journal of Power Sources*, 84, 1 (November 1999), 70-74.

11 Iwahara, H., Esaka, T., Uchida, H., and Maeda, N. Proton conduction in sintered oxides and its application to steam electrolysis for hydrogen production. *Solid State Ionics*, 3-4 (1981), 359-363.

12 Uchida, H., Maeda, N., and Iwahara, H. Relation between proton and hole conduction in $SrCeO_3$-based solid electrolytes under water-containing atmospheres at high temperatures. *Solid State Ionics*, 11, 2 (October 1983), 117-124.

13 Iwahara, H., Uchida, H., Ono, K., and Ogaki, K. Proton conduction in sintered oxides based on barium cerate ($BaCeO_3$). *Journal of the Electrochemical Society*, 135, 2 (1988), 529-533.

14 Bonanos, N., Ellis, B., Knight, K. S., and Mahmood, M. N. Ionic conductivity of gadolinium-doped barium cerate perovskites. *Solid State Ionics*, 35, 1-2 (1989), 179-188.

15 Iwahara, H., Uchida, H., and Morimoto, K. High Temperature Solid Electrolyte Fuel Cells Using Perovskite-Type Oxide Based on $BaCeO_3$. *Journal of The Electrochemical Society*, 137, 2 (February 1990), 462-465.

16 Kreuer, K. D. On the development of proton conducting materials for technological applications. *Solid State Ionics*, 97, 1-4 (1997), 1-15.

17 Nomura, K., Takeuchi, T., Kamo, S.-I., Kageyama, H., and Miyazaki, Y. Proton conduction in doped $LaScO_3$ perovskites. *Solid State Ionics*, 175, 1-4 (2004), 553-555.

18 Arkhipova, E. V., Zuev, M. G., and V., Zolotukhina L. Subsolidus phase equilibria of in the La_2O_3–V_2O_5–Nb_2O_5–Ta_2O_5 system. *Journal of Alloys and Compounds*, 305, 1-2 (January 2000), 58-62.

19 Vullum, F., Nitsche, F., Selbach, S. M., and Grande, T. Solid solubility and phase transitions in the system $LaNb_{1-x}Ta_xO_4$. *Journal of*

Solid State Chemistry, 181, 10 (2008), 2580-2585.

20 Haugsrud, R. and Norby, T. Proton conduction in rare-earth ortho-niobates and ortho-tantalates. *Nature Materials*, 5 (2006), 193-196.

21 Kröger, F. A. and Vink, H. J. Relations between concentrations of imperfections in crystalline solids. *Solid State Physics*, 3 (1956), 307-435.

22 Kröger, F. A. *The Chemistry of Imperfect Crystals*. North-Holland Publishing Company, Amsterdam, 1964.

23 Chua, L. Memristor-The missing circuit element. *IEEE Transactions on Circuit Theory*, 18, 5 (September 1971), 507- 519.

24 Strukov, D. B., Snider, G. S., Stewart, D. R., and S., Williams R. The missing memristor found. *Nature*, 453 (May 2008), 80-83.

25 Barsoukov, E. and Macdonald, J. R. *Impedance Spectroscopy: Theory, Experiment, and Applications*. John Wiley & Sons, Inc., 2005.

26 Hsu, C. H. and Mansfeld, F. Technical note: concerning the conversion of the constant phase element parameter Y_0 into a capacitance. *Corrosion*, 57, 9 (2001), 747-748.

27 Haile, Sossina M., West, David L., and Campbell, John. The role of microstructure and processing on the proton conducting properties of gadolinium-doped barium cerate. *Journal of Materials Research*, 13, 6 (1998), 1576-1595.

28 Komkov, A. X-ray investigation of synthetic compounds of rare earths of the type $MNbO_4$. *Doklady Akademii Nauk SSSR*, 126 (1959), 853-854.

29 Jian, L. and Wayman, C. M. Monoclinic-to-tetragonal phase transformation in a ceramic rare-earth orthoniobate, $LaNbO_4$. *Journal of the American Ceramic Society*, 80, 3 (1997), 803-806.

30 Stubičan, V. S. High-temperature transitions in rare-earth niobates and tantalates. *Journal of the American Ceramic Society*, 47, 2 (1964), 55-58.

31 Gingerich, K. A. and Bair, H. E. Relation between ionic radii and transformation temperature in rare earth niobates. *Advances in X-*

Ray Analysis, 7 (1964), 22-30.

32 Brixner, L. H., Whitney, J. F., Zumsteg, F. C., and Jones, G. A. Ferroelasticity in the lanthanide niobate ($LnNbO_4$)-type rare earth niobates. *Materials Research Bulletin*, 12, 1 (1977), 17-24.

33 Tsunekawa, S, Kamiyama, T., Sasaki, K., Asano, H., and Fukuda, T. Precise structure analysis by neutron diffraction for $RNbO_4$ and distortion of NbO_4 tetrahedra. *Acta Crystallographica*, 49, 4 (July 1993), 595-600.

34 Brandenburg, K and Putz, H. *Diamond 3.2c*. Crystal Impact GbR, Bonn, 2009.

35 David, W. I. F. The high-temperature paraelastic structure of lanthanum niobate ($LaNbO_4$). *Materials Research Bulletin*, 18, 6 (1983), 749-756.

36 Prytz, O. and Taftø, J. Accurate determination of domain boundary orientation in $LaNbO_4$. *Acta Materialia*, 53 (2005), 297-302.

37 Cava, R. J. and Roth, R. S. The structure of $LaTaO_4$ at 300°C by neutron powder profile analysis. *Journal of Solid State Chemistry*, 36, 2 (1981), 139-147.

38 Hartenbach, I., Lissner, F., Nikelski, T., Meier, S. F., Mueller-Bunz, H., and Schleid, T. About lanthanide oxotantalates with the formula $MTaO_4$ (M = La - Nd, Sm - Lu). *Zeitschrift fuer Anorganische und Allgemeine Chemie*, 631, 12 (2005), 2377-2382.

39 Kurova, T. A. and Aleksandrov, V. B. Crystal structure of lanthanum tantalate. *Doklady Akademii Nauk SSSR*, 201, 5 (1971), 1095-1098.

40 Teterin, G. A., Zinchenko, V. F., Kuz'min, V. E., Babich, T. G., and Minaev, I. M. The evaluation of thermal stability of lanthanide niobates at high temperature. *Ukrainskii Khimicheskii Zhurnal (Russian Edition)*, 53, 9 (1987), 906-910.

41 Haugsrud, R. *Raw data for $LaNbO_4$ and $LaTaO_4$. Private e-mail correspondence to Odd-Arne Ertzeid*. September 18th 2008.

42 Tyholdt, F. Electrical conductivity and defect structure of Sr-substituted $LaPO_4$. *Master's thesis*, University of Oslo (1999).

43 Galasso, F. S. *Perovskites and High Tc Superconductors*. OPA, Amsterdam, 1990.

44 Weise, E., Langenbach-Kuttert, B., Sturm, J., and Gruehn, R. Zur Darstellung und Struktur von $LaTa_3O_9$ Röntgenographische und elektronenmikroskopische Untersuchungen. *Zeitschrift für anorganische Chemie*, 548 , 5 (1987), 33-44.

45 Boukamp, B. A. *Equivalent Circuit for Windows 1.2*. University of Twente/WisseQ, Enschede, 2008.

46 Microsoft. *Office Excel 2007 SP2*. Microsoft. 2006.

47 Corporation, OriginLab. *OriginPro 8 SR4*. OriginLab Corporation, Northampton, 2008.

48 Yajima, T, Kazeoka, H, Yogo, T, and Iwahara, H. Proton conduction in sintered oxides based on $CaZrO_3$. *Solid State Ionics*, 47, 3-4 (1991), 271-275.

49 Haugsrud, R. *Temperature ramps for $LaTaO_4$. Private e-mail correspondence to Odd-Arne Ertzeid*. September 24th 2009.